University of Southampton
Faculty of Engineering, Science & Mathematics
Optoelectronics Research Centre

Design Method for Ultimate Efficiency in Linear-cavity Continuous-wave Lasers Using Distributed-Feedback

by
Kuthan Yelen

Thesis Submitted for the Degree of Doctor of Philosophy

June 2004

UNIVERSITY OF SOUTHAMPTON

ABSTRACT

OPTOELECTRONICS RESEARCH CENTRE

Doctor of Philosophy

DESIGN METHOD FOR ULTIMATE EFFICIENCY IN LINEAR-CAVITY CONTINOUS-WAVE LASERS USING DISTRIBUTED-FEEDBACK

by Kuthan Yelen

A novel analytical method for the design of linear-cavity continuous-wave laser cavities that guarantees the ultimate efficiency is developed, theoretically studied and experimentally verified. Opposed to the earlier methods, which optimise the parameters of *a priori* defined cavity, the developed method derives the cavity analytically based on the active medium properties for the chosen pumping scheme. The method combines the general grating design equations, valid for both passive and active media, and the optimum signal power calculations. The idea that lies at the heart of the design method is to sustain the optimum signal power at every single point in the entire cavity by employing distributed-feedback for the maximum local, as a result, for the maximum overall conversion efficiency.

Theoretical study starts with the critical investigation of the previous optimisation approaches. After addressing the limitations of these approaches, it is shown how to improve the efficiency further than the parametric optimisation using intuitive arguments based on the effective cavity length and optimum reflectivities in DFB lasers. The critical importance of the signal distribution is highlighted, and following this observation the grating design method for arbitrary signal distributions is developed. The concept of optimum signal power is introduced and the spatial unfolding of the optimum values is illustrated. Boundary conditions, grating production limitations and effects of modelling parameters are addressed. Modal stability of the new designs is investigated.

A novel approach to the simulation of Er/Yb co-doped fibre lasers is presented with experimental justification. Accurate laser characteristics are predicted for different designs, including the ultimate efficiency designs. Theoretical studies are verified with experimental data in Er/Yb co-doped fibre and discussions are extended to Yb doped fibres, high pump powers and alternative pumping schemes.

TABLE OF CONTENTS

List of Abbreviations

ASE	Amplified Spontaneous Emission
CUP	Co-operative Up-Conversion
DBR	Distributed Bragg Reflector
DFB	Distributed Feedback
ESA	Excited-state Absorption
FP	Fabry-Perot
JAC	Jacketed Air Cladding
LHS	Left-hand side
NA	Numerical Aperture
PM	Power Meter
RHS	Right-hand side
TLS	Tunable Laser Source
WDM	Wavelength Division Multiplexing

List of Symbols

Symbol	Value or [Unit]	Description
Subscripts		
s		At signal wavelength
p		At pump wavelength
n		Normal ytterbium ions
q		Lifetime quenched ytterbium Ions
Subscripts		
a		Absorption
e		Emission
C_{ESA}	$[\ m^2\ ]$	Excited state absorption cross-section
C_{UP}	$[\ m^3s^{-1}\ ]$	Co-operative up-conversion coefficient
D	[m]	Penetration depth (Chapter 5)
D(z)	[W]	Difference between forward and backward propagating powers at position z
E	$[\ \sqrt{W/m^2}\ ]$	Total electric field (Normalised)
Er_i	[]	Single erbium ion at energy level i
G	[W]	Generated signal power over a volume
$\Delta G(z)$	[W / m]	Generated signal per unit length at position z
k_{tr}	$[\ m^3s^{-1}\ ]$	Energy transfer coefficient between Er and Yb ions
L	[m]	Total device length
L_{eff}	[m]	Effective cavity length
n_0	[]	Effective refractive index of the medium
Δn	[]	Refractive index modulation amplitude
n_1	[]	Refractive index of the core
n_2	[]	Refractive index of the cladding
N_T	$[\ m^{-3}\ ]$	Total ion concentration
N^{Er}	$[\ m^{-3}\ ]$	Total erbium concentration
N^{Yb}	$[\ m^{-3}\ ]$	Total ytterbium concentration
N_i	$[\ m^{-3}\ ]$	Ion concentration at energy level i

$P(z)$	[W]	Pump power at position z in a laser cavity
$\Delta P(z)$	[W / m]	Absorbed pump power per unit length
P_p	[W]	Pump power in an amplifying medium
P_s	[W]	Signal power in an amplifying medium
r	[]	Reflection coefficient
R	[]	Reflectivity
R^+	$[\sqrt{W/m^2}]$	Forward Propagating Electric Field Envelope (Normalised)
R^-	$[\sqrt{W/m^2}]$	Backward Propagating Electric Field Envelope (Normalised)
$S(z)$	[W]	Sum of forward and backward propagating powers at position z
Yb_i	[]	Single ytterbium ion at energy level i
z	[m]	Position
z_π	[m]	Position of the phase-shift
α	[m^{-1}]	Field gain (positive) or loss (negative) coefficient
β	[m^{-1}]	Propagation constant
$\Gamma_{s,p}$	[]	Overlap coefficient for signal or pump field
Γ	[m^{-1}]	Phase difference between the fields and the grating
ε	[m^{-1}]	Field background loss
Λ	[m]	Period of the grating
η	[]	Pump-to-signal conversion efficiency
$\kappa(z)$	[m^{-1}]	Coupling coefficient of the grating at position z
λ	[m]	Wavelength
ν	[s^{-1}]	Frequency
σ	[m^2]	Cross-section
τ_i	[s]	Life-time at energy level i
Ψ	[]	Transverse modal distribution

To my aunt Ayfer Özbeyli, for her contributions to my life…
Teyzem Ayfer Özbeyli'ye, hayatımdaki - destekten öte - katkılarına minnetle…

ACKNOWLEDGEMENTS

With ample amount of coffee and the ability to survive some not-so-easy periods any stubborn person can complete a PhD. However, enjoying the entire PhD experience requires more than being determined; you have to be lucky. A sensible *initial point*, years-long non-fading guidance, and a harmony with your supervisor in terms of both academic approach and personality are what it takes to make your postgraduate life enjoyable. With the wisdom of hindsight, I can see that I was one of the luckiest persons around. For all these, I thank my supervisor Professor Michalis Zervas heartily.

Playing with equations, pushing the simulations to the limits, and the feeling of being the only person, at that particular moment, who knows what it is all about, is fantastic. But making things actually work in reality is even more satisfying. Louise Hickey is the person who made it possible for me to link all the theory to the physical world. I would like to thank Louise and the personnel of Southampton Photonics, SPI Inc. for the icing on the cake. Writing up the thesis is another story. Avoiding *writers' cramp* by *hitting the gym,* I finally finished the thesis and dear Eleanor Tarbox kindly allocated her valuable time to correct my countless mistakes.

Of course, no law of physics is as fundamental as the laws of economics. Without the financial supports of the Committee of Vice-Chancellors and Principles of the Universities of the United Kingdom (CVCP) through Overseas Research Students Award (ORS) and the University of Southampton's postgraduate research scholarship, the design method for the ultimate laser efficiency couldn't be developed.

"*The purpose of computing is insight, not numbers.*"
R.W. Hamming

Chapter 1 Introduction

1.1. Motivation

Improving the efficiency of lasers is of great importance throughout the entire optoelectronics field. As well as being a fundamental research interest, better laser efficiency is a very strong commercial driver too. Today, linear-cavity continuous-wave (CW) lasers are one of the most widely used types of lasers that come in categories such as semiconductor, solid-state, fibre and planar glass. Therefore maximizing the efficiency of this particular type of lasers is very desirable and will have a broad impact in the optoelectronics field.

The performance of a laser is set by various characteristics of the device such as the active medium spectroscopy, temperature control mechanism and pumping scheme. One of the most critical features of a laser that has profound effect on the efficiency is the design of the resonator cavity. The structure of the cavity defines the circulating power, the amount of output coupling and the extracted output power. For a given pump power and active medium under the same operating conditions different laser cavities yield different efficiencies; therefore the cavity design lies at the heart of laser performance.

The simplest form of a linear cavity laser is the classic Fabry-Perot (FP) type laser, which comprises two mirrors and an active medium in between, whereas the most complex linear cavity is the distributed feedback (DFB) laser, which incorporates a grating into the active medium. A distributed Bragg reflector (DBR) or a FP laser can be treated as a sub-set of DFB lasers: In the case of a DBR laser the coupling coefficient of the grating in the active medium is reduced to zero, but it is extended into the passive section. In the case of a FP laser the coupling is localised at the ends of the active medium by placing infinitesimal gratings; that is mirrors.

Optimisation of the cavity design for FP lasers dates back to the well- known Rigrod analysis [1, 2]. This analytical optimisation, however, is based on very limiting assumptions and simplifications: First of all, the unsaturated gain is assumed to be constant throughout the entire cavity. This requires a constant pump power, which can,

for example, be valid for electrically side-pumped semiconductor lasers however this assumption excludes many other pumping schemes. Then the active medium is assumed to be a homogenously saturated 2-level system. Optimisation of a FP laser cavity constructed in this medium assumes very small output coupling from the end mirrors (very high reflectivity) and very small saturated gain. With these assumptions the circulating signal inside the cavity is almost constant and with an additional assumption of constant loss the optimum output coupling and the optimum circulating signal are found analytically (For example see [3]).

Any deviation from any of these assumptions, which is almost always the case for any real system, causes the analytical Rigrod optimisation to break down. In the case of a multi-level active medium with varying signal and pump powers or signal dependent loss a *parametric* optimisation is required; that is one of the cavity parameters is varied at a time while the others are kept constant and the laser is simulated for the output powers using numerical techniques.

A FP laser cavity is defined by only three parameters: the two mirror reflectivites and the cavity length. Therefore, a parametric optimisation, although computationally intense, can consider all the possible combinations. But the FP cavity is not the only possible laser configuration, hence the efficiency maximised for a FP design is not guaranteed to be the maximum possible for the given medium and pump power. Other laser structures such as distributed Bragg reflector (DBR) or distributed feedback (DFB) configurations may provide better efficiencies under comparable conditions. However optimisation of these complex structures parametrically is even more challenging since there are literally an infinite number of combinations of parameters when apodisation profile, chirp profile, total length and phase shift positions and amounts are considered; therefore the parametric optimisation cannot guarantee the maximum efficiency possible for the given pump and active medium. A maximum may be a local peak in efficiency over an infinite number of different parameter combinations.

To sum up, there is a lack of a general comprehensive design method for widely used linear cavity CW lasers which would assure the fundamental efficiency limit analytically.

In this work we present a novel analytical method for the design of laser cavities. In our approach we do not *optimise* a certain laser cavity but we *derive* the cavity for a given pump and active medium that guarantees the ultimate efficiency possible.

1.2. Approach

Being the most complex and general cavity, DFB lasers will provide the starting point for our study. We will critically investigate the classic DFB laser optimisation approach in order to improve our understanding of the effects of cavity design on the laser performance. Observing the importance of the signal distribution in the cavity and experimentally verifying its effect, we will introduce the concept of the optimum signal and continue with the method for achieving the optimum signal distribution in the entire cavity. Then imposing the boundary conditions and production limitations and employing the novel grating design method we will show how to find the coupling coefficient profile which provides this signal distribution.

The method does not discriminate between the Fabry-Perot, DBR or DFB structures, however, in general, the maximum efficiency laser cavity requires a distributed feedback; consequently the method is applicable to any active medium in which a grating can be incorporated. Therefore we expect this design method to find immediate application over a wide device range from semiconductor, planar glass, solid-state bulk to fibre lasers since in these media the grating writing technologies have already matured.

As a demonstration we applied the method experimentally in Er/Yb co-doped fibre lasers. We chose this particular medium because of the attractive feature of fibre DFB lasers that we will cover in Chapter 2.

1.3. Modelling and Simulations

To facilitate the theoretical and the experimental investigations we use numerical models extensively, both for the derivation of the laser designs and their simulation. Therefore, the model and the simulation tools we developed are an essential part of our study.

Although several entirely theoretical works on modelling of erbium-ytterbium co-doped media have been reported [4-10] with only very few experimental verifications for amplifiers [11, 12] there is no work on benchmarking the simulation results with experimental results for Er/Yb co-doped lasers, neither in FP, DBR or DFB configuration. The value of any simulation result should be judged according to its proximity to the behaviour of the real device or system. If the performance of a model is not checked against the experimental data then the simulation results will make sense only in terms of *tendencies* instead of actual numbers.

Here, in addition to the novel design method, we present a model for Er/Yb co-doped fibre DFB lasers which takes into account the excited-state absorption and co-operative

up conversion in erbium ions as well as the life-time quenching of ytterbium ions. We describe simple techniques for the measurement of the model parameters. In this new modelling approach we treat the pump, the active medium and the feedback mechanism as a complete system, and we characterise and model each one of them. For the first time, we present simulations that predict the actual characteristics of the Er/Yb co-doped DFB fibre lasers within the range of experimental measurement errors.

1.4. Overview of the Thesis

Following this introduction chapter, an overview of fibre DFB lasers is presented in Chapter 2, followed by the brief description of numerical and computational methods used throughout the rest of the study in Chapter 3. The modelling of the active medium and DFB lasers are discussed in Chapter 4. The transitions and the rate equations are discussed in detail and the measurement of the required parameters as well as the characterisation of the pump source and the grating are presented. Results of the simulations are compared against the experimental data.

Chapter 5 is devoted to the detailed investigation of the classic DFB laser optimisation method. It is shown that, the method is equivalent to the Rigrod analysis for the reflectivities, however in addition to the feedback the signal distribution inside the cavity is identified as a critical variable affecting the efficiency. The concept of effective cavity is introduced and the step-apodised profile is presented to increase the effective cavity length for better efficiency. The theoretical results are verified with the experimental data.

Identification of the signal distribution as a critical factor for the laser efficiency leads to the general theoretical analysis for a design method in order to achieve any desired signal distribution inside passive and active cavities in Chapter 6. Here we discuss the optimum signal distribution for the maximum possible efficiency and we illustrate the new design method in a numerical study in a simple ytterbium doped fibre.

Chapter 7 covers the theoretical and experimental application of the design method in erbium-ytterbium co-doped fibre. Initially, designs for alternative pumping schemes are derived and compared, longitudinal-mode stability is discussed, and the effects of the uncertainties in the model parameters on the design are investigated, then the method is experimentally verified. High power applications along with alternative pump and signal wavelengths in ytterbium doped fibres are discussed in Chapter 8.

Concluding remarks on the design method are presented in Chapter 9. References are given at the end of each chapter.

1.5. References

[1] W. W. Rigrod, "Saturation Effects in High-Gain Lasers," *Journal of Applied Physics*, vol. 36, no. 8, pp. 2487-2490, 1965.

[2] C. T. Meneely, "Laser Mirror Transmissivity Optimization in High Power Optical Cavities," *Applied Optics*, vol. 6, no. 8, pp. 1434-1436, 1967.

[3] A. E. Siegman, "Section 12.3," in *LASERS*. Sausalita, CA: University Science Books, 1986.

[4] C. Strohhofer and A. Polman, "Relationship between gain and Yb3+ concentration in Er3+ - Yb3+ doped waveguide amplifiers," *Journal of Applied Physics*, vol. 90, no. 9, pp. 4314-4320, 2001.

[5] E. Yahel and A. Hardy, "Modeling and Optimization of Short Er3+-Yb3+ Codoped Fiber Lasers," *IEEE Journal of Quantum Electronics*, vol. 39, no. 11, pp. 1444-1451, 2003.

[6] E. Yahel and A. Hardy, "Modeling High-Power Er3+ - Yb3+ Codoped Fiber Lasers," *Journal of Lightwave Technology*, vol. 21, no. 9, pp. 2044-2052, 2003.

[7] M. Karasek, "Optimum Design of Er3+-Yb3+ Codoped Fibers for Large-Signal High-Pump-Power Applications," *IEEE Journal of Quantum Electronics*, vol. 33, no. 10, pp. 1699-1705, 1997.

[8] G. C. Valley, "Modeling Cladding-Pumped Er/Yb Fiber Amplifiers," *Optical Fiber Technology*, vol. 7, no. 1, pp 21-44, 2001.

[9] F. Di Pasquale, "Modeling of Highly-Efficient Grating-Feedback and Fabry-Perot Er3+ Yb3+ Co-Doped Fiber Lasers," *IEEE Journal of Quantum Electronics*, vol. 32, no. 2, pp. 326-332, 1996.

[10] J. Nilsson, P. Scheer, and B. Jaskorzynska, "Modeling and Optimization of Short Yb3+ Sensitized Er3+ Doped Fiber Amplifiers," *IEEE Photonics Technology Letters*, vol. 6, no. 3, pp. 383-385, 1994.

[11] G. Sorbello, S. Taccheo, and P. Laporta, "Numerical modelling and experimental investigation of double-cladding erbium-ytterbium-doped fibre amplifiers," *Optical and Quantum Electronics*, vol. 33, no. 6, pp 599-619, 2001.

[12] M. Achtenhagen, R. J. Beeson, F. Pan, B. Nyman, and A. Hardy, "Gain and Noise in ytterbium-Sensitized erbium-Doped Fiber Amplifiers: Measurements and Simulations," *Journal of Lightwave Technology*, vol. 19, no. 10, pp. 1521-1526, 2001.

Chapter 2 Fibre DFB Lasers: A Brief Historical Perspective and Applications

2.1. Historical Perspective

The discovery of lasing in periodic structures dates back to the early 70s. Kogelnik and Shank, then at the Bell Laboratories, reported lasing action in a dyed gelatine whose refractive index was periodically modulated [1]. Figure 2-1 illustrates the earliest DFB laser structure. The laser consists of a uniform refractive index grating, with constant amplitude and constant period, incorporated in an active medium. This classic design operates at two fundamental longitudinal modes at different wavelengths, corresponding to the edges of the grating band-gap, and gives symmetric output powers from both ends, P_{left} and P_{right}, which are equally divided between these two modes. Therefore, such a cavity provides dual-wavelength bi-directional operation.

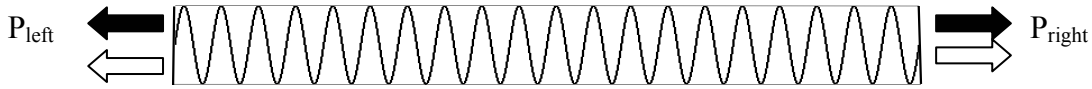

Figure 2-1 Refractive index profile for classic DFB laser design with two-wavelength bi-directional operation.

The theory of lasing action in periodic structures was developed in the classic paper, again by Kogelnik and Shank, based on coupled-wave theory [2].

After this initial observation of lasing action in the periodic structures, the second milestone leading to fibre DFB lasers came with the discovery of the formation of permanent gratings in photosensitive germania-doped fibres by Hill *et al* [3] of the Canadian Communications Research Centre in 1978. The grating was formed by the interference pattern of argon-ion laser radiation propagating in opposite directions in the fibre. This method required that in order to write a Bragg grating at a certain wavelength one would need to launch a field at the same wavelength longitudinally into the fibre, therefore the wavelength of the Bragg grating was limited with the available source wavelengths.

The major breakthrough came from Meltz, Morey and Glenn, working at the United Technologies Research Centre, in 1989 [4]. In their holographic approach the grating was

produced by exposing the photosensitive fibre transversely to the interference pattern produced by two intersecting UV beams. By doing so, the period of the grating became a function of the angle between the beams, hence gratings with any periodicities could be written. This holographic writing approach found application in erbium doped fibre. Ball and Morey from United Technologies Research Centre and Zyskind *et al* from AT&T Bell Laboratories reported Er doped DBR laser structures in 1992 [5, 6]. Further improvements in grating writing techniques followed in 1993 by the introduction of phase masks in order to produce the UV interference pattern demonstrated by Hill *et al* [7] and Anderson *et al* of AT&T Bell Laboratories[8]. The phase-mask method reduced the mechanical sensitivity of the writing setup and allowed the introduction of apodisation and chirping profiles.

The next breakthrough, again in 1993, was the sensitisation of the erbium ions by co-doping with ytterbium. Kringlebotn *et al*, from the Optoelectronics Research Centre of Southampton University showed that the introduction of Yb ions dramatically increased the pump absorption [9]. This discovery made short fibre lasers feasible and efficient. However there was one problem: The highly absorbing Yb required the use of a phosphosilicate host which reduces the photosensitivity, as opposed to the germanosilicate host used for Er-only doped fibres. In 1994 the same research group from Southampton University solved this problem by loading the aluminophosphosilicate fibre with hydrogen to induce photosensitivity. They produced the first Er/Yb co-doped DFB fibre laser by combining the holographic grating writing method and the hydrogen loaded photosensitive active fibre technology [10]. Although the fibre suffered from hydrogen related losses they were able to obtain laser action. Contrary to the dual-wavelength output from the classic DFB cavity, in practice, a single-wavelength operation is desired. This can be achieved by introducing a π-shift in the spatial phase of the grating as shown below. Such a cavity provides a single-wavelength, coinciding with the grating Bragg wavelength, and bi-directional operation.

Figure 2-2 Symmetric, π-phase shifted DFB laser design for single-wavelength operation with bi-directional outputs.

Kringlebotn *et al* managed to introduce the necessary phase-shift by heating the grating locally with a thin resistance wire. Although this approach provided the single-mode operation desired, the induced phase shift was not a permanent feature of the grating.

In 1995 Cole, Loh *et al* from Southampton University improved the phase-mask method further [11, 12]. In their approach the fibre was moved relative to the phase mask while the writing beam was scanning. This method allowed the use of simple short phase masks, as opposed to the earlier, stationary, custom designed phase mask, and the required grating periodicity, phase-shift, apodisation and chirping profiles were produced by precisely controlling the position of the successive exposures to the UV interference pattern. This method greatly reduced the errors in the grating and allowed flexibility for the production of complex grating structures. 1995 witnessed the announcement of Er doped DFB fibre lasers with a permanent phase-shift simultaneously from two research groups. The studies by Loh and Laming from Southampton University [13] and Sejka *et al* from Technical University of Denmark [14] defined the point where DFB fibre production technology reached maturity. Once the basics of the technology had been established the efforts were focused around the optimisation of the fibre and the cavity designs in the following years.

Dong *et al* from Southampton University showed that a better fibre for DFB lasers would be one with a photosensitive cladding. Instead of loading the core with lossy hydrogen to get improved photosensitivity, they produced a boron and germanium-doped photosensitive cladding surrounding the active phosphosilicate core doped with Er and Yb [15], thus boosting the laser efficiency greatly in 1997.

At the end of 90s, Lauridsen *et al* [16, 17] and Ibsen *et al* [18] showed that a better cavity design would be composed of an optimum combination of grating strength and an asymmetrically positioned phase-shift so that the uni-directional output power is the maximum. By placing the phase-shift asymmetrically with respect to the grating centre, as shown in Figure 2-3 larger output power is obtained from the closer end.

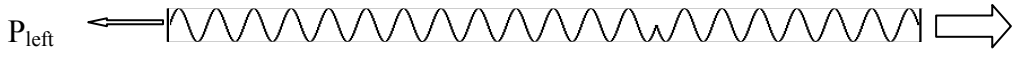

Figure 2-3 Refractive index profile for asymmetric π-phase shifted DFB laser design for single-wavelength uni-directional operation.

Today a typical state of art Er/Yb DFB laser is 5 cm long and produces around 20 mW output power at 1550 nm when pumped with 100 mW at 980 nm and is limited to 50 mW output power even when pump powers as large as 650 mW are used [19].

2.2. Applications

The fibre DFB lasers possess certain unique properties that make them more attractive compared to the semiconductor lasers. First of all they are in-fibre lasers therefore they are inherently fibre compatible and their output can be connected to a transmission fibre using a standard splice. Similarly, the pump power can be delivered to the fibre DFB laser using simple low-loss transmission fibres. In addition, very simple passive thermal stabilisation is sufficient to ensure the stability of a fibre DFB laser. A number of different active dopants, such as erbium, ytterbium, neodymium and thulium, can be used in order to cover different windows of the optical spectrum and offer extended coverage.

These features, combined with the ability to define the emitted wavelength precisely, a narrow linewidth and a low relative intensity noise (RIN), make DFB fibre lasers very advantageous for telecommunication applications [20-22]. Typically an Er/Yb doped laser has a linewidth less than 50 kHz, much smaller compared to 1MHz of a conventional semiconductor laser. The RIN figure in such lasers is less than 100 dB/Hz above 50MHz, and the signal-to-noise ratio is larger than 65 dB. In addition to these advantages, a number of DFB fibre lasers can be configured in a parallel array to provide flexibility in pumping conditions and provide pump redundancy [23].

Various methods have been demonstrated to ensure robust single polarisation operation of fibre DFB lasers [24-26]. This robust single polarisation operation and stable wavelength with narrow linewidth are very desirable for sensor systems. Alternatively, DFB lasers can be made to operate in stable dual-polarisation so that simultaneous measurements can be carried out [27-29]. In addition to the sensing and telecom applications, we recently demonstrated the high power application of DFB fibre lasers [30] following the advances in the pump source technologies.

2.3. References

[1] H. Kogelnik and C. V. Shank, "Stimulated Emission in a Periodic Structure," *Applied Physics Letters*, vol. 12, no. 18, pp. 152-154, 1971.

[2] H. Kogelnik and C. V. Shank, "Coupled-wave Theory of Distributed Feedback Lasers," *Journal of Applied Physics*, vol. 43, no. 5, pp. 2327-2335, 1972.

[3] K. O. Hill, Y. Fujii, D. C. Johnson, and B. S. Kawasaki, "Photosensitivity in Optical Fiber Waveguides: Application to Reflection Filter Fabrication," *Applied Physics Letters*, vol. 32, no. 20, pp. 647-649, 1978.

[4] G. Meltz, W. W. Morey, and W. H. Glenn, "Formation of Bragg Gratings in Optical Fibers by a Transverse Holographic Method," *Optics Letters*, vol. 14, no. 15, pp. 823-825, 1989.

[5] G. A. Ball and W. W. Morey, "Continuously Tunable Single-Mode erbium Fiber Laser," *Optics Letters*, vol. 17, no. 6, pp. 420-422, 1992.

[6] J. L. Zyskind, V. Mizrahi, D. J. DiGiovanni, and J. W. Sulhoff, "Short Single Frequency erbium-Doped Fiber Laser," *Electronics Letters*, vol. 28, no. 15, pp. 1385-1387, 1992.

[7] K. O. Hill, B. Malo, F. Bilodeau, D. C. Johnson, and J. Albert, "Bragg Gratings Fabricated in Monomode Photosensitive Optical Fiber by Uv Exposure through a Phase Mask," *Applied Physics Letters*, vol. 62, no. 10, pp. 1035-1037, 1993.

[8] D. Z. Anderson, V. Mizrahi, T. Erdogan, and A. E. White, "Production of in-Fiber Gratings Using a Diffractive Optical- Element," *Electronics Letters*, vol. 29, no. 6, pp. 566-568, 1993.

[9] J. T. Kringlebotn, P. R. Morkel, L. Reekie, J. L. Archambault, and D. N. Payne, "Efficient Diode-Pumped Single Frequency erbium:ytterbium Fiber Laser," *IEEE Photonics Technology Letters*, vol. 5, no. 10, pp. 1162-1164, 1993.

[10] J. T. Kringlebotn, J. L. Archambault, L. Reekie, and D. N. Payne, "Er3+Yb3+ Codoped Fiber Distributed-Feedback Laser," *Optics Letters*, vol. 19, no. 24, pp. 2101-2103, 1994.

[11] M. J. Cole, H. Geiger, R. I. Laming, S. Y. Set, M. N. Zervas, W. H. Loh, and V. Gusmeroli, "Broadband dispersion-compensating chirped fibre Bragg gratings in a 10Gbit/s NRZ 110km non-dispersion-shifted fibre link operating at 1.55 mu m," *Electronics Letters*, vol. 33, no. 1, pp. 70-71, 1997.

[12] W. H. Loh, M. J. Cole, M. N. Zervas, S. Barcelos, and R. I. Laming, "Complex Grating Structures with Uniform Phase Masks Based on the Moving Fiber-Scanning Beam Technique," *Optics Letters*, vol. 20, no. 20, pp. 2051-2053, 1995.

[13] W. H. Loh and R. I. Laming, "1.55 um phase-shifted distributed feedback fibre laser," *Electronics Letters*, vol. 31, no. 17, pp. 1440-1442, 1995.

[14] M. Sejka, P. Varming, B. Hubner, and M. Kristensen, "Distributed feedback Er3+ doped fibre laser," *Electronics Letters*, vol. 31, no. 17, pp. 1445-1446, 1995.

[15] L. Dong, W. H. Loh, J. E. Caplen, J. D. Minelly, K. Hsu, and L. Reekie, "Efficient single-frequency fiber lasers with novel photosensitive Er/Yb optical fibers," *Optics Letters*, vol. 22, no. 10, pp. 694-696, 1997.

[16] V. C. Lauridsen, J. H. Povlsen, and P. Varming, "Design of DFB fibre lasers," *Electronics Letters*, vol. 34, no. 21, pp. 2028-2030, 1998.

[17] V. C. Lauridsen, J. H. Povlsen, and P. Varming, "Optimising erbium-doped DFB fibre laser length with respect to maximum output power," *Electronics Letters*, vol. 35, no. 4, pp. 300-302, 1999.

[18] M. Ibsen, E. Ronnekleiv, G. J. Cowle, M. O. Berendt, O. Hadeler, M. N. Zervas, and R. Laming, "Robust high power (>20mW) all-fibre DFB lasers with unidirectional and truly single polarisation outputs," presented at CLEO, Baltimore, USA, 1999,CWE4

[19] K. H. Yla-Jarkko and A. B. Grudinin, "Performance Limitations of High-Power DFB Fiber Lasers," *IEEE Photonics Technology Letters*, vol. 15, no. 2, pp. 191-193, 2003.

[20] J. Hubner, P. Varming, and M. Kristensen, "Five wavelength DFB fibre laser source for WDM systems," *Electronics Letters*, vol. 33, no. 2, pp. 139-140, 1997.

[21] M. Ibsen, S. U. Alam, M. N. Zervas, A. B. Grudinin, and D. N. Payne, "8-and 16-channel all-fiber DFB laser WDM transmitters with integrated pump redundancy," *IEEE Photonics Technology Letters*, vol. 11, no. 9, pp. 1114-1116, 1999.

[22] H. N. Poulsen, P. Varming, A. Buxens, A. T. Clausen, P. Munoz, P. Jeppesen, C. V. Poulsen, J. E. Pedersen, and L. Eskildsen, "1607 nm DFB fibre laser for optical communcation in the L-band," presented at ECOC, Nice, France, 1999, MoB2.1

[23] L. B. Fu, S. R., M. Ibsen, J. K. Sahu, J. N. Jang, S. U. Alam, J. Nilsson, D. J. Richardson, D. N. Payne, C. Codemard, S. Goncharov, I. Zalevsky, and A. B. Grudinin, "Fiber-DFB laser array pumped with a single 1-W CW Yb-Fibre Laser," *IEEE Photonics Technology Letters*, vol. 15, no. 5, pp. 655-657, 2003.

[24] Z. E. Haratjunian, W. H. Loh, R. I. Laming, and D. N. Payne, "Single Polarization Twisted Distributed Feedback Fiber Laser," *Electronics Letters*, vol. 32, no. 4, pp. 346-348, 1996.

[25] H. Storoy, B. Sahlgren, and R. Stubbe, "Single polarisation fibre DFB laser," *Electronics Letters*, vol. 33, no. 1, pp. 56-58, 1997.

[26] J. L. Philipsen, M. O. Berendt, P. Varming, V. C. Lauridsen, J. H. Povlsen, J. Hubner, M. Kristensen, and B. Palsdottir, "Polarisation control of DFB fibre laser using UV-induced birefringent phase-shift," *Electronics Letters*, vol. 34, no. 7, pp. 678-679, 1998.

[27] J. T. Kringlebotn, W. H. Loh, and R. I. Laming, "Polarimetric Er3+-doped fiber distributed-feedback laser sensor for differential pressure and force measurements," *Optics Letters*, vol. 21, no. 22, pp. 1869-1871, 1996.

[28] O. Hadeler, E. Ronnekleiv, M. Ibsen, and R. I. Laming, "Polarimetric Fiber Distibuted Feedback Laser Sensor for Simultaneous Strain and Temperature Measurements," *Applied Optics*, vol. 38, no. 10, pp. 1953-1958, 1999.

[29] O. Hadeler, M. Ibsen, and M. N. Zervas, "Distributied-feedback fiber laser sensor for simultaneous strain and temperature mesurements operating in the radio-frequency domain," *Applied Optics*, vol. 40, no. 19, pp. 3169-3175, 2001.

[30] C. A. Codemard, L. Hickey, K. Yelen, D. B. S. Soh, R. Wixey, M. Coker, M. N. Zervas, and J. Nilsson, "400 mW 1060 nm ytterbium doped fiber DFB laser," presented at Photonics West LASE, San Jose, California, USA, 2004, 5335-11

Chapter 3 Computational Methods

3.1. Introduction

As in the case of any simulation, the accuracy and the computation time are the two issues that have to be balanced in the calculation of the DFB laser characteristics. In this Chapter we will discuss the algorithms that allowed us to simulate gratings, rare-earth doped fibres and fibre lasers, typically with computation times less then 1 minute for device lengths up to 10 cm, using a standard PC with Pentium® 4 1.2GHz processor and 128 Mb RAM. Matlab© Ver. 6.1. was used for the implementation of the algorithms because of its very high performance for matrix-based calculations and the readily available mathematical library.

The simulation of a device requires the solution of two groups of equations, namely; the propagation equations for fields in the grating and the rate-equations of the active medium. When the grating apodisation profile is suitably defined, solution of these two sets of equations enables the simulation of fibre lasers with FP, DBR or DFB structures. In addition to the power characteristics, we can also simulate the laser threshold conditions and longitudinal signal and pump distributions.

Passive gratings can also be simulated by setting the loss to a constant value. In this case the reflection, transmission and time-delay spectra can be calculated. Alternatively, the grating can be ignored by setting the coupling coefficient to zero and free propagation in the rare-earth doped medium can be simulated.

3.2. Simulation of Propagation in Grating Structures

The main requirement for the simulation algorithm for propagation is the ability to work on any kind of grating, with arbitrary apodisation and chirp profiles, as well as with an arbitrary number of discreet phase-shifts, so that it will be possible to compare very different laser designs in our quest for maximum efficiency. For this purpose we employed the transfer matrix (T-matrix) method which has been used as a very powerful

tool for the analysis of complex laser structures [1-5]. The essence of the method is to divide a complex structure into small segments so that each segment can be assumed to be uniform, as illustrated in Figure 3-1.

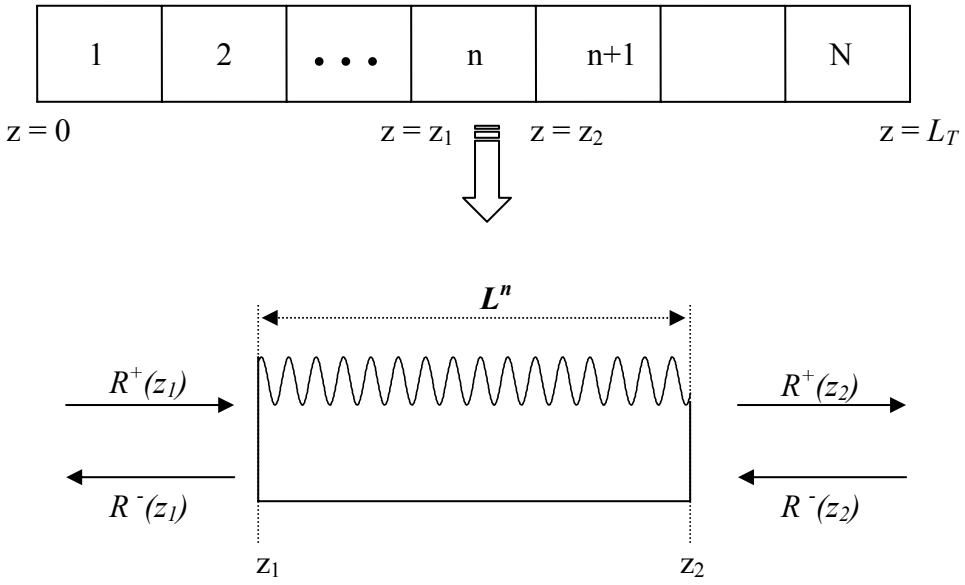

Figure 3-1 Transfer matrix method. A complex grating with arbitrary apodisation and chirping profile and discrete phase shifts is divided into N small segments so that each segment is approximately uniform.

If $\Psi^{+}(x,y)$ and $\Psi^{-}(x,y)$ are the transverse modal distributions, where (+) and (-) signs indicate the direction of propagation, then the total electric field $E(x,y,z)$ at a position is $E(x,y,z) = E^{+}(z)\Psi^{+}(x,y) + E^{-}(z)\Psi^{-}(x,y)$. The transfer matrix, T, of a uniform segment relates the electric fields on one side of the segment to the fields on the other side in the form:

$$\begin{bmatrix} E^{+}(z_1) \\ E^{-}(z_1) \end{bmatrix} = \begin{bmatrix} T_{11} & T_{12} \\ T_{21} & T_{22} \end{bmatrix} \begin{bmatrix} E^{+}(z_2) \\ E^{-}(z_2) \end{bmatrix} \tag{3.1}$$

We use the electric field amplitude envelopes, $R(z)$, to separate the slowly varying part form the fast modulated term, $e^{\beta z}$ and re-write the total electric field as:

$$E(x,y,z) = R^{+}(z)\Psi^{+}(x,y)e^{-i\beta^{+}z} + R^{-}(z)\Psi^{-}(x,y)e^{i\beta^{-}z} \tag{3.2}$$

where β^{+} and β^{-} are the propagation constants of the forward and backward propagating fields, respectively.

Starting from the coupled-wave equations, as given by Equations (6.2) and (6.3), the entries of the T-matrix for the uniform grating segment, n, in Figure 3-1 between $z = z_1$ and $z = z_2$ of length L^n are found as [2]:

$$T_{11}{}^n = \left[\cosh\left(\gamma L^n\right) + \frac{i\Delta\beta'}{\gamma}\sinh(\gamma L^n)\right] e^{i\beta_B L^n} \tag{3.3}$$

$$T_{12}{}^n = \frac{-\kappa}{\gamma}\sinh(\gamma L^n) e^{-i(\beta_B L^n + \phi^n)} \tag{3.4}$$

$$T_{21}{}^n = \frac{-\kappa}{\gamma}\sinh(\gamma L^n) e^{i(\beta_B L^n + \phi^n)} \tag{3.5}$$

$$T_{22}{}^n = \left[\cosh\left(\gamma L^n\right) - \frac{i\Delta\beta'}{\gamma}\sinh(\gamma L^n)\right] e^{-i\beta_B L^n} \tag{3.6}$$

where $\Delta\beta'$, γ and ϕ^n are defined as:

$$\begin{aligned} \Delta\beta' &= \Delta\beta + i\alpha \\ \gamma &= \sqrt{\kappa^2 - \left(\Delta\beta'\right)^2} \\ \phi^n &= \phi_{initial} + \sum_{j=1}^{n-1}\left(\frac{2\pi}{\Lambda^j} L^j\right) \end{aligned} \tag{3.7}$$

Here $\phi_{initial}$ is the initial phase of the grating at $z = 0$ and Λ is the period of the segment. $\Delta\beta$ is the deviation from the propagation constant, $\beta_B = 2\pi n_0/\lambda_B$, at the Bragg wavelength of the segment, given as $\lambda_B = 2n_0\Lambda$ where n_0 is the effective refractive index of the medium. In the equations positive α is the gain experienced by the field. ϕ^n is a piece-wise approximation of the grating phase defined in Equation (6.4) while the sinusoidal refractive index modulation given by Equations (6.6) results in the coupling coefficient κ as given in Equation (6.7). In our analysis we assume the initial phase of the grating at the origin to be 0 for the sake of simplicity.

The gain (loss) term, α, in these equations depends on the medium in which the fields propagate. If a constant gain (or loss) is assumed throughout the device then T-matrix entries for each segment are independent of the fields that are incident on the segments. However if the dynamics of the active medium is to be taken into account, which results in varying gain with field amplitudes, then for each segment the rate equations must be

solved as a function of the signal and pump power for the local α term and T-matrices become a function of distance and propagating fields.

3.2.1. Grating Simulation

A grating can be simulated for its reflection, transmission or time delay spectrum as a passive device. When calculating the spectra of a grating we assume an incident field from one of the ends. For example let us assume that a field propagating with wavelength λ in the positive direction $R^{+}(0)$ is incident on the grating at $z = 0$ and we want to calculate the reflected field $R^{-}(0)$. The T-matrix describing the entire grating of length L_T seen from $z = 0$, T_T, is found by multiplying the T-matrices of each segment in the positive direction:

$$T_T = T_1 T_2 ... T_n T_{n+1} ... T_N \tag{3.8}$$

so that:

$$\begin{bmatrix} R^{+}(0) \\ R^{-}(0) \end{bmatrix} = \begin{bmatrix} T_T \end{bmatrix} \begin{bmatrix} R^{+}(L_T) \\ R^{-}(L_T) \end{bmatrix} \tag{3.9}$$

Since there is no incident field at $z = L_T$, $R^{-}(L_T) = 0$. The reflection, r, and transmission, t, coefficients seen from $z = 0$ are found to be [2]:

$$r = \frac{T_{T21}}{T_{T11}} \tag{3.10}$$

$$t = \frac{1}{T_{T11}} \tag{3.11}$$

The reflected field at z = 0 is:

$$R^{-}(0) = rR^{+}(0) \tag{3.12}$$

Carrying out the same calculations at different wavelengths, the reflection and transmission spectra of the grating can be calculated.

The time delay experienced by the reflected field , τ_r , before it re-emerges and the penetration depth it travels into the grating , D, are defined as [6]:

$$\tau_r = \left| \frac{d\theta_r}{d\omega} \right| \tag{3.13}$$

$$D = \frac{c\tau_r}{2n_0} \tag{3.14}$$

where θ_r is the phase of the reflected field and ω is the angular frequency of the field, c is the speed of light in vacuum and n_0 is the effective refractive index of the medium. Therefore once the reflection spectrum, $r(\lambda)$, is known, calculation of the θ_r and consequently calculation of τ_r and D is straightforward.

The simulation of the spectral properties requires many wavelength iterations. We found a segment length around 0.5 mm (350 x Bragg wavelength) and a spectral resolution of 0.5 pm to provide satisfactory results in less than one minute using Matlab's array based calculations.

In addition to the spectral calculations, the spatial distribution of the fields inside the grating can also be calculated by employing the T-matrix method. Once the incident and reflected fields at one end are known, calculating the fields at the end of each segment gives the required spatial distribution with a resolution of the segment length.[7]. A similar approach can be used to calculate the reflection and transmission coefficients as well as time delays and penetration depths, not only at the ends of the grating but also inside the cavity. By doing so one can calculate the grating reflectivities or penetration depths, seen from a particular position inside the cavity. We will use this type of calculation extensively when we investigate the effects of the classic optimisation approach in Chapter 5.

For example, consider the location $z = z_2$ in Figure 3-1. By multiplying the transfer matrices of the segments seen from right to left in the decreasing order;

$$T_L = T_n^{-1} T_{n-1}^{-1} \ldots T_1^{-1} \tag{3.15}$$

and multiplying the transfer matrices from left to right

$$T_R = T_{n+1} T_{n+2} \ldots T_N \tag{3.16}$$

one can characterise the two grating sections to the left and to the right of the position z_2 respectively for their spectral behaviour. Note that with this formalisation, the reflection and transmission coefficients of the left-hand side grating seen from z_2 are;

$$r_L = \frac{L_{21}}{L_{22}} \quad ; \quad t_L = \frac{1}{L_{22}} \text{ and similarly; } r_R = \frac{R_{21}}{R_{11}} \quad ; \quad t_R = \frac{1}{R_{11}} \tag{3.17}$$

where L_{ij} and R_{ij} are the elements of matrices T_L and T_R. By applying this procedure at all the points between two adjacent segments it is possible to calculate the left- and right-hand reflection, transmission, time-delay and penetration depth spectra as a function of position in the cavity.

3.2.2. Threshold Simulation

Lasing of a device is the condition that occurs when finite signal outputs are observed without any input signals to the cavity. This is mathematically equivalent to an infinite transmission coefficient [2] i.e.:

$$t = \frac{1}{T_{T11}} \to \infty \tag{3.18}$$

that is at threshold:

$$T_{T11} = 0 \tag{3.19}$$

At the threshold the intensity build up inside the cavity will be minimal; therefore we can assume that the gain will be constant and given by the unsaturated small signal value throughout the entire cavity if the pump power is sufficiently large. With this assumption, we can vary the gain constant, α, and the wavelength, λ, and calculate the overall transfer matrix T_T in order to find (α,λ) pairs that make $T_{T11} = 0$. The pair with the smallest gain corresponds to the fundamental longitudinal mode and increasing threshold gain values satisfying the condition given by (3.18) correspond to the higher order modes of the cavity.

The algorithm for determining (α,λ) pair is a successive application of the "golden search" approach, which is based on narrowing the search range while increasing the resolution: Initially we define a range of wavelength, (λ_1,λ_2), with a certain resolution $\Delta\lambda$. We vary α at $\Delta\alpha$ steps and find the minimum $|T_{T11}|$ over this initial λ range (Figure 3-2). This

iteration gives a pair (α_i,λ_j). Then we reduce the wavelength range around λ_j with smaller $\Delta\lambda$ steps, and repeat the golden search with smaller $\Delta\alpha$ steps. We repeat the iteration until the minimum $|T_{T11}|$ calculated is less then the tolerance limit. The time required for the solution of threshold conditions strongly depends on the initial guess of the wavelength range. Investigation of the reflection and time-delay spectra of the total passive grating can improve this initial guess. In our simulations the typical time required for convergence is limited to a few minutes with a tolerance value of 10^{-4}.

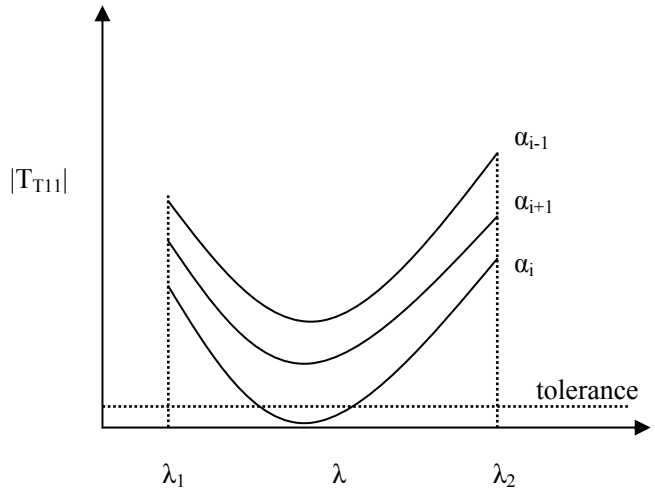

Figure 3-2 Solution for threshold. $|T_{T11}|$ is calculated over a wavelength range (λ_1, λ_2) with varying gain values. The minimum $|T_{T11}|$ is found for (α_i,λ_j). In the next iteration gain and wavelength resolution is increased around (α_i,λ_j) until $|T_{T11}|$ is smaller then the tolerance.

3.2.3. Normalised Modal Distribution

When the threshold condition (α,λ) is known the spatial distribution of the mode can be calculated easily. In contrast to the grating case, however, the fields at the ends are defined according to the laser boundary conditions, that is: There is no incident field at z = 0 and we assume a unit field output z = 0 so that the distribution will be normalised with the LHS output power:

$$R^{+}(0) = 0 \qquad R^{-}(0) = 1 \tag{3.20}$$

By using the constant threshold gain α and corresponding wavelength λ and starting from the left-hand side we evaluate the fields at the end of each segment to find the normalised distribution throughout the cavity.

3.2.4. Power Distributions

Simulation for the signal and pump distributions when the device is pumped above the threshold is a two-point boundary value problem. The two boundary conditions that must be met are zero incident fields at the left and right boundaries of the cavity. We use a shooting algorithm for the solution of this problem. The algorithm starts with an initial guess for the left output power with no left input as the first boundary condition. For the first segment the pump absorption and signal gain are calculated assuming constant pump and signal powers in the segment. Then the transfer matrix of the segment is calculated to find the fields at the end of the segment. Also the pump power arriving to the consecutive segment is calculated since the pump absorption and segment length is known. The same calculations are carried out for each segment until the last one, where the right-end output and input powers are calculated. The second boundary condition requires the right-end input to be zero. If this condition is not met then the initial guess for the left output power is varied until the right input power is smaller than a tolerance value.

When the simulation converges, it gives the forward and backward propagating signal power and pump power distributions as well as the gain and absorption distributions. The backward signal at the left-end corresponds to the left output power, and the forward signal at the right end corresponds to the right-end output. The pump power at the RHS end is the residual pump leaving the cavity.

These distributions are calculated at the lasing wavelength only therefore shorter segments can be used without compromising the computation speed. Typically we used segment lengths around 250 µm and iterations for a single pump power were completed in less than one minute.

3.3. Simulation of Active Medium

The segments in the T-matrix method are short, therefore in each segment we assume the pump and signal to be constant, and we solve the rate equations for the gain (absorption) coefficient. In the case of a simple active medium such as only Yb doped fibres, gain can be calculated by solving linear rate equations analytically. However, in the case of a Er/Yb co-doped medium the rate equations are non-linear due to the up-conversion terms, and a numerical solution method must be employed.

The transitions we will consider in Chapter 4 require solution of 8 steady state equations with non-linear coefficients, including the rate equations for quenched Yb ions

(Equations (4.1) – (4.8)) where N_i is the concentration of ions at the energy state i. In this set the most complex equations are for the N_1 and N_3 Er ions. For the solution algorithm we assume a range of values for N_3 and solve rate equations for N_2, N_4, N_5, N_6 and find N_1 from total ion concentration (See Figure 4-1 for details of the energy levels) . Finally we substitute all these results in the rate equation for N_1. If the results are correct then the N_1 equation should give 0 at the steady state, if not the result will have an error value Δ (Figure 3-3).

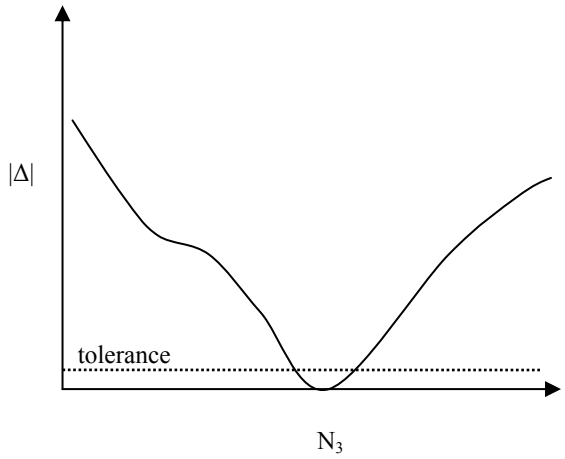

Figure 3-3 Solution of rate equations numerically reduced to one-dimensional minimisation problem by assuming values for N_3 and solving for concentrations in other levels. When they are substituted in the rate equation for N_1 the error $|\Delta|$ is a function of assumed N_3. The N_3 value making the error less then tolerance is the numerically found solution.

Therefore by scanning N_3 values, effectively we reduce the problem to a one dimensional minimisation problem. After each iteration we increase the resolution around the dip of the error curve until the minimum $|\Delta|$ is smaller than the tolerance value. In our implementation we used a tolerance level of 10^{-3} of total Er ion concentration.

3.4. Conclusions

We implemented simulation algorithms for the analysis of gratings, rare-earth doped fibres and lasers that provide solutions in practical times using a standard PC. The algorithms consist of two sets of equations, namely the propagation equations and the rate equations. The gain coefficient appearing in the transfer matrices for the propagation simulations is the link between these two sets of equations.

The simulation tool is versatile; it allows simulation of passive gratings or lasers with any chirp and apodisation profiles or phase-shifts. Proper definition of the apodisation profile permits the simulation of FP, DBR or DFB lasers. The reflection, transmission, time-delay

spectra, threshold conditions, signal and power distributions and power characteristics of these devices can be calculated.

The limit for practical computation time is set by the length of the device. Longer devices require larger number of segments to be used if the same spatial resolution is to be preserved. However, this would increase the computation time. Alternatively, if the device is long, longer segments can be used, which will lead to reduced spatial resolution and accuracy, while keeping the computation time short. Similarly, spectral analyses require multi-wavelength computations therefore a longer segment length is needed in order to keep the computation time practical.

3.5. References

[1] G. Bjork and O. Nilsson, "A New Exact and Efficient Numerical Matrix-Theory of Complicated Laser Structures - Properties of Asymmetric Phase- Shifted Dfb Lasers," *Journal of Lightwave Technology*, vol. 5, no. 1, pp. 140-146, 1987.

[2] M. Yamada and K. Sakuda, "Adjustable gain and bandwidth light amplifiers in terms of distributed-feedback structures," *Journal of the Optical Society of America a-Optics Image Science and Vision*, vol. 4, no. 1, pp. 69-76, 1987.

[3] M. Yamada and K. Sakuda, "Analysis of Almost-periodic Distributed Feedback Slab Waveguides via a Fundamental Matrix Approach," *Applied Optics*, vol. 26, no. 16, pp. 3474-3478, 1987.

[4] B. G. Kim and E. Garmire, "Comparisaon between the matrix method and the coupled-wave method in the analysis of Bragg reflector structures," *Journal of Optical Society of America A*, vol. 9, no. 1, pp. 132-136, 1992.

[5] S. Radic, N. Georges, and G. P. Agrawal, "Analysis of Nonuniform Nonlinear Distributed Feedback Structures: Generalized Transfer Matrix Method," *IEEE Journal of Quantum Electronics*, vol. 31, no. 7, pp. 1326-1336, 1995.

[6] D. I. Babic and W. Corzine, "Analytic Expressions for the Reflection Delay, Penetration Depth, and Absorptance of Quarter-Wave Dielectric Mirrors," *IEEE Journal of Quantum Electronics*, vol. 28, no. 2, pp. 514-524, 1992.

[7] M. A. Muriel, A. Carballar, and J. Azana, "Field distributions inside fiber gratings," *IEEE Journal of Quantum Electronics*, vol. 35, no. 4, pp. 548-558, 1999.

Chapter 4 Modelling of Erbium Ytterbium Co-Doped DFB Fibre Lasers

4.1. Introduction

An analytical model of a device or a system is a very powerful tool for the design and performance optimisation. Models can be used to calculate the behaviour of the device/system under different operating conditions to reduce the design and development time and cost significantly. In addition to being a design tool, a model can also help to improve the physical insight for the device or system under investigation by allowing one to carry out calculations and hypothetical experiments which in many cases can be extremely difficult in laboratory conditions. The value of any simulation result should be judged according to its closeness to the behaviour of the real device or system. Closer predictions to the *reality* over a broader range of conditions make a model superior to other models aiming to describe the same device or system. Therefore, in order to be able to judge the usefulness of a model and its relevance, it is essential to check the predicted results against the experimental data.

Three main difficulties can be identified in optical device modelling. The first difficulty is the large number of equations required to describe a real system and often some phenomena may escape attention. The second difficulty is the solution of these equations; whether it is analytical or numerical, solution techniques usually require simplifications and approximations. And finally, the third difficulty is the measurement of the actual values of the parameters and coefficients that appear in these equations.

The erbium-ytterbium co-doped fibre DFB laser is an important device finding applications in many areas ranging from telecom [1-3] to sensors [4-6]. Therefore, speeding up the design process and cutting the costs through the simulations is quite valuable. However, the required model is subject to the difficulties mentioned: When pumped around 980 nm and operating around 1550 nm, an Er/Yb co-doped medium allows multiple interactions between ions and propagating fields[7]. In addition to the basic absorption and emission transitions of a quasi-three level system, there is energy transfer between Er and Yb ions, in both directions, the excited state absorption (ESA)

of both pump and signal is possible, co-operative up conversion (CUP) for ions at various excited states is allowed which may be two-, three- or many- ion interactions, the relaxation of excited ions can be through phonon emission as well as spontaneous emission such as at green light wavelengths. Also life-time quenching of Yb ions has been reported [8]. Therefore, the full description of all possible transition routes requires a very large number of equations, which corresponds to the first difficulty in a modelling effort that we mentioned.

Ignoring some of the less significant transitions, a set of equations was reported to successfully model the Er/Yb doped medium in the amplifier regime[9]. Even in this reduced model, calculation techniques may require further simplifications and approximations in order for the calculation to be completed in practical times, giving rise to the second of the challenges in the model-reality relation. Investigations on the implications of these simplifications on an already reduced model have been reported [10, 11]. In these studies a rather misleading terminology is used: the *simplified* solutions are compared to the *exact* solutions, which are the solutions to the more detailed equations, but as we just discussed even these are not the *exact* solutions since one would need to consider all of the possible transitions and interactions to find the exact solutions. Critically, one must also address the actual values of the ignored parameters since any simplification is acceptable only if its impact is small compared to other interactions.

Finally the third obstacle we address is the determination of the parameters. The measurement of the active medium properties requires detailed spectroscopic investigation [12, 13] and data usually represent the combined effect of various parameters. Therefore, certain assumptions and fitting of some parameters cannot be avoided.

If any of these three issues is not tackled adequately then the simulation results will make sense only in terms of *tendencies*, instead of the actual numbers and only general comments can be inferred. Although several entirely theoretical studies on modelling of erbium ytterbium co-doped media have been reported [7, 10, 11, 14-17] with only very few experimental verification for amplifiers [9, 18] there is no work benchmarking the simulation results with experimental results for an Er/Yb co-doped laser, whether in Fabry-Perot, DBR or DFB configuration.

In this Chapter, we present a model for Er/Yb co-doped fibre DFB lasers with a minimum number of critical transitions and describe simple techniques to measure the required

parameters. We characterise the pump, the active medium and the grating individually. For the first time, we present simulations that predict actual characteristics of the Er/Yb co-doped DFB fibre lasers within the range of experimental measurement errors.

4.2. Characterisation of Active Medium

4.2.1. Analytical Model

The Er/Yb co-doped medium is described by a set of rate equations derived from the transitions between energy levels due to ion – ion and ion – light interactions. The ion – ion interactions that we consider are co-operative up conversion (CUP) among Er ions and energy transfer between Er and Yb ions. In both cases we assume that a two-ion interaction takes place, although it is possible that more ions are exchanging energy at the same time. Ion – light interactions include absorption at the ground state, stimulated emission, and absorption at an excited state (ESA). In addition to these transitions we also consider spontaneous emission and non-radiative transitions.

In principle any energy transfer between ions and propagating fields is possible as long as there is an energy band that can accommodate the ions. The ideal analytical model should consider all the possible routes. However, this would lead to extremely complex equations whose parameters are practically impossible to measure. Therefore we only focused on the transitions that are reported to have observable effects. Figure 4-1 shows these transitions and Table 4-1 details the mechanisms behind them. Also, in reality the cross-sections vary with temperature [19, 20] . In our model we neglect this effect for the sake of simplicity. Here N_1 is the concentration of the Er ions at $^4I_{15/2}$ level. An ion at this energy level is indicated by Er_1 in Table 4-1 below. Similarly N_2 stands for the concentration at $^4I_{13/2}$, N_3 $^4I_{11/2}$, N_4 $^2H_{11/2}$ and $^4S_{3/2}$ together. For Yb ions N_5 is the concentration at $^2F_{7/2}$ and N_6 at $^2I_{5/2}$. Again Er_2, Er_3, Er_4, Yb_5, Yb_6 stand for a single ion at the corresponding level. In our model we neglect the time Er ions spend at $^4I_{9/2}$ level indicated with the horizontal dashed-line, therefore it does not appear in the rate equations.

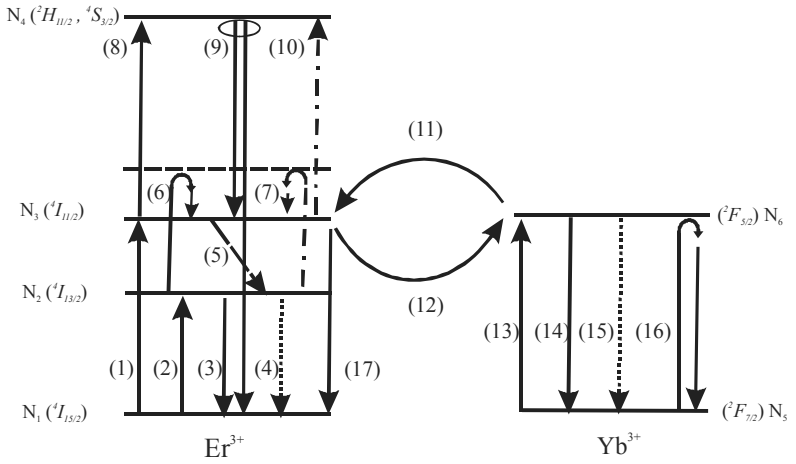

Figure 4-1 The energy scheme of Er and Yb ions. Arrows with dash and dot indicate cooperative up-conversion, dotted lines are used for spontaneous emission.

In Table 4-1 below, energy exchange due to a photon at the pump or signal wavelength are indicated with $h\nu_p$ and $h\nu_s$, respectively, whereas $h\nu_{green}$ indicates a photon emitted between 514 – 532 nm in the green light range, which was observed during experiments with this particular fibre when 980 nm pumping was used. An unassigned $h\nu$ indicates a spontaneous emission of photon at any possible wavelength.

#	*Transition Type*	*Transition Detail*
1	Absorption (Pump)	$Er_1 + h\nu_p \rightarrow Er_3$
2	Absorption (Signal)	$Er_1 + h\nu_s \rightarrow Er_2$
3	Stimulated Emission (Signal)	$Er_2 + h\nu_s \rightarrow Er_1 + 2\ h\nu_s$
4	Spontaneous Emission	$Er_2 \rightarrow Er_1 + h\nu$
5	Non-radiative Decay	$Er_3 \rightarrow Er_2 +$ phonons
6	ESA (Signal) and Fast Decay	$Er_2 + h\nu_s \rightarrow Er_3 +$ phonons
7	CUC and Fast Decay	$Er_2 + Er_2 \rightarrow Er_1 + Er_3 +$ phonons
8	ESA (Pump)	$Er_3 + h\nu_p \rightarrow Er_4$
9	Radiative and Non-radiative Decay	$Er_4 \rightarrow Er_3 + h\nu_{green} + Er_1 +$ phonons
10	CUC	$Er_3 + Er_3 \rightarrow Er_1 + Er_4$
11	Yb to Er Energy Transfer (Forward)	$Yb_6 + Er_1 \rightarrow Yb_5 + Er_3$
12	Er to Yb Energy Transfer (Backward)	$Er_3 + Yb_5 \rightarrow Yb_6 + Er_1$
13	Absorption (Pump)	$Yb_5 + h\nu_p \rightarrow Yb_6$
14	Stimulated Emission (Pump)	$Yb_6 + h\nu_p \rightarrow Yb_5 + 2\ h\nu_p$
15	Spontaneous Emission	$Yb_6 \rightarrow Yb_5 + h\nu$
16	Absorp. & Nonrad. Trans. In Quenched Ions	$Yb_5 + h\nu_p \rightarrow Yb_5 +$ phonons
17	Stimulated Emission (Pump) = 0 for 980 nm pump	$Er_3 + h\nu_p \rightarrow Er_1 + 2\ h\nu_p$

Table 4-1 Description of transitions in Figure 4-1

These transitions result in the following rate equations that should be equal to zero at steady-state:

$$\frac{dN_1}{dt} = N_2R_{21} + N_4R_{41} + k_{tr}N_3N_5 + C_{UP,2}N_2^{\,2} + C_{UP,3}N_3^{\,2} - N_1R_{13} - N_1R_{12} - k_{tr}N_6N_1 = 0 \tag{4.1}$$

$$\frac{dN_2}{dt} = N_3R_{32} + N_1R_{12} - N_2R_{21} - 2C_{UP,2}N_2^{\,2} - R_{ESA,2}N_2 = 0 \tag{4.2}$$

$$\frac{dN_3}{dt} = N_1R_{13} + k_{tr}N_6N_1 + R_{ESA,2}N_2 + C_{UP,2}N_2^{\,2} + N_4R_{43} - N_3R_{32} - k_{tr}N_5N_3 - 2C_{UP,3}N_3^{\,2} - R_{ESA,3}N_3 = 0 \tag{4.3}$$

$$\frac{dN_4}{dt} = C_{UP,3}N_3^{\,2} + R_{ESA,3}N_3 - N_4R_{41} - N_4R_{43} = 0 \tag{4.4}$$

$$\frac{dN_{5,n}}{dt} = N_{6,n}R_{65} + k_{tr}N_{6,n}N_1 - N_{5,n}R_{56} - k_{tr}N_3N_{5,n} = 0$$
$$\frac{dN_{5,q}}{dt} = N_{6,q}R_q - N_{5,q}R_{56} \tag{4.5}$$

$$N_{6,n} = N^{Yb}{}_n - N_{5,n} \qquad N_{6,q} = N^{Yb}{}_q - N_{5,q} \tag{4.6}$$

$$N_1 + N_2 + N_3 + N_4 = N^{Er} \tag{4.7}$$

$$N_{5,n} + N_{6,n} + N_{5,q} + N_{6,q} = N^{Yb} \tag{4.8}$$

Here R_{xy} stands for the transition rate from level x to level y and individual definitions of these rates are given below.

$$R_{12} = \frac{I_s \sigma^{Er}_{s,a}}{h\nu_s} \quad , \quad R_{13} = \frac{I_p \sigma^{Er}_{p,a}}{h\nu_p}$$

$$R_{21} = \frac{I_s \sigma^{Er}_{s,e}}{h\nu_s} + \frac{1}{\tau_2} \quad , \quad R_{ESA,2} = \frac{I_s \sigma^{Er}_{ESA,2}}{h\nu_s}$$

$$R_{31} = \frac{I_p \sigma^{Er}_{p,e}}{h\nu_p} \quad , \quad R_{ESA,3} = \frac{I_p \sigma^{Er}_{ESA,3}}{h\nu_p}$$

$$R_{32} = \frac{1}{\tau_3}$$

$$R_{56,n} = \frac{I_p \sigma^{Yb}_{p,a}}{h\nu_p} \quad , \quad R_{65,n} = \frac{I_p \sigma^{Yb}_{p,e}}{h\nu_p} + \frac{1}{\tau_{6,normal}}$$

$$R_{56,q} = \frac{I_p \sigma^{Yb}_{p,a}}{h\nu_p} \quad , \quad R_{65,q} = \frac{I_p \sigma^{Yb}_{p,e}}{h\nu_p} + \frac{1}{\tau_{6,quenched}}$$

In the rate equations for Yb ions subscript n stands for the normal ions and q denotes the life-time-quenched ions. The need to separate the Yb concentration in normal and quenched sub-groups will be justified after the full spectroscopy and absorption at the pump wavelength is considered later in Section 4.2.3. Above, h is Planck's constant, I is the intensity, σ is the cross-section, ν is the frequency, τ is the life-time, sub-scripts a and e are absorption and emission, p and s denote pump and signal respectively, and numbers follow the numbering of levels in Figure 4-1. $C_{ESA,x}$ and $C_{UP,x}$ are ESA cross-section and up conversion rates from level x respectively and k_{tr} is the energy transfer coefficient between Er and Yb ions in both directions. For radiative green light transition, R_{41}, from level 4 and a non-radiative transition, R_{43}, we use the average constant values 10^3 s^{-1} and $14x10^5$ s^{-1} respectively[21].

Equations (4.1) - (4.8) can be solved numerically to provide the steady-state values of the population concentrations for given signal and pump intensities. In our implementation, we assume a value for N_3 and substitute this in (4.4) to solve for N_4. Then Equations (4.2) and (4.7) are used to solve for N_1 and N_2. Finally, Equations (4.5), (4.6) and (4.8) are used to find $N_{5,n}$, $N_{6,n}$, $N_{5,q}$ and $N_{6,q}$. We check the validity of our initial assumption for N_3 by substituting N_1, N_2, N_3, N_5, N_6 in (4.1); If the assumption is correct then the result should be zero. We vary the N_3 value until Equation (4.1) is smaller than a tolerance value (See Section 3.3. for the solution algorithm).

4.2.2. Fibre Composition and Geometry

The fibre is produced using a Modified Chemical Vapour Deposition (MCVD) technique [22]. The core of the fibre is a phosphosilicate glass doped with Er, Yb and aluminium.

This active core is surrounded by a photosensitive germanosilicate ring doped with boron that matches the refractive index of the silica cladding. Figure 4-2 illustrates the geometrical properties of the fibre.

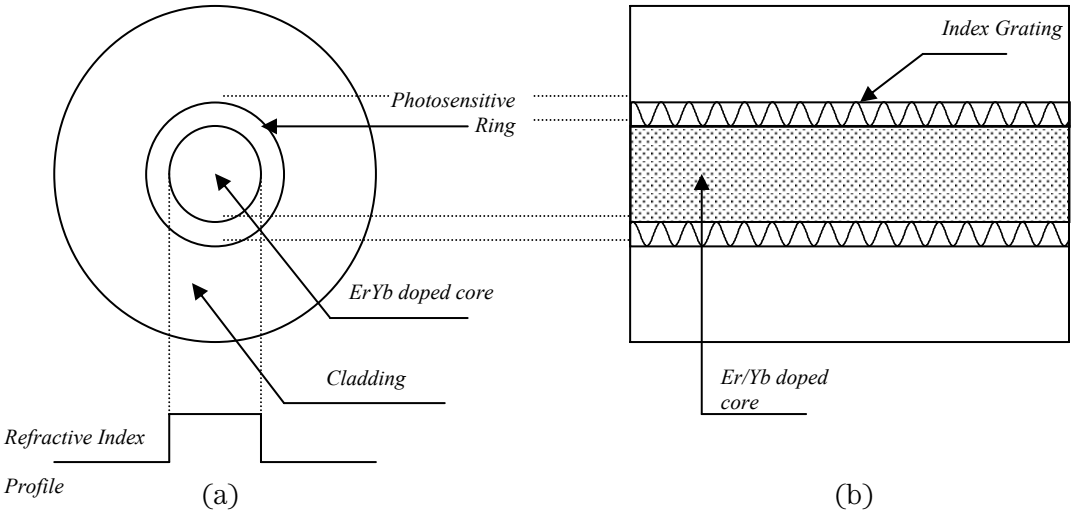

Figure 4-2 Structure of the Er/Yb doped photosensitive fibre (a) Cross section: Refractive index assumed to have a step profile. (b) Longitudinal view : Grating is in the photosensitive ring surrounding the core.

The core radius of the fibre is 2.3 µm and the cut-off wavelength is 1150 nm, giving NA = 0.1921. Refractive index of cladding (n_2) is 1.4585 and we calculate the core index (n_1) to be 1.4709. In our simulations we assume the refractive index distribution to have a step profile across the cross-section of the fibre. We also assume the dopants to be uniformly distributed in the core and to be homogeneously broadened. The refractive index grating is written in the photosensitive ring by exposing the fibre to an ultraviolet (UV) interference pattern produced by a phase-mask [23].

4.2.3. Spectroscopy at Pump Wavelength

In the absence of a grating if a signal with power P_S and a pump with power P_P propagate in an active medium in the + z direction then the propagation equations are of the form:

$$\frac{dP_S}{dz} = 2\alpha_s(z)P_S(z) \quad , \quad \frac{dP_P}{dz} = -2\alpha_p(z)P_P(z) \tag{4.9}$$

where α_s and α_p are the gain and the absorption coefficients for the signal and pump fields reflectively.

The fibre DFB lasers we investigate are pumped at around 980 nm. Around this wavelength the Yb absorption is the largest, which leads to the maximum energy transfer

from pump to signal over the shortest length. The total pump absorption coefficient, $2\alpha_p$, by both Yb and Er ions is given by:

$$2\alpha_p = \left(N_5 \sigma^{Yb}{}_{p,a} - N_6 \sigma^{Yb}{}_{p,e} + N_1 \sigma^{Er}{}_{p,a} - N_3 \sigma^{Er}{}_{p,e} + N_3 C_{ESA,3} \right) \Gamma_p + 2\alpha_{p,background} \quad (4.10)$$

where Γ_p is the overlap coefficient between the pump power distribution and the active medium cross section. $\alpha_{P,background}$ stands for any constant background loss at the pump wavelength. If the pump power is very small then at steady-state only a small fraction of the ions will be in their excited energy levels. In Equation (4.10) the number of excited Yb ions is denoted with N_6 and the number of excited Er ions is N_3. If we neglect these terms for small pump powers, when practically all the ions are in their ground state, then the absorption coefficient can be approximated with

$$2\alpha_p \approx \left(N^{Yb} \sigma^{Yb}{}_{p,a} + N^{Er} \sigma^{Er}{}_{p,a} \right) \Gamma_p$$

assuming the background loss is small compared to the absorption by the ions. Around 980 nm, the Yb absorption cross-section is significantly larger than the Er absorption cross-section. In addition to this, in the fibre we investigate a larger concentration of Yb was used compared to Er, in order to reduce quenching of Er ions [13] and to optimise the energy transfer. From the production of the fibre we know that the concentration of Yb will be more than 10 times larger compared to the Er concentration. Therefore we can further simplify the absorption coefficient to:

$$2\alpha_p \approx N^{Yb} \sigma^{Yb}{}_{p,a} \Gamma_p \quad (4.11)$$

We applied the cut-back method in order to measure the absorption coefficient, $2\alpha_p$, of the fibre at low pump powers. We used a tunable semiconductor laser as the pump source and measured its output power as -55 dBm over the range of 950 – 1000 nm by directly connecting the laser to a photo-detector. Then we spliced a 15.5 mm-long Er-Yb co-doped fibre between the pump source and the detector and measured the transmitted power. We re-measured the transmitted power after removing 4, 8 and 10 mm long pieces of fibre. We calculated the pump absorption in each case by comparing the transmitted power when the fibre was present with the power measured without the fibre. Figure 4-3 shows the results of this experiment after an estimated 0.5 dB splice loss was subtracted.

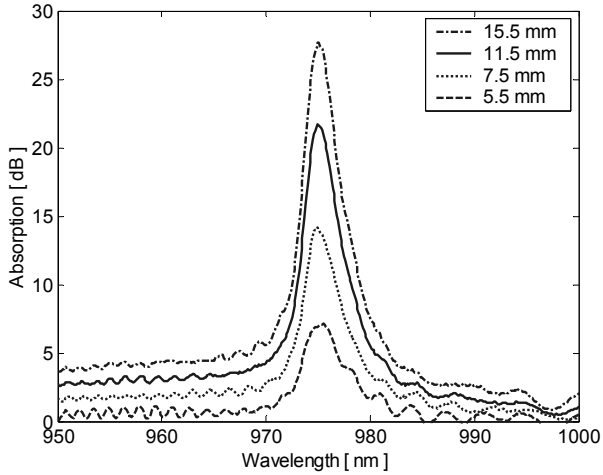

Figure 4-3 Pump absorption in the Er/Yb co-doped fibres of different length.

By comparing the absorption by different lengths of fibre segments with each other we obtained an average value of the absorption per unit length. Although the pump power is delivered to the fibre in single-mode, the Er/Yb co-doped fibre has a varying V value from 2.89 to 2.74 for wavelengths 950 – 1000 nm; therefore the pump power is divided into two modes. Since the fibre lengths we used were short, we assumed that 90% of the pump power remained in the fundamental mode and 10% was in the higher mode. Calculating the wavelength dependent overlap coefficient $\Gamma_p(\lambda)$ and substituting the measured absorption coefficient in Equation (4.11) we calculated the $N^{Yb}\sigma^{Yb}_{p,a}(\lambda)$ term (see Figure 4-4).

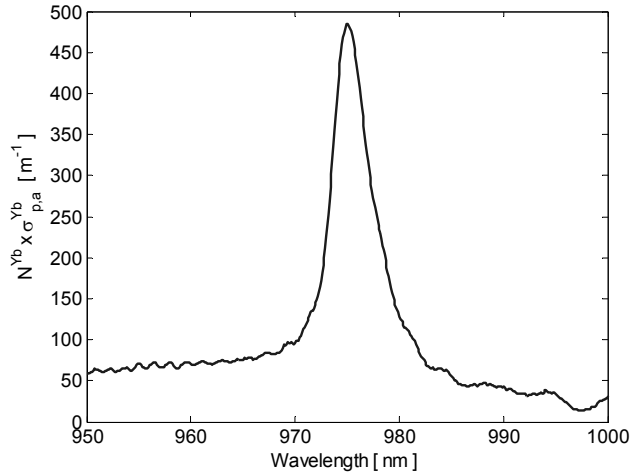

Figure 4-4 Average pump absorption per unit length.

The small-power absorption coefficient given in Figure 4-4 is a result of the combined effect of the total concentration and the absorption cross-section of Yb ions; therefore one needs to choose either one of them as the fitting parameter, and the other one will

be derived from Equation (4.11). We will use total Yb concentration, N^{Yb}, as the fitting parameter and derive the absorption cross-section, so that we can justify our assumption by comparing the resulting spectra with the previously reported values.

If the parameters are accurate enough then the model should also be able to predict high power absorption characteristics. Therefore, we also measured pump absorption of the fibre at high powers. We used a semiconductor laser of wavelength 979 nm whose output power could be varied from 0 to 240 mW. We again applied the cut-back method in order to calculate absorption per unit length of the fibre at high powers. By comparing the pump power before and after a segment we were able to calculate the pump power dependent absorption of the segment. Since the removed segment lengths were short, we assumed that the pump power was constant along the removed fibre segment.

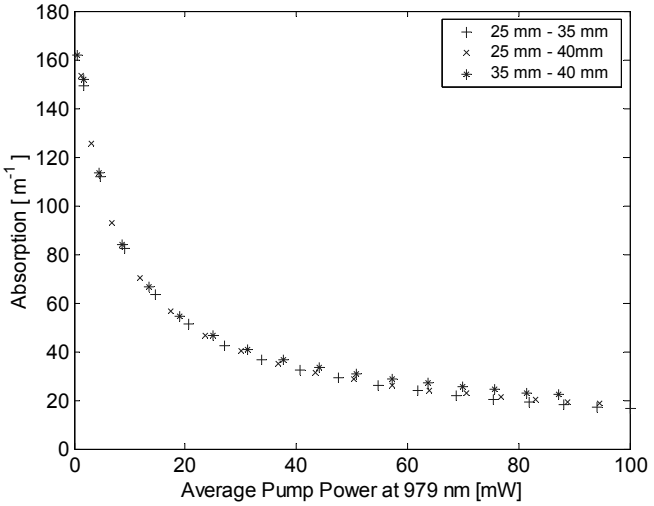

Figure 4-5 Variation of absorption with pump power. The data were obtained by comparing the pump powers leaving different lengths of fibres (25-35mm, 25-40mm, 35-40mm). The figure indicates the existence of an unsaturable loss around 20 m^{-1}.

Figure 4-5 shows the variation of absorption per unit length with the increasing pump power. Each mark in the figure gives the absorption calculated by comparing the transmitted power by two different fibre lengths. (+) is obtained by comparing the transmitted powers at the end of 25 and 35mm long fibres, (x) compares 25 and 40 mm long fibres and (*) compares 35 and 40 mm long fibres. As the pump power increases absorption decreases due to saturation of the medium: with increasing pump power more of the Yb ions move to the excited state however there is only a finite number of ions therefore in the ground state fewer ions remain for further absorption, consequently the absorption drops.

However, the results of this experiment at the high power end show a non-typical saturation behaviour. Although saturation is clearly observed, absorption does not drop to very small values, which should be the case if only a small background loss is present in the system. In the present case the absorption, $2\alpha_p$, becomes asymptotic to a significantly large value around 20 m^{-1} (87 dB/m).

This value is too large to be a constant background loss due to fibre impurities or splicing losses. This loss may be a result of the intrinsic Er or Yb transition dynamics in the medium. If this is the case we expect it to be related to Yb ions since the concentration, as well as, the absorption cross-section of Yb ions at this particular wavelength are significantly larger than that of Er ions. In order to check this assumption, we measured the saturation characteristics of only Yb doped fibres produced by the same method using the same facilities and we observed similar significant unsaturable loss values at large powers as shown in Figure 4-6.

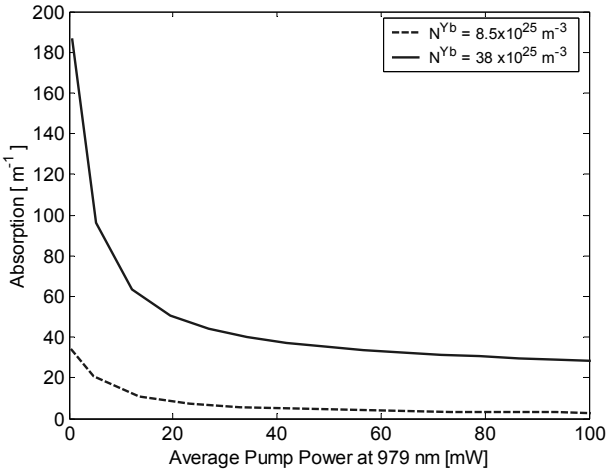

Figure 4-6 Absorption saturation characteristics of Yb-only doped fibres, produced in the way as the Er/Yb doped fibre. Both fibres exhibit an unsaturable loss.

Figure 4-6 shows that the larger the Yb concentration, the larger the amount of unsaturable loss. The fibre with lower Yb concentration ($8.5x10^{25}$ m^{-3}) exhibited an unsaturable loss $2\alpha_{unsaturable}$ = 3 m^{-1} (13 dB/m), whereas for the fibre with large Yb concentration ($38x10^{25}$ m^{-3}) this value was as large as 30 m^{-1} (130 dB/m). The unsaturable loss phenomenon in Yb- only doped media has been reported previously [8, 24, 25]. Although the exact mechanism behind this absorption has not been explained yet, the overall effect appears to be due to life-time quenching of a portion of Yb ions. Extremely small life- time causes the excited state ions to return to ground state very quickly through some non-radiative relaxation. Since this cycle is completed very fast, absorption

due to the quenched ions appears to be an unsaturable loss in addition to normal Yb saturable absorption[8].

In modelling accurately the performance of Er/Yb codoped DFB lasers we tried to account for the observed unsaturable loss by considering the excited state absorption and the co-operative up conversion in Er ions. But in order to get reasonable agreement with the experimental data the required parameters describing these secondary transitions had to be well out of the range reported in the literature. Therefore, we conclude that the unsaturable loss in the Er/Yb doped fibre around 980 nm was related to the life-time quenching of Yb ions. If we assume that the life-time quenched Yb ions are practically always in the ground state then we can write:

$$2\alpha_{unsaturable} \approx N^{Yb}{}_{quenched}\sigma^{Yb}{}_{p,a}\Gamma_p \qquad (4.12)$$

When we set the total Yb concentration, then Equation (4.11) and experimental data, shown in Figure 4-4, give the absorption cross-section, $\sigma^{Yb}{}_{p,a}$. Substituting this value in Equation (4.12) we can calculate the concentration of quenched ions, $N^{Yb}{}_{quenched}$. In doing so, we assume that normal and quenched Yb ions have the same emission and absorption cross-sections and only differ in their upper laser level life-times.

For the Er/Yb co-doped fibre, we achieved the best agreement between simulation and experimental results when $N^{Yb} = 34\text{x}10^{25}$ m^{-3}. The low pump power experiment then gives $\sigma^{Yb}{}_{p,a}(979\text{nm}) = 5.89\text{x}10^{-25}$ m^{-2}, and 22 m^{-1} unsaturable loss requires 11% of total Yb ions to be quenched. We again use Equation(4.11) and the data in Figure 4-4 in order to calculate the absorption cross-section spectrum of the Yb ions. The results are shown in Figure 4-7 with the solid curve.

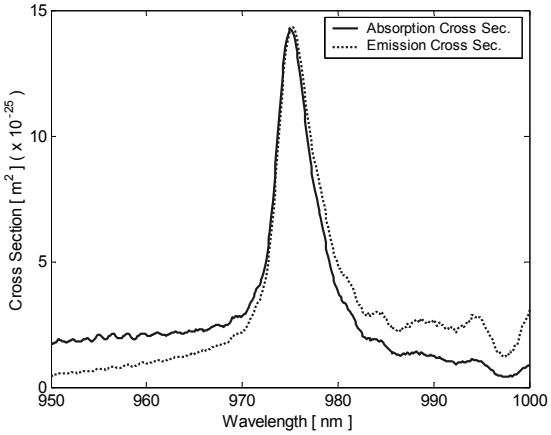

Figure 4-7 Calculated absorption (solid line) and emission (dotted line) cross-sections of Yb ions. Absorption cross-section is calculated from the experimental absorption spectrum and the emission cross-section is derived using McCumber Theory.

Figure 4-7 also shows the emission cross-section of Yb ions calculated by using McCumber theory (for example see [26]), assuming that emission and absorption cross-sections are equal at 975 nm [27]. Both cross-sections spectra are within the range of values reported previously [27-29]

4.2.4. Spectroscopy at Signal Wavelength

In the Er/Yb co-doped media, the signal is generated by the Er ions in the excited state undergoing radiative transitions. Using a low power white light source we measured the absorption spectra of the fibres between 1400-1600 nm, a range over which Yb ions are transparent. At low powers we can assume that all the Er ions are in the ground state therefore we can neglect any emission or excited state absorption, or any up-conversion from excited states. In this case, absorption of signal $2\alpha_s$ can be used to determine the total ion concentration times the absorption cross-section:

$$N^{Er}\sigma^{Er}_{s,a} \approx \frac{2\alpha_s}{\Gamma_s} \tag{4.13}$$

where Γ_s is the overlap between the active medium and the signal power distribution at the considered wavelength.

First we measured the white light source's output spectrum without any fibre attached, to obtain the calibration data. Then by introducing the fibre between the source and the detector and by gradually removing small lengths we applied the cut-back method to find the absorption per unit length as shown in Figure 4-8(a). Calculating $\Gamma_s(\lambda)$, and assuming N^{Er}=3x10^{25} m^{-3} Equation (4.13) gives the absorption cross-section spectrum of Er ions as shown in Figure 4-8(b) with the solid line.

The absorption outside the absorption spectrum of both Er and Yb ions (between 1250 and 1400 nm) is the constant background loss due to the fibre impurities and splicing losses. We measured this background loss as 0.15 m^{-1} (0.65 dB/m). Again we used McCumber theory in order to calculate the emission cross-section assuming emission and absorption cross-sections are equal at 1535 nm [30] . The emission cross-section is plotted in Figure 4-8(b) with a dotted curve. Resulting spectra are comparable to previously reported spectra [30-32].

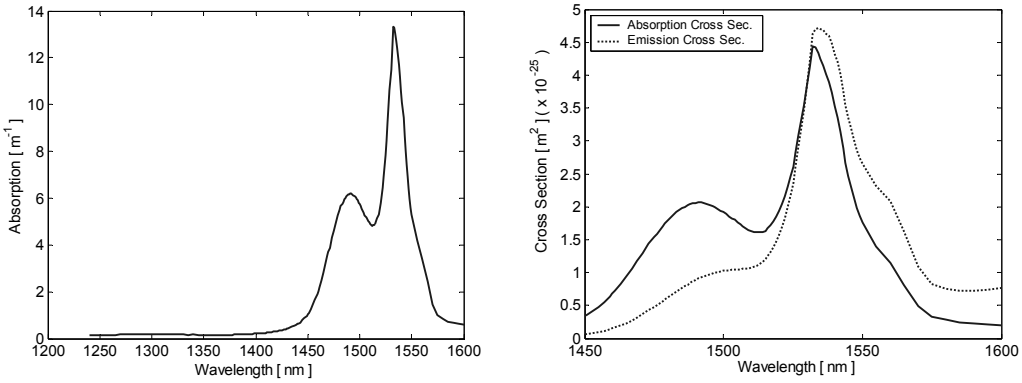

(a) (b)

Figure 4-8 (a) Absorption spectrum of Er ions, measured using a white source and employing the cut-back method. Absorption value at wavelengths lower than 1400 nm indicates a background loss of 0.15 m^{-1}, since at these wavelengths both Er and Yb ions are transparent. (b) Absorption (solid line) and emission (dotted line) cross-section. Emission spectrum is calculated using McCumber Theory.

4.3. Characterisation of the Grating

The lasing action in a DFB laser is a result of two combined phenomena; signal generation by the active medium and feedback by the grating. Therefore in addition to the active medium parameters, realistic simulation of a DFB laser requires information about the grating. We acquire this information by analysing the reflection spectrum of the DFB laser under investigation.

The grating writing procedure we consider is based on a moving translation stage and a stationary phase mask [23]. In this setup a fibre with a photosensitive ring surrounding the active medium is attached to the translation stage, and a section of grating is written by illuminating the fibre with the UV interference pattern generated by the mask for a fixed exposure time. Then the translation stage is moved in such a way that the next grating section can be written with the desired phase relation to the previous section. Any desired apodisation profile is achieved by precisely controlling constructive or destructive superpositioning of consecutive exposures. Changing the overall exposure time changes the refractive index modulation depth therefore scales the apodisation profile. The grating writing technique guarantees the shape of the apodisation, however, in addition to the exposure time, the absolute value of the scaling varies due to the variations in the alignment between the fibre and the UV interference pattern, and also due to variations in the photosensitivity of the fibre.

Figure 4-9 (a) illustrates an apodisation profile with three different scales that can be written due to different UV powers delivered or variations in the photosensitivity. The sign change in the apodisation profile is equivalent to a π-shift in the phase of the grating.

This shift is introduced by intentionally washing out a $\Lambda/4$-long grating section where Λ is the period of the grating.

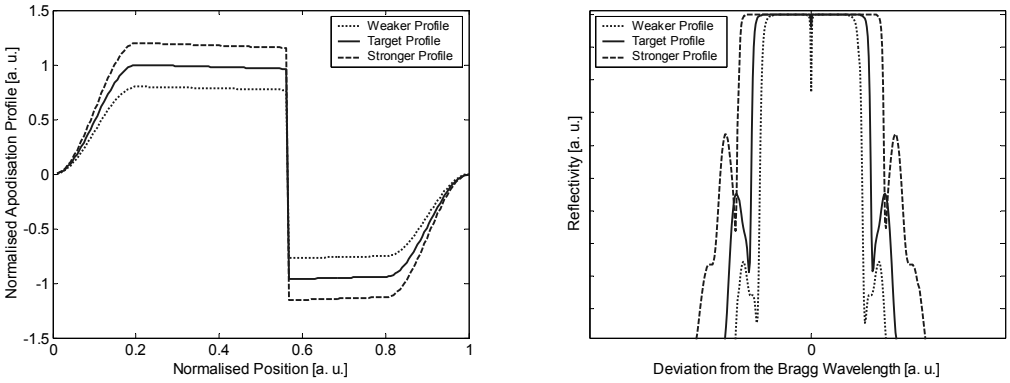

(a) (b)

Figure 4-9 (a) Normalised apodisation profile (solid line) and scaled profiles. Change of sign in the profile corresponds to the discreet π phase-shift (b) Normalised reflection spectrum of corresponding apodisation profiles.

Characterisation of the grating corresponds to the measurement of the absolute value of the apodisation profile which manifests itself in the reflection spectrum in a predictable manner: A larger coupling coefficient profile results in larger and wider side-lobes, and a weaker profile leads to smaller and narrower side-lobes in the spectrum of a π phase-shifted grating. Figure 4-9(b) compares the reflection spectra of the scaled apodisation profiles of Figure 4-9(a).

When characterising a DFB laser, since we know the normalised apodisation profile from the grating writing process, we can scale it up and down in our simulations until the results match the experimental reflection spectrum data, so that we can determine the absolute value of the profile. Although this idea is simple, in practice the birefringence of the fibre adds somewhat to the complexity of the measurement. Due to birefringence, fibre has slightly different effective refractive indices in two orthogonal polarisations. This difference results in two almost identical gratings in two polarisations with a slight offset, which in our case, is 10 – 20 pm. If the measurement setup does not distinguish between these two, then the resultant spectrum will be a superimposition of two spectra. Initially we were not able to separate the two polarisations in our experiments therefore we assumed a 15 pm offset in our simulations and compared the resultant spectrum to the experimental data. At a later stage, we were able to improve the experimental setup by introducing polarisation resolving units and we compared the spectra for individual polarisations.

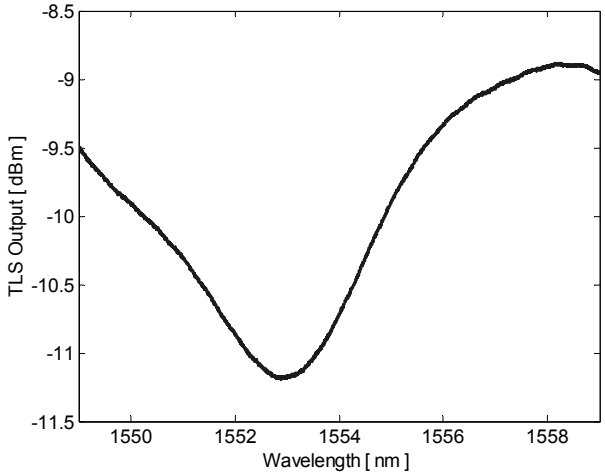

Figure 4-10 Power output spectrum of the tunable laser source used for grating characterisation. The variation in the power manifests itself as a slope in the reflection spectrum.

We used a tunable laser source (TLS) in order to measure the reflection spectra of DFB lasers. Figure 4-10 shows the TLS output spectrum across the tuning range. Since the power delivered to the grating is not constant, we also incorporated this variation in the incident power with wavelength when calculating the reflection in our simulations.

4.4. Characterisation of the Pump Source

The semiconductor pump laser we used is electrically pumped with drive current– power characteristics as shown in Figure 4-11. These values are the actual powers delivered to the DFB laser after the WDM component.

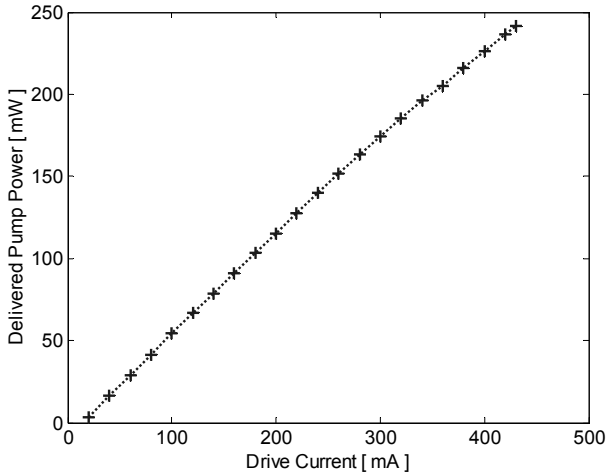

Figure 4-11 Drive current vs. pump power delivered to the DFB laser after the connectors and splices.

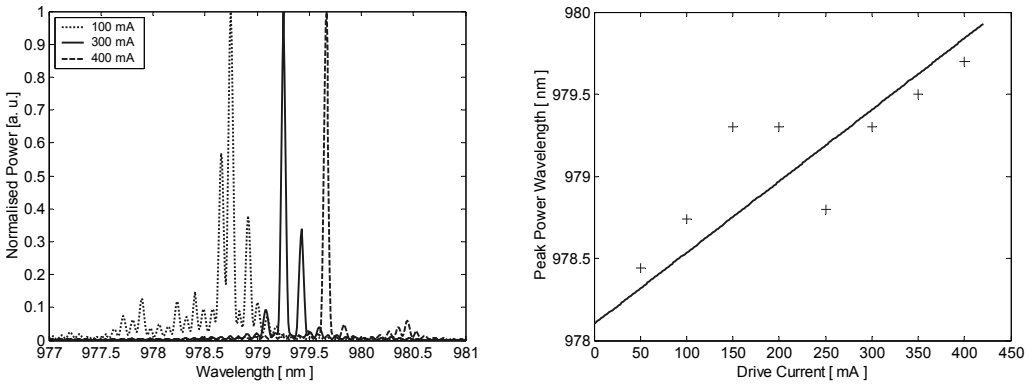

(a) (b)

Figure 4-12 (a) Output spectrum of the pump diode for different drive currents. (b) Experimental data (+) of the peak pump power wavelength and linear approximation (solid line) used in the simulations.

The wavelength of the pump source is also a defining factor in simulations since it affects the absorption by the active medium. It is especially critical if the pump operates between 970 – 980 nm where the Yb absorption cross-section dramatically changes with wavelength. As shown in Figure 4-12 (a), the output spectrum of the pump drifts to longer wavelengths with increasing drive current. Over the tuning range from 50 to 450 mA, the spectrum peak shifts from 978 nm up to 980 nm. We included this drift in our simulations as a linear variation in the wavelength as shown in Figure 4-12 (b).

4.5. Fitting Parameters

Experimental measurement of all the parameters that appear in the rate equations of the Er/Yb doped medium is beyond the scope of this study. Therefore parameters that cannot be derived from the available data are chosen such that they remain in the range reported by earlier studies. We varied the unknown parameters within the known range until satisfactory fitting is achieved in output powers as well as in residual pump powers for input powers from 0 to 240 mW.

Table 4-2 shows the fitted, experimentally measured and assumed parameters with the corresponding literature. The life-time of Yb ions can vary considerably depending on the host composition. For example in the glass hosts with various co-dopants including Al the life-time varies in the range 1.3 – 2.3 ms [29], even 0.7 ms is not an uncommon value. Although other literature quote values in the smaller end of this range for various various Er/Yb codoped fibres, they do not necessarily distinquish between the quenched and normal ions and present an effective observed life-time value. Here we distinguish between the normal (89%) and quenched ions (11%), and when we combine their life-times to obtain an effective value we found it to be 1.78 ms.

Parameter	*Value*	*Source*	*Related Literature*
Pump Wavelength	978 – 980 nm	Measured	
Yb Concentration	**34 x 10^{25} m^{-3}**	**Fitted**	
$\sigma^{Yb}_{p,a}$, $\sigma^{Yb}_{p,e}$	Figure 4-7	Measured	[27],[28], [29]
Yb $^2F_{5/2}$ life-time	**2 ms**	**Assumed**	**[29]**
Yb $^2F_{5/2}$ quenched life time	1 µs	Assumed	[8],[24]
Quenched Yb / Total Yb	**0.11**	**Measured**	
Signal Wavelength	1551-1554 nm	Measured	
Er Concentration	**3 x 10^{25} m^{-3}**	**Fitted**	
$\sigma^{Er}_{s,a}$, $\sigma^{Er}_{s,e}$	Figure 4-8 (b)	Measured	[30],[31],[32]
$\sigma^{Er}_{p,a}$	**3 x 10^{-25} m^2**	**Assumed**	**[33]**
Er $^2I_{13/2}$ life-time	10 ms	Assumed	[33],[34]
Er $^2I_{11/2}$ life-time	**0.6 µs**	**Fitted**	**[21],[35]**
Er $^4F_{7/2}$, $^2H_{11/2}$, $^2S_{3/2}$ Non-radiative / radiative transition rate	14 x 10^5 s^{-1} , 10^3 s^{-1}	Assumed	[21]
k_{tr}	**8 x 10^{-22} m^3s^{-1}**	**Fitted**	**[36],[37],[38],[39],[17]**
$C_{up,2}$, $C_{up,3}$	1 x 10^{-24} m^3s^{-1}	Assumed	[36],[38]
$C_{ESA,2}$, $C_{ESA,3}$	**1 x 10^{-27} m^2**	**Fitted**	**[40]**
Signal Background Loss	0.15 m^{-1}	Measured	
Core radius	**2.3 µm**	**Measured**	
n_1 , n_2	1.4709 , 1.4585	Measured	

Table 4-2 Active medium parameters and related literature.

4.6. Results

If the active medium parameters are accurate enough then the model should predict the absorption characteristics of the fibre without any grating present. Figure 4-13 (a) shows the simulation (solid curve) and experimental results (error bars) of the cut-back experiment at the pump wavelength. Figure 4-13 (b) compares the theoretical absorption saturation (solid line) with the experimental data (error bars) of the cut-back experiment. In the same plot, we also included the simulation results when a constant average pump wavelength (979 nm) is used (dotted curve) instead of taking into account the drift in the pump wavelength with increasing power shown in Figure 4-12(b). The deviation between two curves shows the significance of accurate modelling of the pump source, especially at the wavelengths where cross-sections change dramatically.

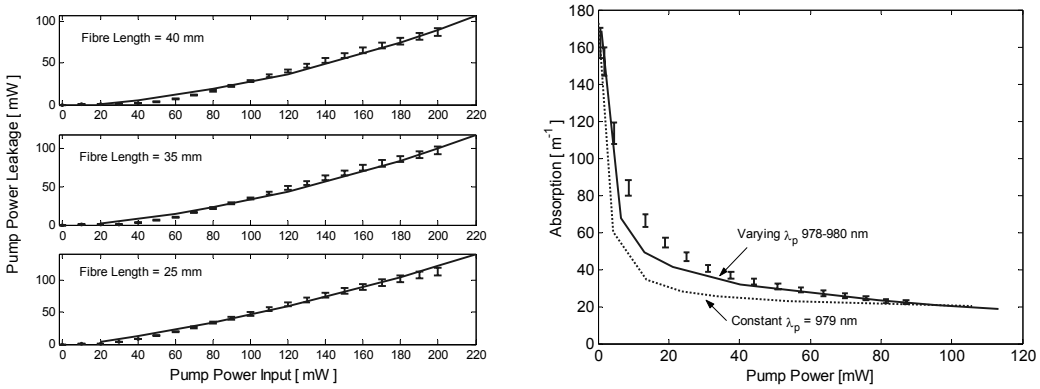

(a) (b)

Figure 4-13 (a) Comparison of experimental and simulation result of cutback experiment for 40, 35 and 25mm-long fibres. (b) Variation of average of absorption with pump power. Experimental data (error bars) are compared against the simulation results with varying (solid line) and constant pump wavelength (dotted)

Figure 4-14 (a) and (b) show two different normalised apodisation profiles used in DFB lasers on the absolute scale where the position of the phase shift is indicated with the dotted vertical lines. Figure 4-14 (a) is a standard DFB laser. The small apodisation towards the ends increases the side-mode suppression and improves the longitudinal mode stability. The asymmetrically located phase-shift provides unidirectional output power. The step apodised profile given in Figure 4-14 (b) is discussed in detail in the next chapter. It is designed to improve the efficiency and it still maintains the same uni-directionality and longitudinal mode stability.

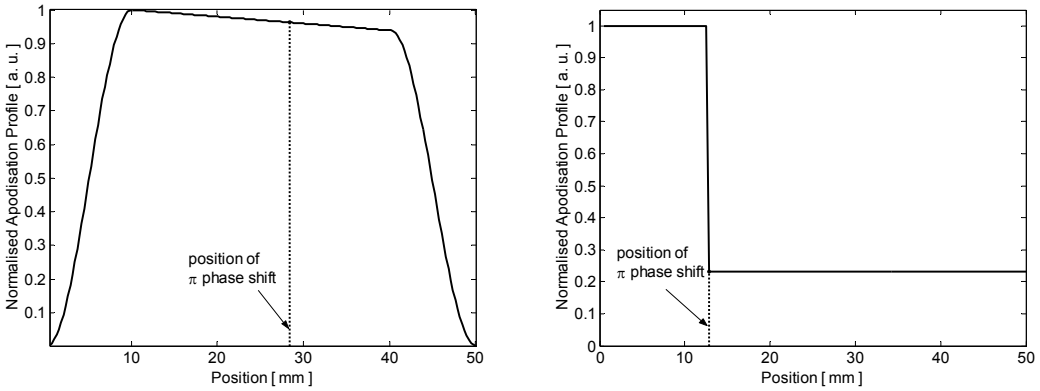

(a) (b)

Figure 4-14 Two normalised apodisation profiles used in DFB lasers(a) Smooth Apodised Profle (b) Step Apodised Profile

The normalised profiles are inherently known from the production method and we used the grating characterisation method to find the scaling factor, which is equivalent to the grating's maximum coupling coefficient κ. Figure 4-15 (a) and (b) show the matching simulation and experimental reflection spectra (Bragg wavelength = 1552 nm) for

apodisation profiles in Figure 4-14 (a) and (b) respectively. We found the scaling factor to be 210 m^{-1} and 350 m^{-1} in the respective cases.

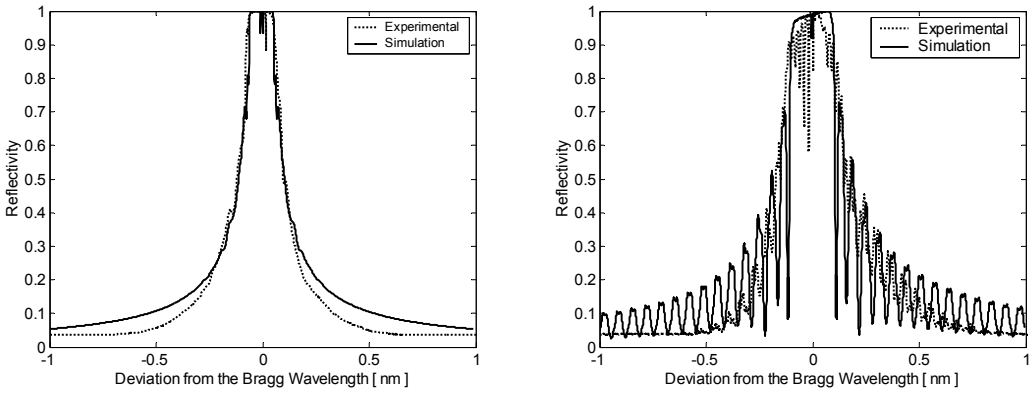

(a) (b)

Figure 4-15 Deduction of absolute scaling of the apodisation profiles by comparing the experimental (dotted line) and theoretical (solid line) reflection spectra. (a) Smooth apodised profile. Peak κ = 210 m^{-1} (b) Step apodised profile. Peak κ = 350 m^{-1}

Experimental and simulated results for reflection spectra are both composed of two slightly offset spectra due to birefringence and simulations take into account the wavelength dependent nature of the TLS output shown in Figure 4-10 . The difference between the experimental and simulated reflected powers is found to be less than -32 dBm (0.6 µW) for input powers around -11 dBm.

4.7. DFB Laser Simulations

After characterising the pump source, deducing the absolute apodisation profile of the gratings and confirming the active medium model predictions at both high and low pump powers, we are now ready to simulate DFB lasers and compare with the experimental results.

While simulating the lasers we ignore the gain grating due to the spatial-hole-burning since the gain and its modulation are very small compared to the refractive index grating. In addition to the gain grating, the periodic modulation of the gain can result in a slightly different saturated value than the one we calculate in a simplistic fashion using the average value of the standing wave pattern [41]. However, given the small value of the unsaturated gain and the large energy migration among the ions of highly doped fibre, the uncertainity due to this effect is not as significant as the uncertainities in the spectroscopic properties of the fibre.

Figure 4-16 shows the experimental setup used to characterise the DFB lasers. DFB lasers are pumped by the semiconductor laser in a co-directional manner: that is the pump power propagates in the same direction as the desired output end of the DFB laser. In this forward direction, a 980 /1550 nm WDM is used to separate the DFB output signal from the residual pump power. Residual pump power is measured by a power meter (PM).

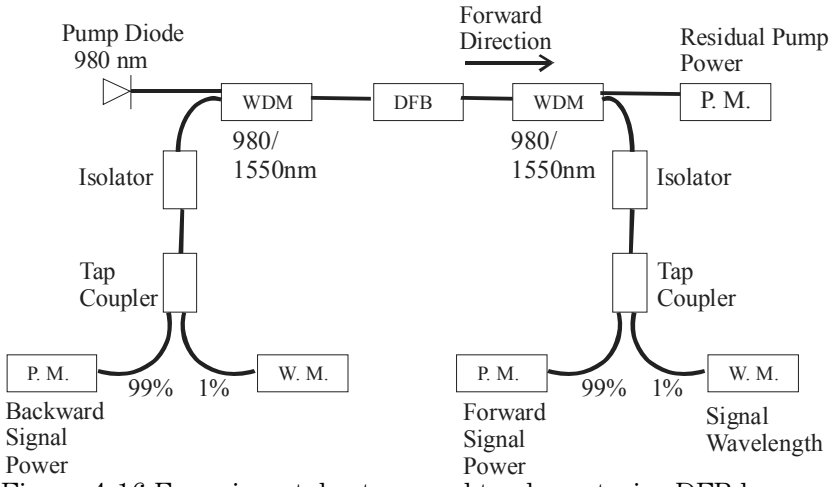

Figure 4-16 Experimental setup used to characterise DFB lasers.

A tap coupler is used to feed 1% of the signal to a wave-meter (WM) in order to measure the peak wavelength. The other arm of the coupler is connected to a power-meter to measure the output power in the forward direction. A similar setup is used on the other side of the DFB laser in order to measure the backward output power as well as the peak wavelength. On both sides, optical isolators prevent spurious back-reflections from entering and perturbing the DFB laser. The transmission of all components is measured, so that the output powers could be calculated from power-meter readings.

The theoretical and experimental output power at 1552 nm and the residual pump power around 979 nm from the two DFB designs given in Figure 4-14 (a) and (b) are shown in Figure 4-17 (a) and (b) respectively. The results for both designs show very good agreement over the full range of the pump powers.

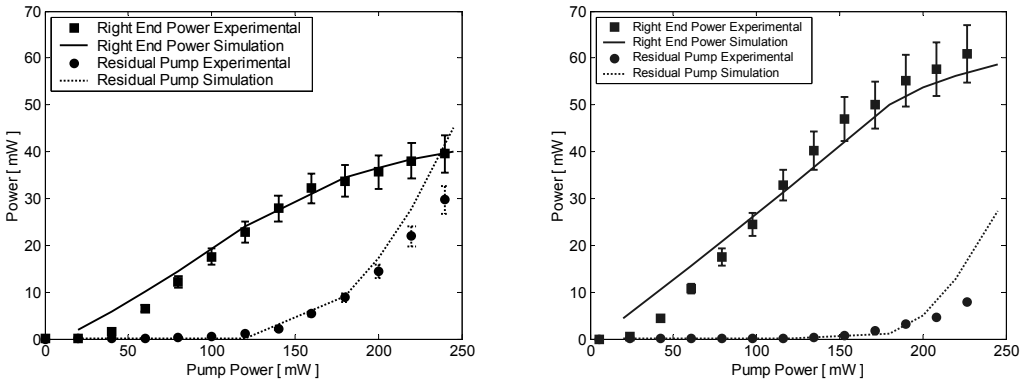

Figure 4-17 Design-end signal and residual pump power from DFB lasers. Experimental (error bars) and theoretical data (solid and dotted lines) are compared. (a) Smooth apodised DFB laser (b) Step apodised DFB laser

We believe the deviation between the simulations and the experiments at low pump powers may be due to a number of factors: The wavelength of the pump source abruptly changes with the drive current, (see Figure 4-12(b)), which is included in the simulation only as a linear variation. Production of the devices requires splicing tolerances, which means there is a 4±1 mm long additional doped fibre before and after the grating. A 4 mm long section is included in the model, but any error will impact the simulation especially at the low pump powers. Finally, heating and temperature distributions are known to affect the gratings in Er/Yb co-doped fibres [41] . The phase-shift could be approaching the ideal π value at the larger pump powers as a result of heating whereas at low pump powers deviation from this value could lead to an increased threshold value and lower efficiency.

4.8. Conclusions

We have modelled Er/Yb co-doped π-phase shifted fibre DFB lasers as complete systems comprised of the pump source, the active medium, and the grating. We characterised each of them and, for the first time, we simulated two different DFB laser designs with experimental verification over a pump power range from 0 to 240 mW. Unlike previous theoretical works which gave information as trends in the power characteristics, our results agreed well with the actual experimental data for different DFB laser designs.

We presented a set of simple experiments for the characterisation of Er/Yb doped media and gratings that provide sufficient data for the modelling and simulation of short fibres and lasers. We measured a large amount of unsaturable loss at the pump wavelength that is attributed to Yb clustering and lifetime quenching. This effect has a significant impact on the performance and the efficiency of fibre DFB lasers. This proves to be the major

limiting factor in the design of highly efficient DFB lasers that will be discussed in Chapter 7.

The developed model can be utilised in many different ways: It can be used to compare laser designs with different apodisation profiles, lengths, and chirp rates, in terms of their efficiency at different pump wavelengths and pump powers. It can also be used to investigate the effects of the fibre geometry such as core radius, or NA, the active medium properties, such as quenching or ion concentration on the device performance at different signal wavelengths. This model will be the basis of all the following Er/Yb co-doped device simulations and optimisations.

4.9. References:

[1] J. Hubner, P. Varming, and M. Kristensen, "Five wavelength DFB fibre laser source for WDM systems," *Electronics Letters*, vol. 33, no. 2, pp. 139-140, 1997.

[2] M. Ibsen, S. U. Alam, M. N. Zervas, A. B. Grudinin, and D. N. Payne, "8-and 16-channel all-fiber DFB laser WDM transmitters with integrated pump redundancy," *IEEE Photonics Technology Letters*, vol. 11, no. 9, pp. 1114-1116, 1999.

[3] H. N. Poulsen, P. Varming, A. Buxens, A. T. Clausen, P. Munoz, P. Jeppesen, C. V. Poulsen, J. E. Pedersen, and L. Eskildsen, "1607 nm DFB fibre laser for optical communcation in the L-band," presented at ECOC, Nice, France, 1999, Mo B2.1

[4] J. T. Kringlebotn, W. H. Loh, and R. I. Laming, "Polarimetric Er3+-doped fiber distributed-feedback laser sensor for differential pressure and force measurements," *Optics Letters*, vol. 21, no. 22, pp. 1869-1871, 1996.

[5] E. Ronnekleiv, M. Ibsen, and G. J. Cowle, "Polarization characteristics of fiber DFB lasers related to sensing applications," *IEEE Journal of Quantum Electronics*, vol. 36, no. 6, pp. 656-664, 2000.

[6] O. Hadeler, M. Ibsen, and M. N. Zervas, "Distributied-feedback fiber laser sensor for simultaneous strain and temperature mesurements operating in the radio-frequency domain," *Applied Optics*, vol. 40, no. 19, pp. 3169-3175, 2001.

[7] C. Strohhofer and A. Polman, "Relationship between gain and Yb3+ concentration in Er3+ - Yb3+ doped waveguide amplifiers," *Journal of Applied Physics*, vol. 90, no. 9, pp. 4314-4320, 2001.

[8] R. Paschotta, J. Nilsson, P. R. Barber, J. E. Caplen, A. C. Tropper, and D. C. Hanna, "Lifetime quenching in Yb-doped fibres," *Optics Communications*, vol. 136375-378, 1997.

[9] G. Sorbello, S. Taccheo, and P. Laporta, "Numerical modelling and experimental investigation of double-cladding erbium-ytterbium-doped fibre amplifiers," *Optical and Quantum Electronics*, vol. 33599-619, 2001.

[10] E. Yahel and A. Hardy, "Modeling High-Power Er3+ - Yb3+ Codoped Fiber Lasers," *Journal of Lightwave Technology*, vol. 21, no. 9, pp. 2044-2052, 2003.

[11] E. Yahel and A. Hardy, "Modeling and Optimization of Short Er3+-Yb3+ Codoped Fiber Lasers," *IEEE Journal of Quantum Electronics*, vol. 39, no. 11, pp. 1444-1451, 2003.

[12] S. B. Poole, J. E. Townsend, D. N. Payne, M. E. Fermann, G. J. Cowle, R. I. Laming, and P. R. Morkel, "Characterization of Special Fibers and Fiber Devices," *Journal of Lightwave Technology*, vol. 7, no. 8, pp. 1242-1255, 1989.

[13] G. G. Vienne, J. E. Caplen, L. Dong, J. D. Minelly, J. Nilsson, and D. N. Payne, "Fabrication and Characterization of Yb3+:Er3+ Phosphosilicate Fibers for Laser," *Journal of Lightwave Technology*, vol. 16, no. 11, pp. 1990-2001, 1998.

[14] M. Karasek, "Optimum Design of Er3+-Yb3+ Codoped Fibers for Large-Signal High-Pump-Power Applications," *IEEE Journal of Quantum Electronics*, vol. 33, no. 10, pp. 1699-1705, 1997.

[15] G. C. Valley, "Modeling Cladding-Pumped Er/Yb Fiber Amplifiers," *Optical Fiber Technology*, vol. 721-44, 2001.

[16] F. Di Pasquale, "Modeling of Highly-Efficient Grating-Feedback and Fabry-Perot Er3+ Yb3+ Co-Doped Fiber Lasers," *IEEE Journal of Quantum Electronics*, vol. 32, no. 2, pp. 326-332, 1996.

[17] J. Nilsson, P. Scheer, and B. Jaskorzynska, "Modeling and Optimization of Short Yb3+ Sensitized Er3+ Doped Fiber Amplifiers," *IEEE Photonics Technology Letters*, vol. 6, no. 3, pp. 383-385, 1994.

[18] M. Achtenhagen, R. J. Beeson, F. Pan, B. Nyman, and A. Hardy, "Gain and Noise in ytterbium-Sensitized erbium-Doped Fiber Amplifiers: Measurements and Simulations," *Journal of Lightwave Technology*, vol. 19, no. 10, pp. 1521-1526, 2001.

[19] J. Kemtchou, M. Duhamel, and P. Lecoy, "Gain temperature dependence of erbium-doped silica and fluoride fiber amplifiers in multichannel wavelength-multiplexed transmission systems," *Journal of Lightwave Technology*, vol. 15, no. 11, pp. 2083-2090, 1997.

[20] Y. Maeda and T. Yamada, "Temperature dependence of the enhanced excited state absorption in erbium-doped garnets," *Journal of Applied Physics*, vol. 83, no. 12, pp. 7436-7441, 1998.

[21] E. Desurvire, C. R. Giles, and J. R. Simpson, "Gain Saturation Effects in High-Speed, Multichannel erbium-Doped Fiber Amplifiers at Lambda = 1.53 um," *Journal of Lightwave Technology*, vol. 7, no. 12, pp. 2095-2104, 1989.

[22] L. Dong, W. H. Loh, J. E. Caplen, J. D. Minelly, K. Hsu, and L. Reekie, "Efficient single-frequency fiber lasers with novel photosensitive Er/Yb optical fibers," *Optics Letters*, vol. 22, no. 10, pp. 694-696, 1997.

[23] A. Asseh, H. Storoy, B. E. Sahlgren, S. Sandgren, and R. A. H. Stubbe, "A writing technique for long fiber Bragg gratings with complex reflectivity profiles," *Journal of Lightwave Technology*, vol. 15, no. 8, pp. 1419-1423, 1997.

[24] Z. Burshtein, Y. Kalisky, S. Z. Levy, P. Le Boulanger, and S. Rotman, "Impurity Local Phonon Nonradiative Quenching of Yb3+ Fluorescence in ytterbium-Doped Silicate Glasses," *IEEE Journal of Quantum Electronics*, vol. 36, no. 8, pp. 1000-1007, 2000.

[25] P. Yang, P. Deng, and Z. Yin, "Concentration quenching in Yb:YAG," *Journal of Luminescence*, no. 97, pp. 51-52, 2002.

[26] E. Desurvire, "Section 4.5 Determination of Transition Cross Sections," in *erbium-Doped Fiber Amplifiers: Principles and Applications*. New York: John Wiley & Sons, Inc, 1994, pp. 245-270.

[27] H. M. Pask, R. J. Carman, D. C. Hanna, A. C. Tropper, C. J. Mackechnie, P. R. Barber, and J. M. Dawes, "ytterbium-Doped Silica Fiber Lasers: Versatile Sources for the 1-1.2 um Region," *IEEE Journal of Selected Topics in Quantum Electronics*, vol. 1, no. 1, pp. 2-13, 1995.

[28] X. Zou and H. Toratani, "Evaluation of spectroscopic properties of Yb3+-doped glasses," *Physical Review B*, vol. 52, no. 22, pp. 15889-15897, 1995.

[29] H. Yin, P. Deng, J. Zhang, and F. Gan, "Emission properties of Yb3+ in fluorophosphate glass," *Journal of Non-Crystalline Solids*, vol. 210, pp. 243-248, 1997.

[30] W. J. Miniscalco and R. S. Quimby, "General procedure for the analysis of Er3+ cross sections," *Optics Letters*, vol. 16, no. 4, pp. 258-260, 1991.

[31] W. J. Miniscalco, "erbium-Doped Glasses for Fiber Amplifiers at 1500 nm," *Journal of Lightwave Technology*, vol. 9, no. 2, pp. 234-250, 1991.

[32] L. W. Barnes, R. I. Laming, E. J. Tarbox, and P. R. Morkel, "Absorption and Emission Cross Section of Er3+ Doped Silica Fibers," *IEEE Journal of Quantum Electronics*, vol. 27, no. 4, pp. 1004-1010, 1991.

[33] E. Desurvire, J. L. Zyskind, and C. R. Giles, "Design Optimization for Efficient erbium-Doped Fiber Amplifiers," *Journal of Lightwave Technology*, vol. 8, no. 11, pp. 1730-1741, 1990.

[34] B. J. Ainslie, "A Review of the Fabrication and Properties of erbium-Doped Fibers for Optical Amplifiers," *Journal of Lightwave Technology*, vol. 9, no. 2, pp. 220-227, 1991.

[35] E. Maurice, G. Monnom, B. Dussardier, and D. B. Ostrowsky, "Clustering effects on double energy transfer in heavily ytterbium-erbium-codoped silica fibers," *Journal of Optical Society of America B*, vol. 13, no. 4, pp. 693-701, 1996.

[36] B. Hwang, S. Jiang, T. Luo, J. Watson, G. Sorbello, and N. Peyghambarian, "Cooperative upconversion and energy transfer of new high Er3+- and Yb3+ - Er3+-doped phosphate glasses," *Journal of Optical Society of America B*, vol. 17, no. 5, pp. 833-838, 2000.

[37] C. Lester, A. Bjarklev, T. Rasmussen, and P. G. Dinesen, "Modeling of Yb3+ Sensitized Er3+ Doped Silica Waveguide Amplifiers," *Journal of Lightwave Technology*, vol. 13, no. 5, pp. 740-743, 1995.

[38] S. Taccheo, G. Sorbello, S. Longhi, and P. Laporta, "Measurement of the energy transfer and upconversion constants in Er-Yb-doped phosphate glass," *Optical and Quantum Electronics*, vol. 31249-262, 1999.

[39] M. Federighi and F. Di Pasquale, "The Effect of Pair-Induced Energy Transfer on the Performance of Silica Waveguide Amplifiers with High Er3+ / Yb3+ Concentrations," *IEEE Photonics Technology Letters*, vol. 7, no. 3, pp. 303-305, 1995.

[40] J. Nilsson, P. Blixt, B. Jaskorzynska, and J. Babonas, "Evaluation of Parasitic Upconversion Mechanisms in Er3+-doped Silica-Glass Fibers by Analysis of Fluorescence at 980 nm," *Journal of Lightwave Technology*, vol. 13, no. 3, pp. 341-349, 1995.

[41] B. Jaskorzynska, E. Vanin and S. Helmfrid, "Gain-Saturaion Gratings with an Arbitrary Diffusion Rate of Excited States", *Journal of Optical Society of America B*, vol. 15, no 3, pp 945-950, 1998. 1995.

[42] Y. Z. Xu, H. Y. Tam, S. Y. Liu, and M. S. Demokan, "Pump-induced thermal effects in Er-Yb fiber grating DBR lasers," *IEEE Photonics Technology Letters*, vol. 10, no. 9, pp. 1253-1255, 1998.

Chapter 5 Investigation of the Classic Optimisation Method for DFB Lasers

5.1. Introduction

To date, efforts in improving DFB fibre laser efficiency have been based on *parametric* analysis. That is, certain parameters of the cavity such as grating length, grating strength and position of the phase shift were varied over a range to find an optimum combination [1-4]. In this Chapter, we critically investigate this classic optimisation approach and show that it is equivalent to optimisation of reflectivities in Fabry-Perot type lasers. We introduce the concept of effective cavity length and we present a new design that implements a simple apodisation profile to enhance the position and length of the effective cavity without impacting the cavity asymmetry, cavity Q-factor or the overall physical length. With the increased effective cavity length and increased pump power delivered around the phase-shift area the optical efficiency increases. We explain how the effective cavity, in which the optical signal predominantly circulates, can be increased while maintaining the optimum reflectivities, so that a longer section of the active medium contributes to the signal generation.

We discuss in detail a DFB fibre laser based on an erbium and ytterbium co-doped fibre. This combination of material is a well-known laser host, designed for high pump absorption around 975-980 nm and laser emission in the region 1528-1560nm (telecommunication C-band). The design principles can be equally applied to other dopants and host materials as well as to semiconductor and planar DFB lasers.

5.2. Uniform Design

Figure 5-1 illustrates a generic asymmetric DFB laser with a uniform apodisation profile and the signal distribution inside the cavity. In this asymmetric design, the maximum output power from the desired end is obtained for a particular phase-shift position, z_π, and coupling coefficient value, κ. These optimum values, $z_{\pi,opt}$ and κ_{opt} are found by varying the parameters over a defined range, either by simulation or by experiment [3, 5].

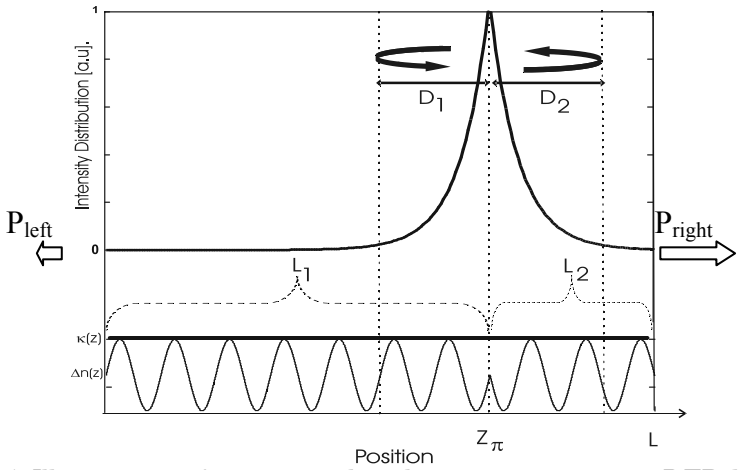

Figure 5-1 Illustration of intensity distribution in a generic DFB laser with uniform $\kappa(z)$ and corresponding refractive index modulation $\Delta n(z)$. Phase of the grating is shifted by π at z_π. Seen from this position there are two gratings in both direction of length L_1 and L_2. Fields propagating to the left and right, effectively, travel distances of D_1 and D_2 respectively.

In such a cavity, as illustrated in the figure, a very large intensity builds up around the phase-shift. We can think that the fields propagating to the left and to the right are trapped around the phase shift by the two grating segments and they are circulating within a short effective cavity. The peak signal intensity depends on the Q-factor of the effective cavity created by these two grating segments.

Each grating segment on either side of the phase-shift can be considered as a separate reflector. The reflection coefficient, r, of a grating with constant gain at the Bragg wavelength is given by [6]:

$$r = \frac{-\kappa \sinh(\gamma L)}{\gamma \cosh(\gamma L) - \alpha \sinh(\gamma L)} \tag{5.1}$$

where α is the field gain, κ is the coupling coefficient, L is the length of the grating and $\gamma = \sqrt{\kappa^2 + \alpha^2}$. However, if α is small compared to κ, which is the case for most practical applications, then (5.1) can be simplified to:

$$r \approx -\tanh(\kappa L) \qquad ;\alpha << \kappa \tag{5.2}$$

In our study, the maximum value of gain is around 3 m^{-1} and the typical coupling coefficient is 150 m^{-1}, so the approximation (5.2) holds. In this case the reflectivity, R, of the grating is:

$$R = |r|^2 \approx \tanh^2(\kappa L) \tag{5.3}$$

which is equal to the reflectivity of a passive grating with no gain.

Due to the distributed nature of the reflection process in gratings, the incident wave penetrates into the grating before re-emerging at the front end. This effective distance is known as the penetration depth, D [7], which in the case of constant gain and at the Bragg wavelength is given by [8]:

$$D = \frac{1}{2}\frac{\alpha L\left(\dfrac{\tanh(\gamma L)}{\gamma L} - \dfrac{1}{\cosh^2(\gamma L)}\right) + \tanh^2(\gamma L)}{\alpha \tanh^2(\gamma L) + \gamma \tanh(\gamma L)} \tag{5.4}$$

However if $\alpha << \kappa$ then D can be approximated by its passive cavity value:

$$D \approx \frac{\tanh(\kappa L)}{2\kappa} = \frac{|r|}{2\kappa} \tag{5.5}$$

In the case of a π-phase-shifted DFB laser, the total length of the effective cavity, L_{eff} in which the fields are circulating is:

$$L_{eff} = D_1 + D_2 \approx \left(\frac{|r_1|}{2\kappa_1} + \frac{|r_2|}{2\kappa_2}\right) \tag{5.6}$$

where D_1 and D_2 are the penetration depths into the grating segments on the left-hand-side (LHS) and on the right-hand-side (RHS) of the phase-shift, respectively. In the case of a uniform refractive index profile $\kappa_1 = \kappa_2 = \kappa$.

With the above definitions of reflectivity and effective cavity length we can consider a closer look at the standard DFB output power optimisation method. In our theoretical investigation we use the transfer-matrix method for the simulation of DFB lasers [6]. We first apply the parametric approach for the optimisation of a 50 mm-long Er/Yb co-doped fibre DFB laser. We assume 200 mW of pump power at 978 nm is launched from LHS and we want to have maximum output power at 1552 nm coming out from the RHS end. For different coupling coefficients, κ, we vary the phase-shift position, z_π and compute the laser output power characteristics. Figure 5-2 (a) shows the variation of the RHS output power, P_{right}, with z_π for three different κ values. It is first shown that for each κ there is a different optimum phase-shift position that results in maximum output power from the desired end. The output power from the opposite end is about two orders of magnitude

smaller resulting in almost perfect uni-directionality[5]. It is also evident that there is an optimum coupling constant, κ, that results in an overall maximum output power.

We should point out that, for each coupling constant, output power optimisation in asymmetric DFB lasers is in essence similar to the Rigrod optimisation of standard Fabry-Perot cavities [9, 10]. For each coupling constant, by moving the phase-shift we change the length of LHS grating, L_1, and RHS grating, L_2, which leads to a change in effective reflectivities R_1 and R_2, according to Equation (5.3), as shown in Figure 5-2(b). Therefore we can re-arrange the data of Figure 5-2(a) to show explicitly the variation of P_{rigth} with the reflectivity of the RHS grating, R_2 as in Figure 5-2(c). Here decreasing R_2 on the x-axis corresponds to increasing z_π. Figure 5-2(d) shows the variation in the round-trip reflectivity, R_1 x R_2, provided by the two gratings together, starting from the symmetrical cavity. The largest round-trip reflectivity, which is achieved when the phase shift is in the middle, for the weakest grating (κ = 120 m^{-1}) is 0.98, indicating a rather weak cavity confinement. For the stronger gratings, however, this value can be very close to unity, showing a much stronger confinement. Figure 5-2(e) shows the variation of the corresponding effective cavity lengths as a function of R_2. It is shown that increasing the grating coupling constant results in a decrease of the effective cavity length. On the other hand the effective cavity remains largely unaffected by the change of phase-shift position. The results of Figure 5-2(c) and (e) make the equivalence to the Rigrod analysis quite obvious. Varying the DFB phase-shift position affects primarily R_2 and results in output power optimisation, while the effective cavity remains practically constant. The existence of an optimum coupling constant (in this case κ = 150 m^{-1}) can be understood by considering Figure 5-2(d) and (e). Although smaller coupling constants (e.g. κ = 120 m^{-1}) result in a longer effective cavity, (c.f. Figure 5-2(e)), they show weaker cavity confinement (c.f. Figure 5-2(d)). For coupling constants higher than the optimum (e.g. κ = 180 m^{-1}), the stronger cavity confinement is compromised by the decrease of the effective cavity length. This dependence is accentuated by the presence of the fibre background loss.

Now let us consider the case where z_π and κ have the optimum values. The largest output power is obtained when z_π ≈29 mm (58% of total length) and κ ≈ 150 m^{-1} . The corresponding optimum reflectivities are $R_{1,opt}$ = 0.9993 and $R_{2,opt}$ = 0.9927. These values are in good agreement with the literature on experimental and theoretical work using similar fibres and setups [3, 5] .

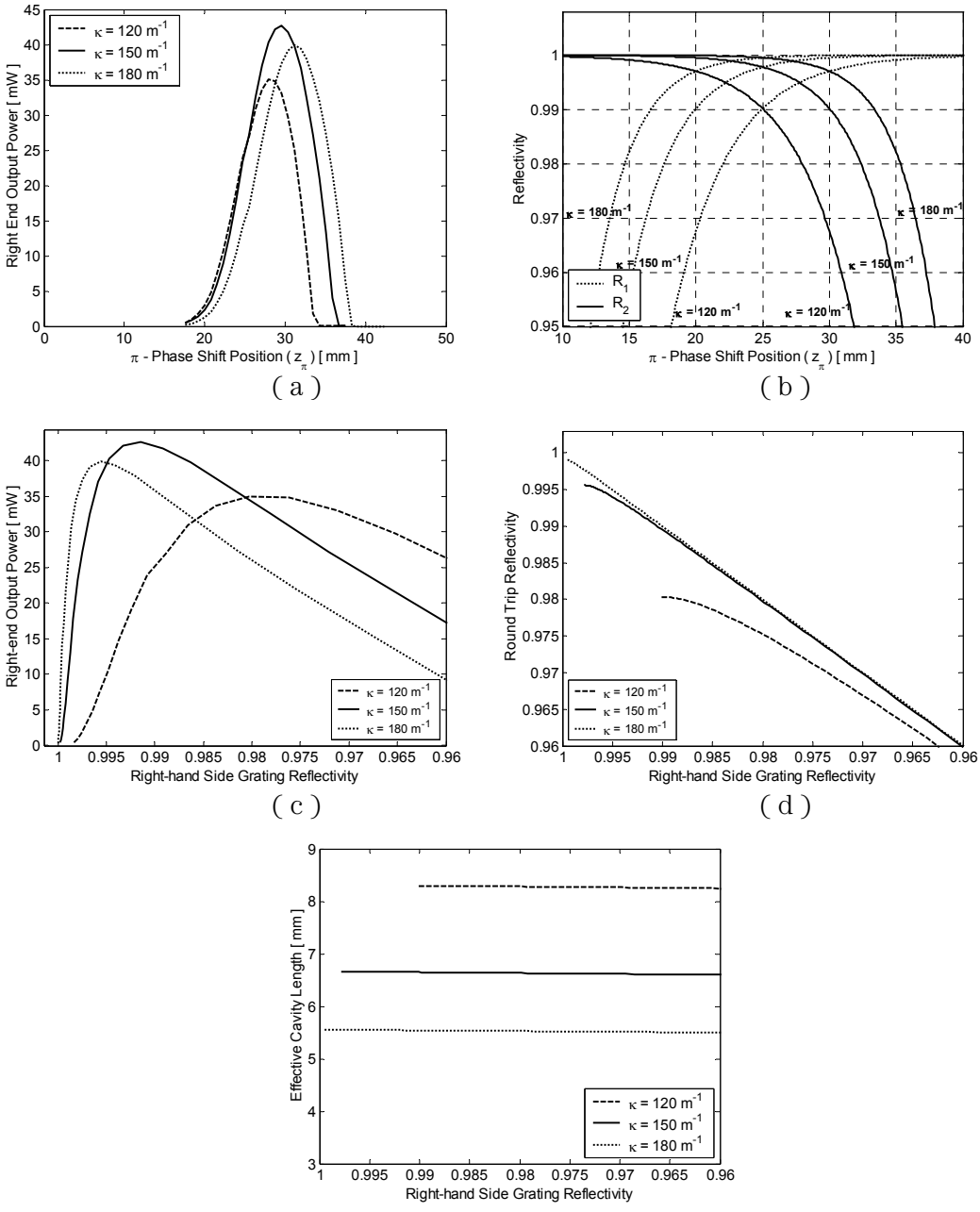

Figure 5-2 (a) Variation of right-end output power (P_{right}) with position of phase shift, z_π in uniform DFB lasers (b) Variation of reflectivities of gratings on the left (R_1) and right of the phase shift (R_2) (c) P_{right} variation as a function R_2 (d) Round trip reflectivity R_1 x R_2 as a function of R_2 (e) Comparison of effective cavity length for different κ as a function of R_2.

Figure 5-3 shows the average signal distribution (dashed line) at steady-state inside the optimised design as well as the corresponding gain distribution (solid line). The main feature of the distribution is the building up of intensity to very large values around the phase-shift. In this region, the active medium ions in the excited state undergo stimulated emission at a much higher rate due to the large signal intensity, causing the gain to drop substantially. In comparison, in the regions away from the phase-shift area,

where the signal intensity, and therefore, the stimulated emission is low, ions remain at the excited state and the gain remains close to the unsaturated value.

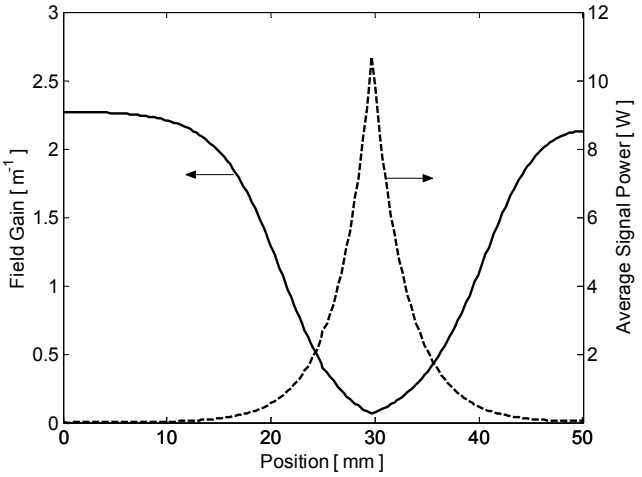

Figure 5-3 Field gain and signal power distributions inside a 50mm-long Er/Yb doped fibre at optimum (κ , z_π) pair. The intensity build up around phase shift position z_π = 29 mm causes gain to drop, indicating power extraction from the medium, but this build up quickly drops away from the phase-shift leaving a large amount of gain outside the phase shift area.

The L_{eff} in this optimum case is around 6.6 mm whereas the total device length is 50 mm. Thus only a fraction of the available active medium interacts with the signal strongly. We propose that by increasing the effective cavity length, we can utilize more of the active medium for signal generation, and therefore we can improve the laser output power without changing the total length of fibre or the pump power used.

5.3. Step-apodised Design

One way of increasing the penetration depth, as Equation (5.5) indicates, is to reduce the coupling coefficient. However by doing so, we also reduce the reflectivity of the grating and, therefore decrease the optical feedback, and deviate from the optimum confinement condition. Considering Equation (5.3) it is obvious that we can compensate the reduction in the reflectivity due to smaller κ by increasing the segment length L. When the length of one of the segments is increased, other segment's length must be decreased so that the total device length is not changed. With the same argument in order to compensate for the reduced length of the other segment, its coupling coefficient must be increased so that the optimum reflectivity is restored. Such a DFB cavity is characterised by a step change in the coupling coefficient on either side of the phase-shift. Figure 5-4 shows a schematic of such a step-apodised DFB cavity.

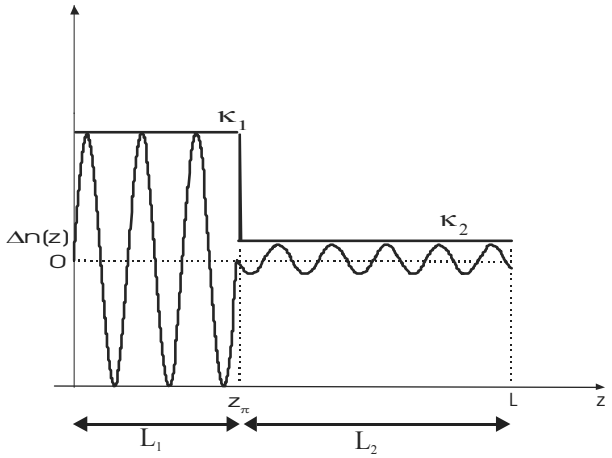

Figure 5-4 Illustration of the step apodised profile. As the phase shift is placed closer to the left-hand side the length of first segment gets shorter, and therefore a larger κ is required to keep the reflectivity the same. The length of the second segment however increases. Therefore the κ value in this segment is reduced.

We can summarize the conditions that must be met as:

$$\begin{aligned} \kappa_1 L_1 &= c_1 \\ \kappa_2 L_2 &= c_2 \\ L_1 + L_2 &= L \end{aligned} \tag{5.7}$$

where c_1 and c_2 are constants required to keep the reflectivities at the optimum values $R_{1,opt}$ and $R_{2,opt}$ respectively and L is the total device length, which is also kept constant. Using Equations (5.7) and setting $z_\pi = L_1$ we can rewrite Equation (5.6) as:

$$L_{eff}(z_\pi) = \left[\frac{|r_2|L}{2c_2} + \left(\frac{|r_1|}{2c_1} - \frac{|r_2|}{2c_2} \right) z_\pi \right] \tag{5.8}$$

which is a linearly decreasing function of the phase-shift position as Figure 5-5(a) shows(solid line). Compared with the effective cavity length variation in the optimum uniform-grating design (dotted line), the step-apodised profile increases L_{eff} significantly when the phase-shift is moved towards the LHS.

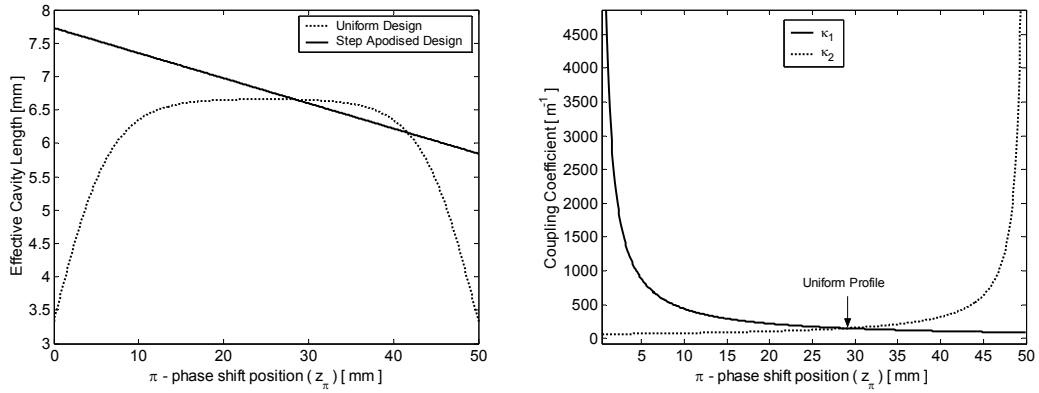

(a) (b)

Figure 5-5 (a) Variation of the effective cavity length, L_{eff}, with the phase-shift position. (b) Variation of the required coupling coefficients on both sides of the phase-shift in order to keep the corresponding reflectivities fixed to their optimum values.

Figure 5-5(b) shows the variation of the coupling coefficients of the grating segments on both sides of the phase-shift. As the segment length gets smaller a larger coupling coefficient is required to keep the reflectivity the same.

We again used the T-matrix method to simulate DFB lasers with a step apodisation for different z_π positions. The total output power, P_{Total}, and P_{Right}, show a linear variation with the position of the phase shift, similar to the variation of the effective cavity length. Figure 5-6 shows the variation of effective cavity length as well as P_{Total}, and P_{Right} of a step-apodised DFB laser as a function of the phase-shift position. By placing the phase-shift closer to the LHS, while preserving the optimum reflectivites, the total output power and RHS output power can be increased up to 50% with respect to the optimum uniform profile values (indicated by the arrows). As the phase-shift is placed closer to the LHS, κ_1 must be increased to keep R_1 at the optimum level (see Figure 5-5(b)). In practice, the photosensitivity of the fibre will determine the maximum coupling coefficient that can be attained, which in turn will determine how short the LHS segment can be. Coupling coefficients up to 500 m^{-1} are found to be feasible in the fibres we used. Larger values couldn't be induced accurately due to the saturation of photosensitivity and reduced repeatability in the production of gratings. This value allows us to put the phase shift around 12.5 mm away from the LHS end. Figure 5-6 indicates that for maximum P_{right} the phase-shift should be placed at $z_\pi = 0$. This is equivalent to a cavity comprised of a simple uniform grating butt-coupled to an external mirror or spliced to another passive grating of optimum reflectivity. In such a case, however, the non-trivial issue of introducing and maintaining the π phase-shift should be addressed satisfactorily.

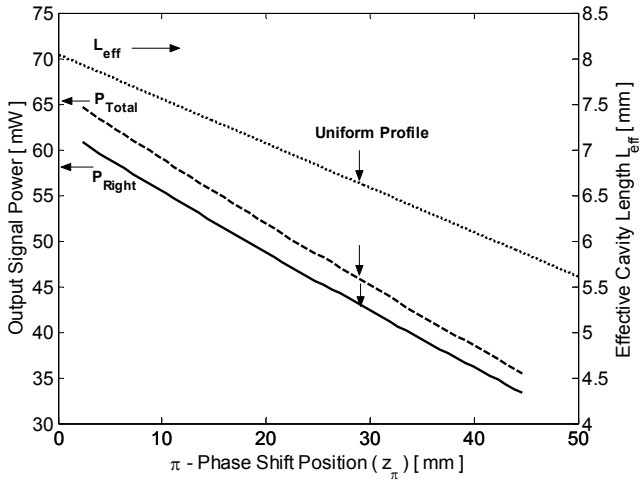

Figure 5-6 Right end output power, P_{Right}, and total output power (left and right), P_{Total}, variation with the position of phase shift in the step apodised profile.

Figure 5-7 shows the gain and average signal power distributions in a step-apodised cavity with z_π=12.5 mm. The effective cavity length in this case is 7.4 mm, corresponding to ≈12% increase with respect to the optimised uniform profile.

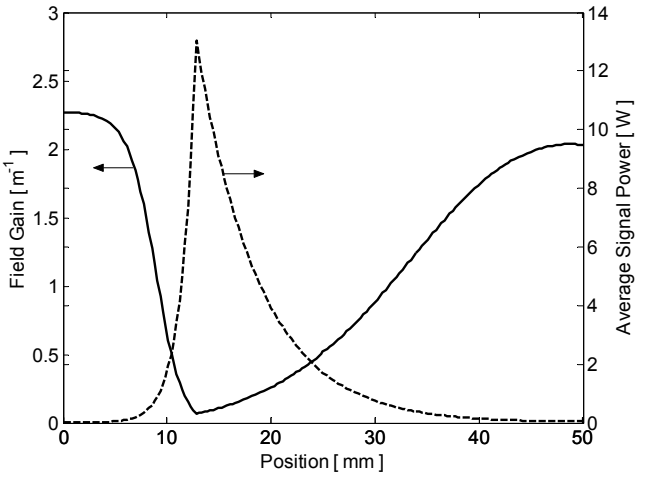

Figure 5-7 Field gain and signal power distributions inside a 50 mm-long Er/Yb doped fibre with a step apodisation profile. The phase shift is placed at z_π = 12.5 mm.

With the step apodisation profile the signal distribution is altered and spread out compared to the classic design.

The step-apodised profile not only increases the effective cavity length but also increases the pump power delivered into the effective cavity around z_π since in this case the phase-shift is placed closer to the pump source. As a result more pump power is available around the area where it is mostly needed, i.e. the area where the signal power increases considerably, and sustains the required gain (see Figure 5-7).

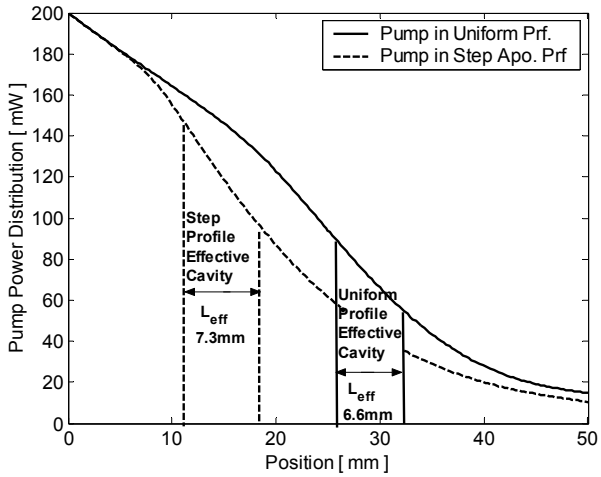

Figure 5-8 Pump power distributions in DFB lasers with uniform profile (solid line) and step apodised profile (dashed line). Effective cavities around the π-phase shift regions are indicated with vertical lines.

Figure 5-8 compares the pump power distributions in the optimised uniform and step-apodised profiles. The effective cavities of each profile are also indicated in the figure. In the step-apodised profile, the pump power delivered to the effective cavity is around 140 mW. In the uniform profile this value drops to 90 mW due to absorption by the longer segment between the pump source and the phase-shift region. With the combined effect of longer effective cavity and larger pump power, the pump-to-signal conversion increases from 22% to 27%.

5.4. Experimental Results

We applied the step-apodised design approach experimentally in the Er/Yb co-doped fibre we modelled and characterised in Chapter 4. Using the uniform profile, first we experimentally determined the optimum coupling coefficient and phase-shift position for maximum P_{right} by producing a number of uniform DFB lasers with different strengths and different phase shift positions. We used the experimental setup presented in Section 4.7 for laser characterisations.

The optimum value of κ and z_π were experimentally found to be 153 m^{-1} and 29 mm respectively, for a 50 mm-long device. These experimental results are in very good agreement with the simulation results. Using these values we calculated the required step-apodised profile with the phase-shift placed at z_π = 12.5 mm, as discussed in the previous section, and we fabricated 50 mm-long DFB laser with the calculated step-apodised profile. Figure 5-9 compares the theoretical and experimental values of RHS output power of uniform and step-apodised DFB lasers when pump power is varied from 0 to 240 mW.

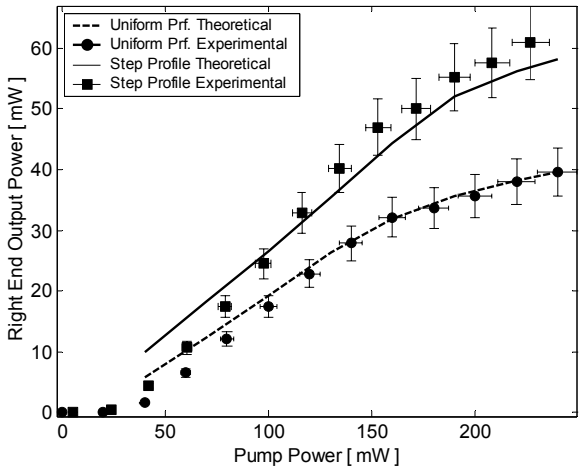

Figure 5-9 Experimental and theoretical comparison of DFB lasers with uniform and step apodised coupling coefficients. The phase-shift position in the step apodised laser is placed at 12.5 mm due to practical limits in the maximum refractive index change that can be induced.

We found that theoretical and experimental results were in very good agreement for both lasers. Experimentally, the introduction of the step-apodised profile increased the laser output power from 39 mW to 56 mW, corresponding to an increase in pump-to-signal conversion from 20% to 28%, which are very close to the values predicted by theory.

We believe that the deviation between the simulations and the experiments at low pump powers may be due to a series of factors: The wavelength of the pump source abruptly changes with the drive current, (see Fig. Figure 4-12 (b)), which is included in the simulation as only as a linear variation. Production of the devices requires splicing tolerances, which means there is a 4±1 mm long additional doped fibre before and after the grating. A 4 mm long section is included in the model, but any error will impact the simulation especially at the low pump powers. Finally, heating and temperature distributions are known to affect the gratings in Er/Yb co-doped fibres [11]. The phase-shift could be approaching the ideal π value at the larger pump powers as a result of heating whereas at low pump powers deviation from this value could lead to increased threshold values

Because the step-apodised profile increases the pump power delivered to the effective cavity compared to the initial optimum uniform design, the optimum values for the reflectivities can be slightly different. Therefore, additional optimisation is possible by fine-tuning the position of phase-shift around the step position. By doing so, we were able to increase the output power, experimentally, up to 60 mW for 200 mW pump power, increasing the pump-to-signal conversion to 30%.

5.5. Conclusions

Investigation of standard parametric optimisation of π phase-shifted DFB lasers has shown that the method is similar to the traditional Rigrod analysis of Fabry-Perot laser cavities. However, in the case of DFB lasers the efficiency is also influenced by the effective cavity length, which in turn is determined by the grating coupling coefficient. Based on the last observation, we have developed a new way of optimising DFB laser cavities: This method introduces a step-apodised profile that results in an increased effective cavity length without changing the reflectivities from their optimum values and without increasing the total grating length. The essential effect of the step apodised design is to alter the signal distribution inside the cavity to increase the efficiency. In addition to a longer effective cavity, this design increases the actual pump power delivered to the effective cavity since the phase-shift position is moved closer to the pump source.

We showed, both theoretically and experimentally, that in an Er/Yb doped fibre DFB laser this approach increased the pump-to-signal conversion from 20% to 28% as compared to an optimised uniform profile counter part. With further optimisation of reflectivities for the larger pump power delivered, we increased this figure up to 30%. The key to this increase in the efficiency is the increased interaction between the signal distribution and the active medium.

In implementing the step apodised design, the photosensitivity of the fibre sets the practical limit. This method is not limited only to the fibre DFB lasers and it can be equally well applied to DFB laser devices in other rare-earth doped fibres as well as in semiconductor and planar glass DFB lasers.

5.6. References:

[1] H. Soda, H. Ishikawa, and H. Imai, "Design of DFB-Lasers for High-Power Single-Mode Operation," *Electronics Letters*, vol. 22, no. 20, pp. 1047-1049, 1986.

[2] J. E. A. Whiteaway, G. H. B. Thompson, A. J. Collar, and C. J. Armistead, "The Design and Assessment of Lambda-4 Phase-Shifted DFB Laser Structures," *IEEE Journal of Quantum Electronics*, vol. 25, no. 6, pp. 1261-1279, 1989.

[3] V. C. Lauridsen, J. H. Povlsen, and P. Varming, "Design of DFB fibre lasers," *Electronics Letters*, vol. 34, no. 21, pp. 2028-2030, 1998.

[4] V. C. Lauridsen, J. H. Povlsen, and P. Varming, "Optimising erbium-doped DFB fibre laser length with respect to maximum output power," *Electronics Letters*, vol. 35, no. 4, pp. 300-302, 1999.

[5] M. Ibsen, E. Ronnekleiv, G. J. Cowle, M. O. Berendt, O. Hadeler, M. N. Zervas, and R. Laming, "Robust high power (>20mW) all-fibre DFB lasers with unidirectional and truly single polarisation outputs," presented at CLEO, Baltimore, USA, 1999.

[6] M. Yamada and K. Sakuda, "Analysis of Almost-periodic Distributed Feedback Slab Waveguides via a Fundamental Matrix Approach," *Applied Optics*, vol. 26, no. 16, pp. 3474-3478, 1987.

[7] D. I. Babic and W. Corzine, "Analytic Expressions for the Reflection Delay, Penetration Depth, and Absorptance of Quarter-Wave Dielectric Mirrors," *IEEE Journal of Quantum Electronics*, vol. 28, no. 2, pp. 514-524, 1992.

[8] F. Koyama, Y. Suematsu, S. Arai, and T. Tawee, "1.5-1.6 mu-m GaInAsP/InP Dynamic-Single-Mode (DSM) Lasers with Distributed Bragg Reflector," *IEEE Journal of Quantum Electronics*, vol. 19, no. 6, pp. 1042-1051, 1983.

[9] W. W. Rigrod, "Saturation Effects in High-Gain Lasers," *Journal of Applied Physics*, vol. 36, no. 8, pp. 2487-2490, 1965.

[10] C. T. Meneely, "Laser Mirror Transmissivity Optimization in High Power Optical Cavities," *Applied Optics*, vol. 6, no. 8, pp. 1434-1436, 1967.

[11] Y. Z. Xu, H. Y. Tam, S. Y. Liu, and M. S. Demokan, "Pump-induced thermal effects in Er-Yb fiber grating DBR lasers," *IEEE Photonics Technology Letters*, vol. 10, pp. 1253-1255, 1998.

Chapter 6 Cavity Design Method for Ultimate Laser Efficiency

6.1. Introduction

The classic parametric optimisation method does not guarantee the maximum efficiency possible since there are practically an infinite number of design possibilities with different combinations of apodisation profiles, phase-shift positions and device length. The parametric optimisation method can be improved by applying a proper evolutionary strategy such as genetic algorithms. However such techniques are known to be quite computation-intensive and time-inefficient. Unless the optimisation algorithm converges to the fundamental physical efficiency limit known *a priori* there is always room for further optimisation. As a matter of fact, as we have shown in the previous chapter, by increasing the effective cavity length and keeping the optimum reflectivity values constant, it is possible to improve DFB laser efficiency substantially above the parametric optimisation design. This improvement, however, is based on purely intuitive arguments and does not answer the question of how close the efficiency is to the fundamental limit.

In the previous chapter we pointed out the importance of the signal distribution and its interaction with the active medium. The step apodisation altered the signal distribution for better efficiency. In this chapter we introduce the concept of optimum intensity distribution for a given medium and present a novel analytical cavity design method for CW lasers that leads to this optimum intensity distribution, and consequently, provides the maximum possible conversion efficiency from pump to signal power.

The method is applicable to any medium in which a grating can be incorporated and it is limited only by the available grating writing and active-medium characterisation techniques. In addition to the design of maximum efficiency lasers, the design method can be applied to passive devices to achieve any signal distribution required, this will also be presented in this chapter.

6.2. Fundamental Design Equations

Similar approaches for grating design have been followed in the context of semiconductor DFB lasers to avoid the deleterious effects of spatial-hole-burning. G. Morthier and R. Baets [1] showed how to eliminate spatial hole burning in a DFB laser by attaining a uniform intensity distribution with proper grating designs. We have modified and extended their approach in order to derive more general equations that enable us to design complex grating structures that achieve any arbitrary internal intensity distribution.

In a one-dimensional grating, the total field, E, is the sum of the forward and backward propagating fields:

$$E(x,y,z) = R^{+}(z)\Psi^{+}(x,y)e^{-i\beta^{+}z} + R^{-}(z)\Psi^{-}(x,y)e^{i\beta^{-}z} \tag{6.1}$$

where $R^{+}(z)$ and $R^{-}(z)$ are the amplitude envelopes of the forward and backward propagating fields, $\Psi^{+}(x,y)$ and $\Psi^{-}(x,y)$ are the transverse modal distributions, respectively. β^{+} and β^{-} are the corresponding propagation constants of the fields.

Assuming slowly varying envelopes and small periodic perturbations in the waveguide or fibre parameters, the well-known coupled mode equations for counter-directional coupling can be written as (see for example [2]):

$$\frac{dR^{+}(z)}{dz} = \alpha(z)R^{+}(z) + \kappa(z)R^{-}(z)e^{i\Gamma(z)} \tag{6.2}$$

$$\frac{dR^{-}(z)}{dz} = -\alpha(z)R^{-}(z) + \kappa(z)R^{+}(z)e^{-i\Gamma(z)} \tag{6.3}$$

where $\alpha(z)$ is the field gain and $\kappa(z)$ is the coupling coefficient which depends on the particular characteristics of the periodic perturbation. Γ expresses the phase matching between the coupled modes and the grating in the form of:

$$\Gamma(z) = \beta^{+} + \beta^{-} - \phi(z) = \beta^{+} + \beta^{-} - \int_{0}^{z} \frac{2\pi}{\Lambda(z')}dz' \tag{6.4}$$

where $\phi(z) = \int_{0}^{z} \frac{2\pi}{\Lambda(z')}dz'$ is the phase of the sinusoidal grating and $\Lambda(z)$ is the spatial period of the perturbation. If the grating is not chirped then $\Lambda(z)$ is constant. If the

counter-propagating fields correspond to the same guided mode then $\beta^+ = \beta^- = \beta$ and Γ becomes:

$$\Gamma(z) = 2\beta - \int_0^z \frac{2\pi}{\Lambda(z')} dz' \tag{6.5}$$

In the case of a refractive index grating, $n(z)$, in a medium with n_0 effective refractive index and a sinusoidal modulation with an amplitude of Δn, that is;

$$n(z) = n_0 + \Delta n(z)\cos(\phi(z)) \tag{6.6}$$

the coupling coefficient κ is related to this modulation by:

$$\kappa(z) = \frac{\Delta n(z)\pi}{\lambda} \tag{6.7}$$

where λ is the wavelength of the propagating field.

Now we introduce two new parameters, namely; the signal intensity, S, and the intensity difference between the counter propagating fields, D, defined as follows:

$$S(z) = R^+(z)^2 + R^-(z)^2 \tag{6.8}$$

$$D(z) = R^+(z)^2 - R^-(z)^2 \tag{6.9}$$

In a linear cavity at steady state, the interference of two counter-propagating fields results in a standing wave pattern In this case the sum and difference given by Equations (6.8) and (6.9) are spatial averages of fast varying values modulated by $e^{i\beta z}$.

Multiplying Equation (6.2) with $R^+(z)$ and Equation (6.3) with $R^-(z)$ and taking the difference and using the above definitions of S and D we find:

$$\frac{1}{2}\frac{dD(z)}{dz} = \alpha(z)S(z) \tag{6.10}$$

Similarly multiplying Equation (6.2) with $R^+(z)$ and Equation (6.3) with $R^-(z)$ and summing them and again substituting S and D we find:

$$\frac{1}{2}\frac{dS(z)}{dz} = \alpha(z)D(z) + 2\kappa(z)R^+(z)R^-(z)\left[e^{i\Gamma(z)} + e^{-i\Gamma(z)}\right] \tag{6.11}$$

Now we solve Equations (6.10) and (6.11) for $D(z)$ and for the coupling coefficient $\kappa(z)$ namely;

$$D(z) = D(0) + 2\int_0^z \alpha(z)S(z)dz \tag{6.12}$$

$$\kappa(z) = \frac{1}{\sqrt{S(z)^2 - D(z)^2}}\left[\frac{1}{2}\frac{dS(z)}{dz} - D(z)\alpha(z)\right]\frac{1}{\cos\left[\Gamma(z)\right]} \tag{6.13}$$

where $D(0)$ is the initial value that is defined by considering the boundary conditions.

Equations (6.12) and (6.13) constitute the basis of our design method. Equation (6.12) depends on the boundary conditions and sets the device length while Equation (6.13) enables us to calculate the required apodisation profile $\kappa(z)$ for the given intensity $S(z)$ and certain chirp profile $\Lambda(z)$. The gain distribution $\alpha(z)$ can be defined as an independent parameter or it can be calculated as a function of $S(z)$ and pump power through the rate equations of the medium. In these equations $S(z)$ and $D(z)$ are intensity sums and differences. The intensities (W/m^2) are related to the actual power (W) simply by multiplication with the area and an overlap coefficient. Power values are more convenient than the intensities when realistic active media, such as rare-earth doped fibres, are investigated. Therefore, when dealing with a specific active medium we will refer to power and intensity values interchangeably.

At this stage it will be instructive to investigate the implications of Equation (6.12). Consider a small volume of medium, of length Δz, on which R^+_1 and R^-_2 are incident from opposite directions while R^+_2 and R^-_1 are leaving the volume again in opposite directions as illustrated in Figure 6-1.

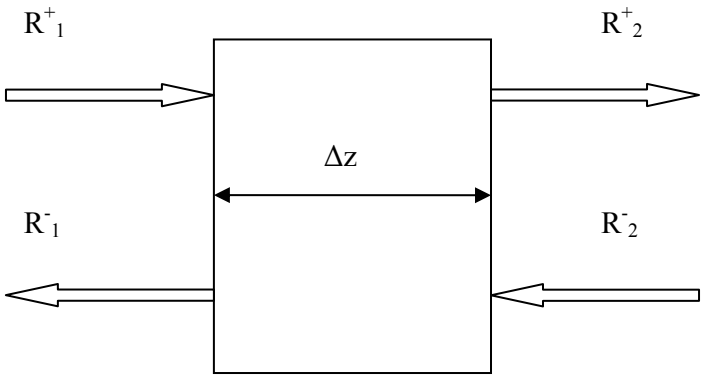

Figure 6-1 Incident fields and signal generating over a infinitesimal distance Δz

The total incident signal power on this volume is:

$$P_{incident} = \left(R^{+}_{1}\right)^2 + \left(R^{-}_{2}\right)^2 \tag{6.14}$$

and the total power leaving the volume is:

$$P_{leaving} = \left(R^{+}_{2}\right)^2 + \left(R^{-}_{1}\right)^2 \tag{6.15}$$

If there is a source or sink of signal inside the volume then the generated or absorbed power will be equal to the difference between the leaving and incident power. Using Equations (6.14) and (6.15) with a simple re-arrangement we find the generated (or absorbed) power, *G,* in this volume as:

$$G = P_{leaving} - P_{incident} = D_2 - D_1 = \Delta D \tag{6.16}$$

That is; the change in the $D(z)$ over a length corresponds to the total generated or absorbed power over this length. From Equation (6.12) we find this change over a length L as:

$$G = \Delta D = D(L) - D(0) = \int_0^L 2\alpha(z)S(z)dz \tag{6.17}$$

6.3. Design of Single Reflectors

Initially for the sake of simplicity let us apply Equations (6.12) and (6.13) to design simple reflectors for a chosen intensity distribution. Initially we will design reflectors for three intensity distributions, namely exponential, cosh(mz) and linear distributions, in a lossless medium. We will investigate the effect of loss or gain on the grating designs for

these distributions later. Figure 6-2 shows a generic passive device and its boundary conditions.

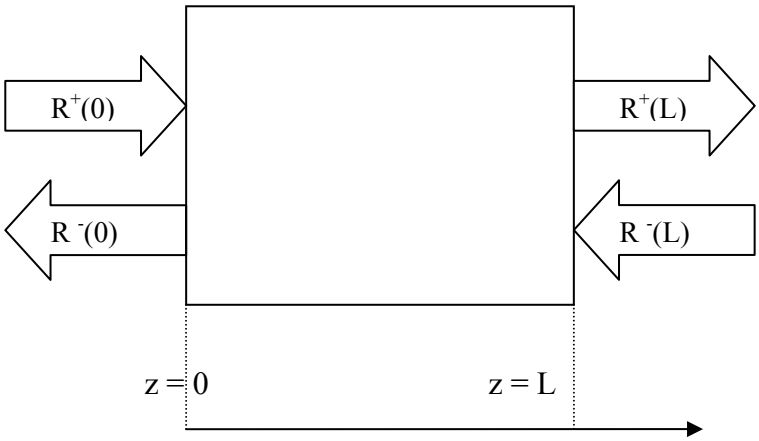

Figure 6-2 Schematic representation of a generic passive device

In this medium the gain (loss) is:

$$\alpha(z) = 0 \tag{6.18}$$

hence Equation (6.12) becomes:

$$D(z) = D(0) = D_0 \tag{6.19}$$

Now we will illustrate the design method for some simple intensity distributions:

6.3.1. Exponential Signal Distribution

A Special Case: Complete Reflection

Assume that we would like to design a perfect reflector such that the incident field $R^+(0)$ in Figure 6-2 is completely reflected back as $R^-(0)$ at the Bragg wavelength of the grating without any incident field at the RHS (i.e. $R^-(L)$=0) and we want the signal, $S(z)$, to decrease exponentially in the reflector as illustrated in Figure 6-3 (a).

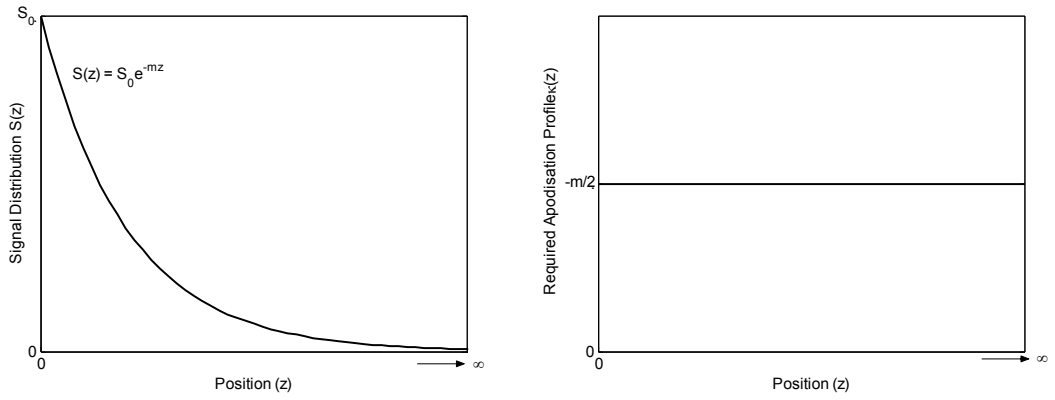

(a) (b)

Figure 6-3(a) Exponentially decreasing signal distribution (b) The required apodisation profile

If the reflection is complete then the first boundary condition at z = 0 is:

$$R^{+}(0) = R^{-}(0) \Rightarrow D(0) = 0 \tag{6.20}$$

and since there is no incident field at $z = L$:

$$R^{-}(L) = 0 \Rightarrow S(L) = R^{+}(L)^2 = D(L) \tag{6.21}$$

from Equation (6.19) and (6.20) we find the second boundary condition at $z = L$:

$$D(L) = 0 = S(L) \tag{6.22}$$

Now, if the signal distribution is exponential in the form:

$$S(z) = S_0 e^{-mz} \tag{6.23}$$

then

$$\frac{dS(z)}{dz} = -mS(z) \tag{6.24}$$

substituting $S(z)$, $dS(z)/dz$, $D(z)$, $\alpha(z)$ in Equation (6.13) and assuming constant grating period (no chirp) at the Bragg wavelength we find the required apodisation profile $\kappa(z)$ for the chosen signal distribution as:

$$\kappa(z) = \frac{1}{\sqrt{S(z)^2}}\left(\frac{-mS(z)}{2}\right) = \frac{-m}{2} \tag{6.25}$$

That is the required grating has a constant coupling coefficient and it is equal to half the exponential variation rate as in Figure 6-3(b). The length of the device is determined from the second boundary condition. The boundary condition at $z = L$ requires $D(L) = S(L) = 0$ and

$$S(L) = 0 \Rightarrow S_0 e^{-mL} = 0 \Rightarrow L \to \infty \tag{6.26}$$

That is; in order to reach complete reflection, i.e. $|r|^2 = 1$, the uniform grating needs to be infinitely long. Therefore; the exponential distribution approximation, which is frequently

used in practice, for uniform gratings is valid only if the losses are very small and the grating is infinitely long.

General Case

Now, let's consider a grating reflector in a lossless medium with a general reflectivity, $|r|^2 < 1$, again with exponential signal distribution $S(z) = S_0 e^{-mz}$ inside. If the reflection is not complete then there is a non-zero backward propagating signal which makes the first boundary condition: $D(0) = D_0 \neq 0$. With no loss or gain ($\alpha = 0$) Equation (6.12) gives:

$$D(z) = D(0) = D_0 \neq 0 \tag{6.27}$$

If the defined reflection coefficient is r and the incident signal intensity is $I_{incident}$ then the total signal intensity at the LHS boundary, S_0, is:

$$S_0 = I_{incident} + I_{reflected} = (1 + |r|^2) I_{incident} \tag{6.28}$$

similarly, the intensity difference at the LHS boundary D_0 is:

$$D_0 = I_{incident} - I_{reflected} = (1 - |r|^2) I_{incident} \tag{6.29}$$

and Equation (6.13) gives the general solution for the apodisation profile as:

$$\kappa(z) = -\frac{m}{2\sqrt{S(z)^2 - D_0^2}} S_0 e^{-mz} \tag{6.30}$$

6.3.2. cosh(mz) Signal Distribution

Equation (6.30) shows that the exponential signal distribution in general requires a z dependent apodisation profile. But we can employ the same expressions in reverse order to find the signal distribution corresponding to a desired apodisation profile. For example, we can define the coupling coefficient to be constant, i.e. $\kappa(z) = \kappa$ and set chirping to zero. In this case Equation (6.13) becomes:

$$\kappa = \frac{1}{2\sqrt{S(z)^2 - D_0^2}} \frac{dS(z)}{dz} \tag{6.31}$$

and the corresponding signal distribution $S(z)$ will be found by solving the first order differential equation:

$$\frac{dS(z)}{dz} = 2\kappa\sqrt{S(z)^2 - D_0{}^2} \tag{6.32}$$

where the initial value S_0 and the constant D_0 are again given by the defined reflectivity and the incident signal as in Equations (6.28) and (6.29). A simple variable substitution $y = S(z)/D_0$ transforms the Equation (6.32) into:

$$\frac{dy}{dz} = 2\kappa\sqrt{y^2 - 1} \tag{6.33}$$

and observing the hyperbolic trigonometric equalities:

$$\sqrt{\cosh^2(x) - 1} = \sinh(x) \quad \text{and} \quad \frac{d\cosh(x)}{dx} = \sinh(x) \tag{6.34}$$

we solve the differential equation for $y(z)$ as:

$$\frac{S(z)}{D_0} = y(z) = \cosh(2\kappa z) \tag{6.35}$$

Applying the initial value S(0) = S_0 and defining m=2κ to follow the convention we adopted we find the signal distribution corresponding to a constant coupling coefficient in a lossless medium in the form of:

$$S(z) = D_0 \cosh\left(\left|\cosh^{-1}(S_0 / D_0)\right| - mz\right) \tag{6.36}$$

This is equivalent to stating that if we define the signal distribution to be in the form of cosh(mz) the required grating will have a constant coupling coefficient. Figure 6-4(a) compares the exponential (solid line) and cosh (dashed line) signal distributions with the same m value and Figure 6-4(b) illustrates the required apodisation profile respectively.

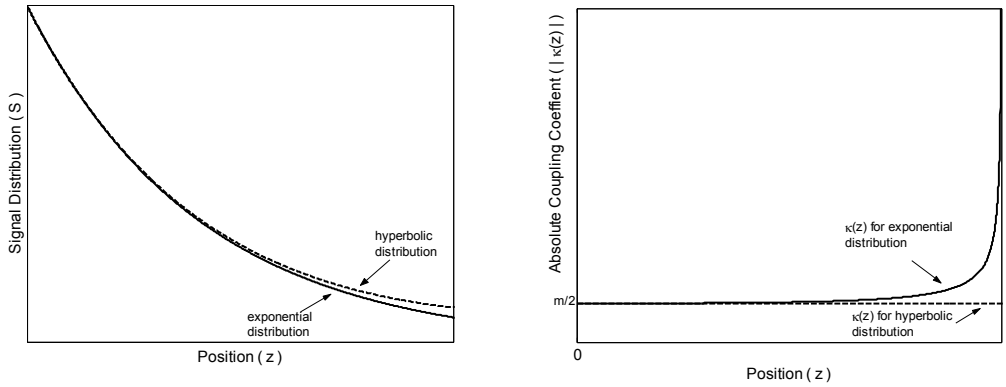

(a) (b)

Figure 6-4 (a) Exponential (solid line) and Hyperbolic (dashed line) signal distributions (b) Corresponding required apodisation profiles.

The comparison of the exponential and hyperbolic distributions show that although these two signal distributions are very close to each other, the apodisation profile for the exponential distribution requires a very large increase over a short distance close to the origin. In practice this may lead to production difficulties whereas the hyperbolic distribution gives a flat apodisation profile and it is much more practical and easier to implement.

6.3.3. Linear Signal Distribution

As a final illustration of the grating design method we define the signal distribution to be linearly decreasing in the form of $S(z) = S_0 - mz$ in the lossless medium with the boundary conditions $S(0) = S_0$ and $D(0) = D_0$. The required apodisation profile is then found as:

$$\kappa(z) = -\frac{m}{2\sqrt{S(z)^2 - D_0^{\,2}}} \tag{6.37}$$

Figure 6-5 below illustrates the defined signal distribution and the corresponding apodisation profile in an unchirped grating.

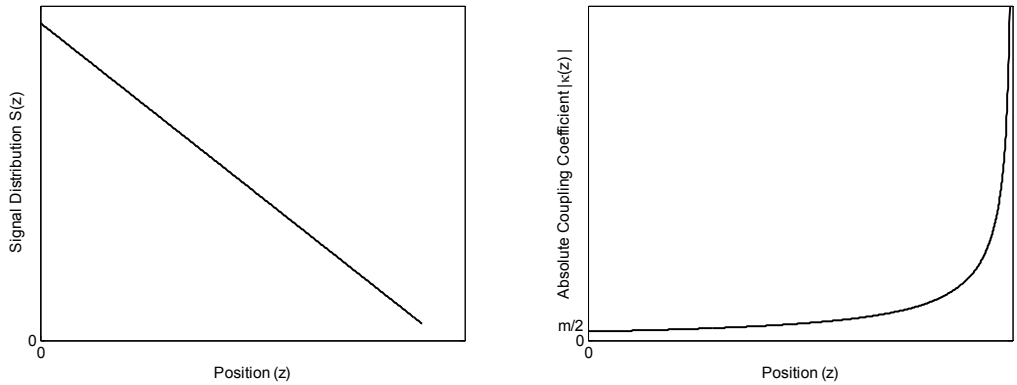

(a) (b)

Figure 6-5 (a) Linearly decreasing signal distribution (b) Corresponding required apodisation profile

6.3.4. Effect of Loss and Gain

So far we derived the gratings in a lossless ($\alpha = 0$) medium. In this section we will investigate the effects of the loss or gain on the designs. We will do so by using numerical examples in which we define the reflectivity, $|r|^2$, to be 0.9. Therefore, the initial values we have at $z = 0$ are S_0=1.9$I_{incident}$ and $D_0 = 0.1I_{incident}$ for a normalised incident signal $I_{incident}$ on the left-hand-side. We define m = 100 m^{-1} for exponential, cosh(mz) and linear distributions, which are shown in Figure 6-6 (a). We will introduce constant loss and gain of values – 5dB/m and +5dB/m, respectively, in the design equations (6.12) and (6.13).

Figure 6-6 (b) shows the apodisation profiles required for the defined exponential distribution in the lossless (solid line), lossy (dashed line) and gain (dotted line) medium. The introduction of loss results in a longer device. This follows from the conservation of energy principle: The defined reflectivity $|r|^2 = 0.9$ in all cases means that 0.9 of the incident field is reflected back. Therefore in the lossless case 0.1 of the signal should be transmitted, and the exponential decrease should drop until $S(L) = 0.1I_{incident}$ which is satisfied at $z = L$ = 28 mm. However in the lossy medium the transmitted signal would be less than 0.1. Therefore, the exponential decrease extends further than the lossless case.

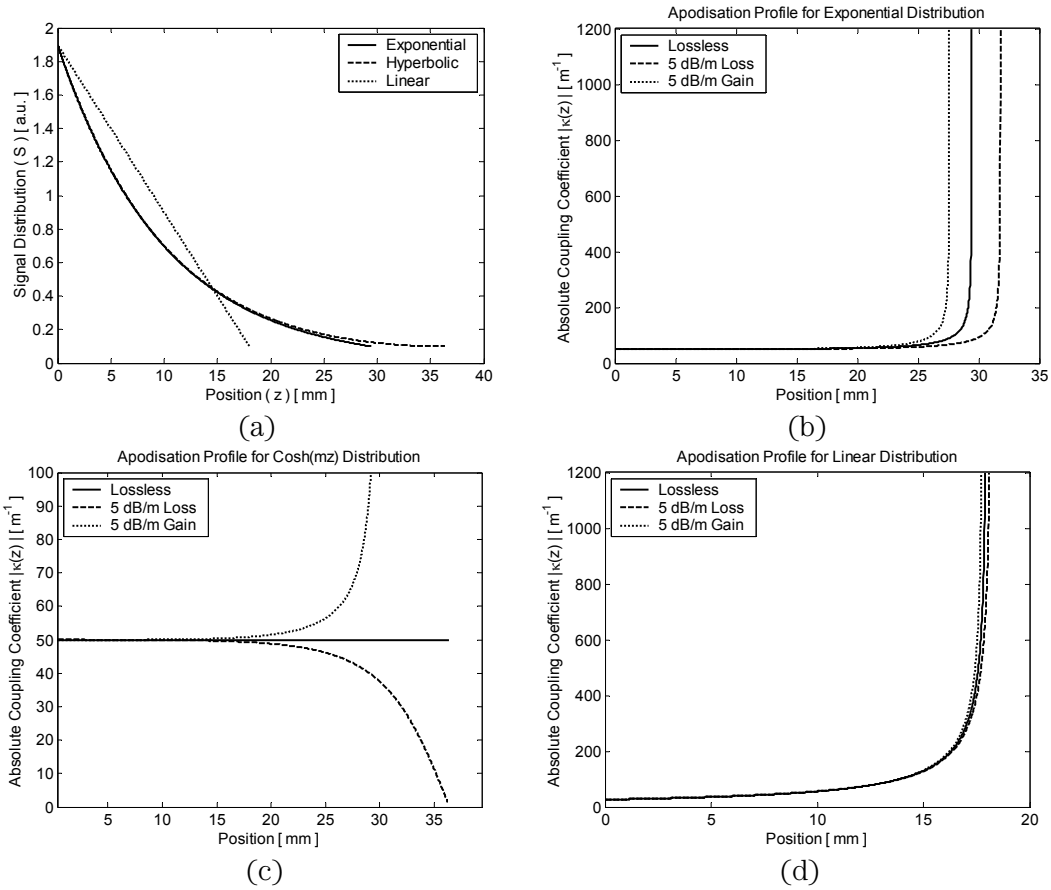

Figure 6-6 (a) 3 different signal distributions: Exponential (solid), hyperbolic (dashed) and linear (dotted). Effect of constant loss and gain in apodisation profiles for (b) the exponential distribution (c) the hyperbolic distribution (d) the linear distribution.

We find the RHS boundary condition is met at z= L = 32 mm and the transmitted signal is $0.08I_{incident}$. Similarly, the gain medium results in a transmitted signal greater than 0.1 hence the exponential decrease and the device length is shorter compared to the lossless case.

We repeat the same analysis for the cosh(mz) and linear distributions as shown in Figure 6-6 (c) and (d), respectively. Although the presence of gain or loss causes a deviation from the constant coupling coefficient $|\kappa| = m/2$ for the cosh(mz) distribution, this deviation is still small compared to the linear and exponential distribution and it is only over a short length. Therefore, in practice, we can say that a constant coupling coefficient grating is associated with a signal distribution very close to a cosh function. In our numerical and experimental studies, therefore, we will use a cosh signal distribution whenever we want to have a constant profile grating. In analytical studies, where we want to highlight the mathematical derivations, we will resort to exponential distributions for the sake of simplicity.

These simple analytical studies conclude the basics of the grating design method for any given signal distribution in reflectors. Now we are ready to continue with the design of laser cavities.

6.4. Design of Laser Cavities

The difference between the passive, or amplifier, cavities and the laser cavities lies in the boundary conditions; in a resonator cavity there are no incident fields at the cavity boundaries but output fields are present as illustrated in Figure 6-7.

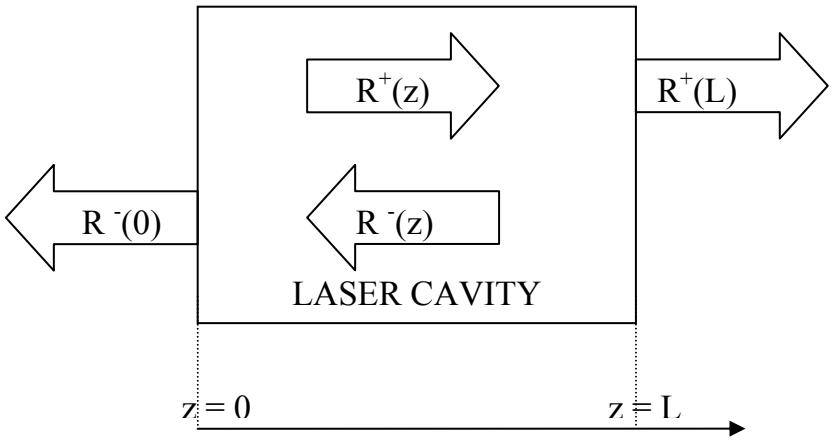

Figure 6-7 Boundary conditions of a generic laser. R^+ and R^- are the amplitude envelopes of forward and backward propagating fields respectively.

Therefore the boundary conditions in a laser cavity are:

Left Boundary Condition at z = 0

No incident field propagating in the forward direction: $R^+(0) = 0$

$$D(0) = -R^-(0)^2 = -S(0) \tag{6.38}$$

Right Boundary Condition at z = L

No incident field propagating in the backward direction: $R^-(L) = 0$

$$D(L) = R^+(L)^2 = S(L) \tag{6.39}$$

Substituting the boundary conditions in Equation (6.17) we find:

$$S(L) + S(0) = \int_0^L 2\alpha(z)S(z)dz \tag{6.40}$$

Observing *S(0)* and *S(L)* are the output powers, Equation (6.40) means that the total output power of the cavity is equal to the generated power inside the cavity. This is basically the analytical way of stating the principle of conservation of energy at the steady-state: If the steady state is reached in a laser cavity, then all the power generated inside the cavity must leave the cavity otherwise it will lead to more energy build up which will contradict with the steady state. Obviously, if we can maximise the efficiency at every point inside the cavity then we will maximise the efficiency of the entire device up to the fundamental limit of the active medium.

Equation (6.40) also provides information on the directionality of the laser. If one of the output powers can be set to zero then all the generated power will leave the cavity from the opposite end making the device completely uni-directional.

6.4.1. Laser with Uniform Distribution

Let us start designing laser cavities with a very special case where we would like to obtain a constant intensity distribution and assume that the gain is also constant throughout the medium. That is; $S(z) = S$ and $\alpha(z) = \alpha$, which when substituted in Equation (6.12) gives:

$$D(z) = 2\alpha S z + D(0) \tag{6.41}$$

Using the left boundary condition given by Equation (6.38) we find $D(0) = -S$, then:

$$D(z) = S(2\alpha z - 1) \tag{6.42}$$

The right boundary condition imposes the length of the device, L. Since at the RHS boundary $D(L) = S$ using Equation (6.42) we find:

$$L = \frac{1}{\alpha} \tag{6.43}$$

Substituting S, α, D and $\Lambda(z)$ in Equation (6.13) we find the required coupling coefficient profile as:

$$\kappa(z) = \frac{\alpha(1-2\alpha z)}{2\sqrt{\alpha z(1-\alpha z)}} \frac{1}{\cos\left[\Gamma(z)\right]} \tag{6.44}$$

If we wish to have a grating whose Bragg wavelength matches the signal wavelength without any chirp, then $\beta = \frac{\pi}{\Lambda}$ and the cosine term in Equation (6.44) is simply equal to

1 for all z. In that case we find that at $z = 0$, κ is infinitely large and drops to 0 at $z = L/2$ whereas at larger z values κ becomes negative and it approaches to negative infinity at $z = L$, as shown in Figure 6-8 for two different gain values (α).

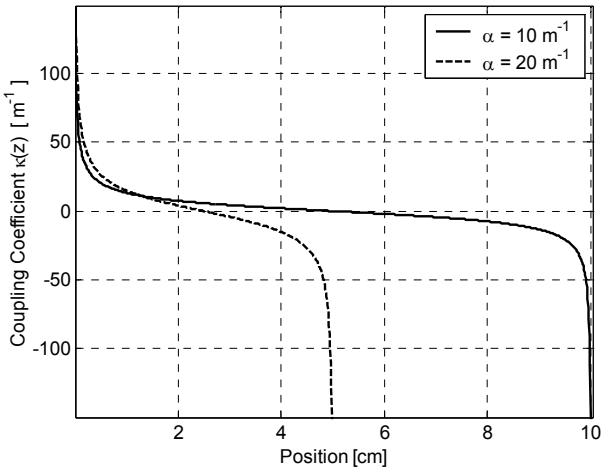

Figure 6-8 Apodisation profiles for constant signal distribution with two different gain values.

The coupling coefficient κ defines the amount of the periodic perturbation required. If this perturbation is a sinusoidally varying refractive index modulation in the form of:

$$n = n_0 + \Delta n \cos(\phi(z)) \tag{6.45}$$

where Δn is the amplitude of modulation and ϕ is the phase of a sinusoidal grating, then the coupling coefficient is related to this perturbation by:

$$\kappa(z) = \frac{\Delta n(z)\pi}{\lambda} \tag{6.46}$$

In such a grating the sign change in the coupling coefficient can be achieved by introducing a π-shift in the phase of grating.

These results are identical to those of G. Morthier and R. Baets [1] where their analysis is limited to this special case of constant intensity and gain employing simplified equations.

6.4.2. Laser with Varying Distribution

Now let us consider a varying signal distribution; In this case, we assume the distribution to have an exponential variation close to the ends of the cavity and to be constant in between as shown in Figure 6-9. We assume the gain to be constant throughout the entire structure for the sake of simplicity.

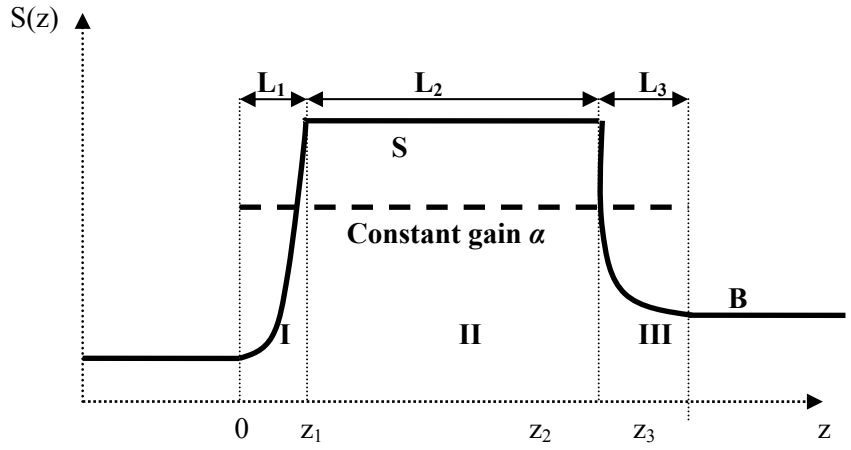

Figure 6-9 Constant signal distribution with exponential transitions at the ends of the cavity.

Now for the given S(z) and $\alpha(z)$ we will solve Equations (6.12) and (6.13) to calculate the required coupling coefficient profile. Since there are three separate intensity distributions defined in the active medium, we divide our analysis into three segments.

Segment I:

Between 0 and z_1, over a length of L_1, the total intensity distribution and gain are given as:

$$S_I(z) = S_0 e^{mz} \qquad \alpha(z) = \alpha$$

We solve Equation (6.12) with the left boundary condition, $D(0) = -S_0$ and find D(z) in Segment I as:

$$D_I(z) = \frac{2\alpha}{m} S_I(z) - S_0\left(1 + \frac{2\alpha}{m}\right) \qquad ;0 < z < z_1 \tag{6.47}$$

Initial condition for Segment II is then:

$$D(z_1) = S_0\left(\frac{2\alpha}{m} e^{mL_1} - \frac{2\alpha}{m} - 1\right) \tag{6.48}$$

Segment II:

$$S_{II}(z) = S_C = S_0 e^{mL_1} \qquad \alpha(z) = \alpha$$

We find

$$D_{II}(z) = 2\alpha S_c (z - z_1) + D(z_1) \qquad ; z_1 < z < z_2 \tag{6.49}$$

Segment III:

Signal decreases exponentially therefore:

$$S_{III}(z) = S_C e^{-n(z-z_2)} \qquad \alpha(z) = \alpha \tag{6.50}$$

with initial condition:

$$D(z_2) = 2\alpha S_c L_2 + D(z_1) \tag{6.51}$$

and we find

$$D_{III}(z) = -\frac{2\alpha}{m} S_{III}(z) + \frac{2\alpha}{n} S_c + D(z_2) \qquad ; z_2 < z < z_3 \tag{6.52}$$

Now we substitute *S(z)*, *α(z)* and the calculated *D(z)* into Equation (6.13) and assuming no chirping we find:

$$\kappa = \begin{cases} \dfrac{1}{\sqrt{\left(\dfrac{S_I}{D_I}\right)^2 - 1}} \left(\dfrac{m}{2} \dfrac{S_I}{D_I} - \alpha \right) & ; 0 < z \le z_1 \\ \dfrac{-\alpha}{\sqrt{\left(\dfrac{S_{II}}{D_{II}}\right)^2 - 1}} & ; z_1 < z \le z_2 \\ \dfrac{1}{\sqrt{\left(\dfrac{S_{III}}{D_{III}}\right)^2 - 1}} \left(-\dfrac{n}{2} \dfrac{S_{III}}{D_{III}} - \alpha \right) & ; z_2 < z \le z_3 \end{cases} \tag{6.53}$$

Figure 6-10 shows the solution for $\kappa(z)$ with the following parameters in a fibre with core radius of 2.3 μm.

$S(0)$ = 1 mW / core area

Constant gain α = 10 m^{-1}

Exponential coefficient in the first section m = 500 m^{-1}

Length of first section L_1 = 10 mm

Length of second section L_2 = 20 mm

Exponential coefficient in the third section n = 500 m^{-1}

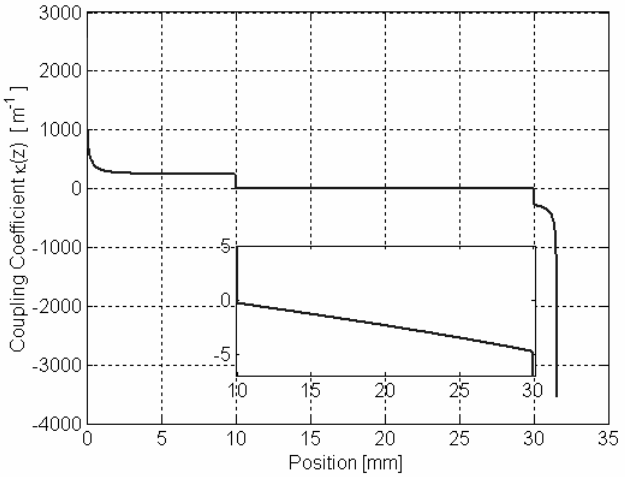

Figure 6-10 Apodisation profile derived for 3-segment intensity distribution

Here we define the left output power to be 1 mW and the corresponding signal intensity $S(0)$ is found by simply dividing the power by the core area assuming uniform distribution inside the core.

Length of the final section is found as L_3 = 2mm by imposing the right boundary condition, giving a total length of 32 mm

This apodisation profile has a resemblance to a DBR laser cavity however a closer look at the middle section (see inset) shows that, although quite weak, there is a grating. The presence of this grating provides the wavelength selectivity. The sign change in the coupling coefficient at z = 10 mm corresponds to a π phase-shift, which in combination with the weak grating, assures that the cavity has a single longitudinal mode coincident with the Bragg wavelength, as opposed to a DBR structure with multiple longitudinal modes. The specific shape of the apodisation profile keeps the signal distribution constant as we desired. Therefore, strictly speaking; this structure is a complex DFB laser.

Figure 6-11 shows the signal distributions inside the grating calculated by using the simulation tool described in Chapter 3. This apodisation profile in the given active medium sustains the desired signal distribution and meets the boundary condition as the figure and the inset shows.

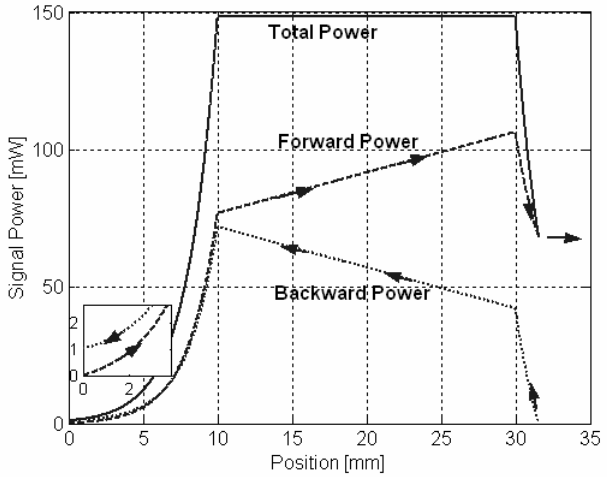

Figure 6-11 Forward, backward and total signal power distributions in the cavity. Forward and backward distributions indicate that the boundary conditions are met.

As required, $S(0)$, which is the left-end output power, is 1 mW. Up to z = 10 mm the total signal power increases exponentially with m = 500 m^{-1} and for another 20 mm remains constant. Then it drops exponentially with n = 500 m^{-1}. At z = 32 mm the right boundary condition is met, that is the backward input power is zero, and the forward power becomes the output from the right end. We find this output power to be 68 mW.

6.5. Grating Design for Maximum Laser Efficiency

Our aim is to design lasers with ultimate efficiency. Therefore, instead of an arbitrary signal distribution we will first calculate the *optimum signal distribution* that results in the maximum possible efficiency. In this section we present the definition and calculation of the optimum signal powers before we continue with the cavity design algorithm. We also present an example of the design of a laser with maximum efficiency in a simple Yb doped fibre.

6.5.1. Optimum Signal Intensity

At a position z, where a signal photon is generated, the absorption of pump power also takes place. Although the same arguments apply to electrically pumped media here we will focus on the optical pumping, therefore, we will assume that power is delivered to the medium by pump photons.

If G is the net generated signal over a volume as given by Equation (6.17) then ΔG defined as:

$$\Delta G(z) = \frac{dG}{dz} = 2\alpha(S,P)S(z) \tag{6.54}$$

is the net signal generated per unit length. Here α is the net gain coefficient for a signal field resulting from the gain due to stimulated emission (α_S) and loss due to constant background losses (ε_s):

$$\alpha(S,P) = \alpha_S(S,P) - \varepsilon_S \tag{6.55}$$

And similarly ΔP:

$$\Delta P = -2\alpha_P(S,P)P(z) \tag{6.56}$$

is the absorbed pump per unit length, where α_p is the absorption coefficient for the pump field, and P is the pump power. Since the absorption coefficient α_p is negative, here we multiplied the RHS of the equation by -1 so that ΔP is a positive number. Then the local conversion efficiency, η, from pump to signal at position z is:

$$\eta(S,P) = \frac{\Delta G(S,P)}{\Delta P(S,P)} \tag{6.57}$$

η is a function of both signal, S, and pump power, P, and it is governed by the rate equations and losses of the active medium.

Equation (6.57) indicates that for a given pump P there exists a certain signal power S_{opt} such that the conversion efficiency, η, is maximum, locally. Using Equations (6.54) - (6.56) we can re-write Equation (6.57) as:

$$\eta(S,P) = \frac{\left(\alpha_S(S,P) - \varepsilon_S\right)S}{\left(\alpha_P(S,P) - \varepsilon_P\right)P} \tag{6.58}$$

In general the pump absorption and the signal generation as well as the loss mechanisms, such as excited state absorption and co-operative up conversion, are functions of both signal and pump power. Therefore maximisation of Equation (6.57) is, in general, only a numerically solvable problem.

This pump power dependent maximum conversion efficiency will be central to our discussion in the forthcoming sections, therefore it is useful to explore the implications of this concept at this stage.

Assume that we are interested in a pump power range from 0 to P_{input} For each pump power between 0 and P_{input} we find the corresponding optimum signal S_{opt} as illustrated in Figure 6-12 (a) and we calculate the maximum possible conversion efficiency for each pump power as illustrated in Figure 6-12(b). For the purpose of illustration here the maximum efficiency is decreasing with increasing pump power.

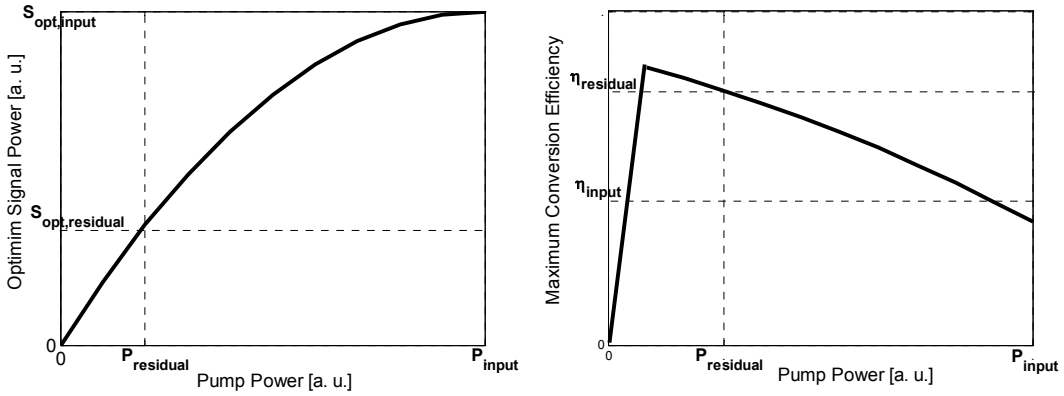

Figure 6-12 : Ullustration of pump power dependent (a) Optimum Signal Power (b) Maximum Conversion Efficiency

Now, there is a very important question we need to ask: If we launch a pump power P_{input} into the active medium, when it is totally absorbed, what is the maximum conversion efficiency that we can get. From the Figure 6-12(b), the immediate answer follows to be η_{input}. This answer, unfortunately, is partially correct. The maximum conversion efficiency for P_{input} would be η_{input} if the pump power where absorbed at one step over an infinitesimal length. Now consider a realistic picture: When the pump power is launched into an active medium, it will propagate while it is being absorbed therefore its value will longitudinally vary. When it is completely absorbed the pump power will have a variation starting from P_{input} at z = 0 down to 0 at position z = L. Therefore the maximum possible conversion will also vary from η_{input} down to 0. In this realistic case, therefore the maximum overall conversion efficiency will be a weighted average of the efficiency values for pump powers between 0 and $P_{input.}$ This value can be easily calculated from the figure by taking the integral of the efficiency curve in Figure 6-12 (b) and dividing it by P_{input}

There can be certain cases, as we will encounter later, the pump absorption is not total and there is a residual pump power $P_{residual}$. In that case, the overall maximum efficiency

possible with respect to the absorbed pump power will be the mean value between $P_{residual}$ and P_{input}.

We will investigate the longitudinal variation of the pump power and optimum signal in much more detail when we consider numerical examples. At this stage it is sufficient to say that for a given input pump power we can calculate the pump power and the gain distribution in conjunction with the corresponding optimum signal distribution. Once we calculate $S_{opt}(z)$ and $\alpha(z)$ we can solve for the required coupling coefficient profile as explained in the previous section.

6.5.2. Calculation of Optimum Signal in Yb Doped Fibre

Now we will consider a Yb doped fibre and demonstrate the optimum signal distribution and the maximum efficiency laser design concepts with numerical values in this somewhat simple medium. We will tackle the more complex problem of an Er/Yb doped medium in the next chapter.

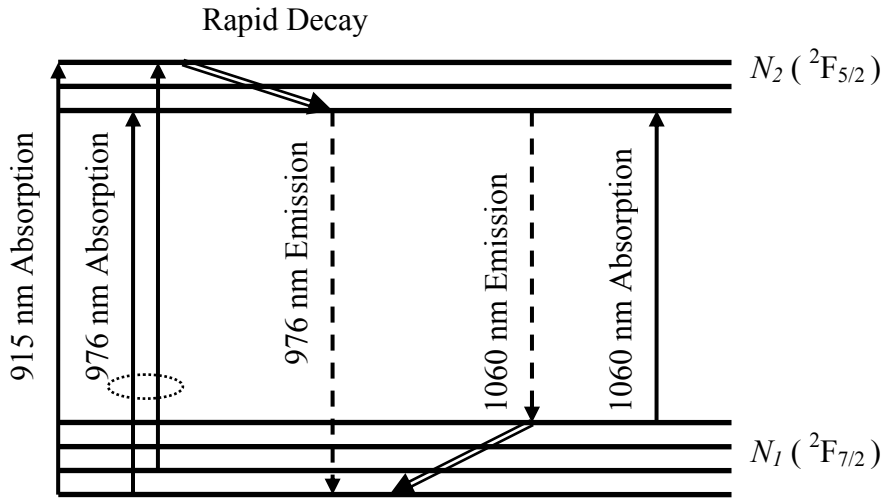

Figure 6-13 Energy Level Diagram of Yb Ions

Figure 6-13 illustrates the energy levels and transitions in Yb ions, which have 4 Stark split levels at the ground level $^2F_{7/2}$ manifold and 3 levels in excited state $^2F_{5/2}$ manifold. The 976 nm pump field excites ground level ions with density N_1 to the excited state with denisty N_2. When pumped with 915 nm, this medium operates as a 3 –level system if the signal wavelength is around 976 nm, since absorption and emission cross-sections are almost equal. For signal wavelengths longer than 1100 nm the medium is a 4-level system due to lack of any signal absorption. For signals between 976-1100 nm the Yb doped medium can be considered as a quasi-4 level system. We will design the laser to operate at 1060 nm in this quasi-4-level region. For more about the modelling of Yb doped media see for example [3,4].

Ions at the higher sub-levels of the $^2F_{5/2}$ manifold almost instantaneously decay to the lower sub-levels. Due to the rapid nature of this transition we assume that all the excited state ions are at the lower sub-level, with a concentration of N_2. From this lower sub-level of the excited state, the ions undergo stimulated as well as spontaneous emission over a broad range of wavelengths. With these two concentrations we can write the steady-state rate equation for the medium as:

$$\frac{dN_1}{dt} = -N_1\left(\frac{P}{h\nu_p}\sigma_{p,a} + \frac{S}{h\nu_s}\sigma_{s,a}\right) + N_2\left(\frac{P}{h\nu_p}\sigma_{p,e} + \frac{S}{h\nu_s}\sigma_{s,e} + \frac{1}{\tau}\right) = 0 \qquad (6.59)$$

and we observe

$$N_T = N_1 + N_2 \qquad (6.60)$$

where N_T is the total ion concentration, h is Planck's Constant, ν is the frequency, σ is the cross-section for which sub-scripts s and p stand for the signal and the pump frequencies, and a and e denote absorption and emission respectively. Finally τ is the life-time of the ions at the excited state. If we assume the signal and pump have complete overlap with the active medium for simplicity then the propagation of signal and pump in this medium leads to the amplification and absorption, respectively, given by:

$$\begin{aligned}\frac{dG}{dz} &= 2\left(\alpha_S(S,P) - \varepsilon_S\right)S(z)\\ \frac{dP}{dz} &= 2\left(-\alpha_P(S,P) + \varepsilon_P\right)P(z)\end{aligned} \qquad (6.61)$$

where ε_S and ε_P are again the constant background field losses for signal and pump. The field gain coefficients, α_s and α_p, are found from the rate-equations as:

$$\begin{aligned}2\alpha_s &= N_2\sigma_{s,e} - N_1\sigma_{s,a}\\ 2\alpha_p &= N_2\sigma_{p,e} - N_1\sigma_{p,a}\end{aligned} \qquad (6.62)$$

Solving Equations (6.59) and (6.60) for N_1 and N_2 and substituting into Equation (6.62) we can re-write the conversion efficiency Equation (6.58) as (See Appendix A for derivation in detail):

$$\eta = \frac{\left[\frac{P}{h\nu_p}\left(\sigma_{s,e}\sigma_{p,a} - \sigma_{s,a}\sigma_{p,e}\right) - \frac{\sigma_{s,a}}{\tau} - \varepsilon_s\left(\frac{E+A}{N_T}\right)\right]S}{\left[\frac{S}{h\nu_s}\left(\sigma_{s,e}\sigma_{p,a} - \sigma_{s,a}\sigma_{p,e}\right) + \frac{\sigma_{p,a}}{\tau} + \varepsilon_p\left(\frac{E+A}{N_T}\right)\right]P} \tag{6.63}$$

where emission, E, and absorption, A, terms are defined as:

$$\begin{aligned} A &= \left(\frac{P}{h\nu_p}\sigma_{p,a} + \frac{S}{h\nu_s}\sigma_{s,a}\right) \\ E &= \left(\frac{P}{h\nu_p}\sigma_{p,e} + \frac{S}{h\nu_s}\sigma_{s,e} + \frac{1}{\tau}\right) \end{aligned} \tag{6.64}$$

If the background losses are zero (i.e. $\varepsilon_s = \varepsilon_p = 0$), and the life-time of the excited-state, τ, is very large compared to the absorption cross sections, the efficiency given by Equation (6.63) simplifies to:

$$\eta_{QL} = \frac{\nu_S}{\nu_P} = \frac{\lambda_P}{\lambda_S} \tag{6.65}$$

η_{QL} is the well known quantum limit for the conversion from the pump wavelength to the signal wavelength in a lossless medium without spontaneous emission.

Although in this medium with a minimum number of transitions the efficiency term could analytically be solved for the optimum signal intensity for a given pump power, a numerical solution is more convenient, and in general, it is the only solution method in a more complex medium. Therefore let's consider the numerical example whose details are given in Figure 6-14.

In this fibre we assume that the ions are uniformly distributed across the cross-section and that the signal and the pump fields have a complete overlap with this doped region. We assume 1% of the ions have their lifetime quenched and act as an unsaturable loss. For the sake of simplicity, we assume that the combined effect of this unsaturable loss and any other background losses, is equal to 0.5 m^{-1} both at pump and signal wavelengths ($\varepsilon_s = \varepsilon_p = 0.5 m^{-1}$).

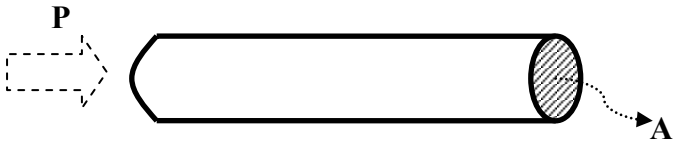

$\lambda_p = 976$ nm
$\lambda_s = 1060$ nm
$N_T = 8 \times 10^{25}$ m^{-3}
$\sigma_a^p = 13.5 \times 10^{-25}$ m^2
$\sigma_e^p = 13.8 \times 10^{-25}$ m^2
$\sigma_a^s = 2.94 \times 10^{-27}$ m^2
$\sigma_e^s = 1.60 \times 10^{-25}$ m^2
$\tau = 2$ ms
$A = \pi(2.3\mu m)^2$
$\varepsilon_s = \varepsilon_P = 0.5 m^{-1} = 4.34$ dB/m

Figure 6-14 Yb doped fibre geometry and spectroscopic parameters

We can calculate the generated signal per unit length, *ΔG(S,P),* by calculating the Equation (6.54) numerically. Figure 6-15(a) shows the total signal generated by stimulated emission (dashed line), the absorbed signal by the background loss (dotted line) and the net generated signal *ΔG* (solid line) as a function of signal power for pump power = 200 mW.

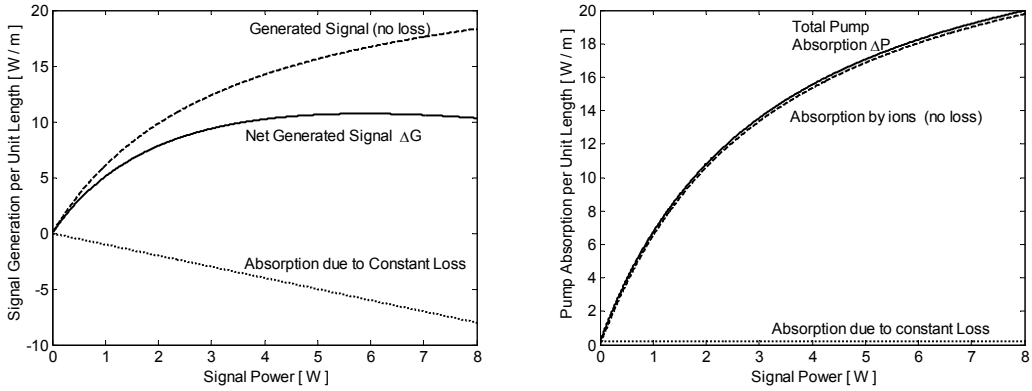

(a)

(b)

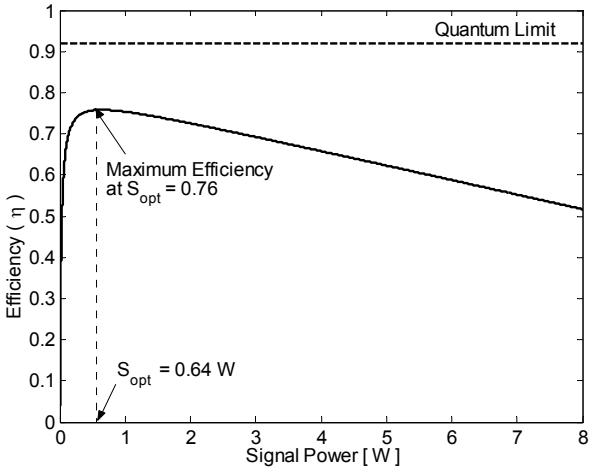

(c)

Figure 6-15 For pump power = 200 mW (a) Generated signal per unit length as a function of signal power (b) Absorbed pump per unit length as a function of signal power (c) Variation of the efficiency with signal power.

In the absence of loss the total generated signal increases monotonically and saturates with increasing signal power due to the limited number of Yb ions. However, the signal loss increases linearly with signal power in the form $2\varepsilon_s S$ due to the constant loss. Therefore the net generated signal begins to drop when the saturation of signal generation is overtaken by the increasing signal loss.

Similarly Figure 6-15(b) shows the breakdown of the pump power absorption. Increasing signal power results in larger stimulated emission consequently more pump power is absorbed by the ions returning to the ground level; however, since the number of ions is finite, pump absorption gradually saturates with larger signal. Pump loss due to the background loss is constant regardless of the signal power since this loss term is a function of pump power only in the form $2\varepsilon P$. In Figure 6-15(c) we combine $\Delta G(S)$ and $\Delta P(S)$ curves to calculate the conversion efficiency, $\eta(S) = \Delta G(S) / \Delta P(S)$, as a function of signal power for the given pump power of 200 mW. In the ideal lossless case the generated signal and the absorbed pump power increases proportionally at the quantum limit as shown analytically by Equation (6.63). Therefore in the lossless case there is no optimum signal. Any signal value results in the quantum efficiency. In the real world, however, where losses are inevitable, the presence of loss mechanisms define an optimum signal power (S_{opt}), which, for the given pump power, results in maximum efficiency. In this example for the given pump power of 200 mW the maximum efficiency is obtained when the signal is at the optimum value, S_{opt} = 0.64 W, yielding a 0.76 conversion coefficient.

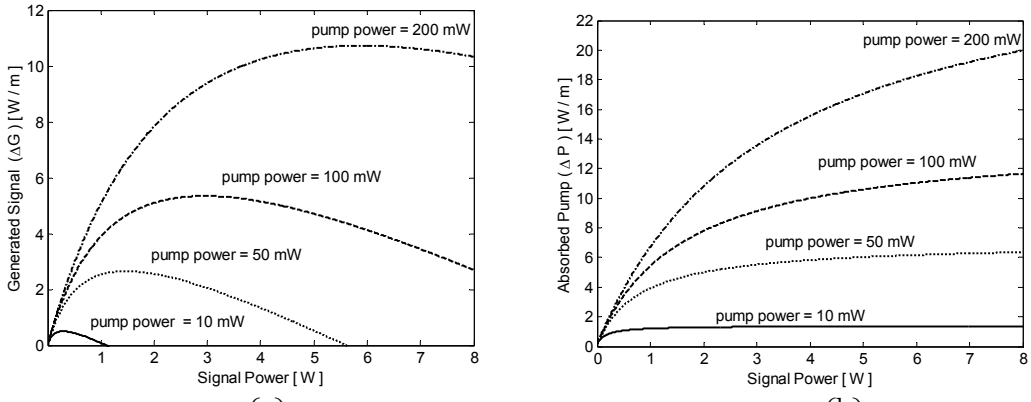

(a) (b)

Figure 6-16 (a) Net generated signal G as a function of signal power at different pump powers (b) Total absorbed pump ΔP as a function of signal power at different pump powers

We can carry out the identical analysis for different pump powers in order to calculate the net generated signal per unit length (ΔG) and the total absorbed pump power per

unit length (ΔP). Figure 6-16(a) and (b) show ΔG and ΔP, respectively, for the pump powers 10, 20, 50 and 200 mW.

We combine these two plots to find the conversion efficiency $\eta(S) = \Delta S(S)/\Delta P(S)$ for different pump powers as shown in Figure 6-17 below.

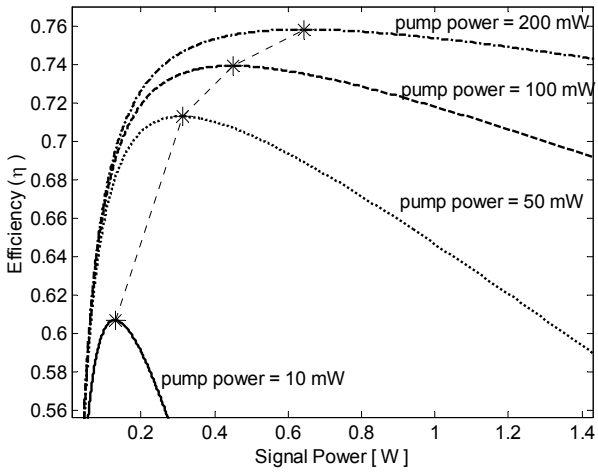

Figure 6-17 Efficiency vs. signal power at different pump powers

From each peak in Figure 6-17 (marked with stars) we find the optimum signal power and the corresponding maximum efficiency for each pump power. In this manner we can calculate the optimum signal values and maximum efficiencies for all the pump powers of interest. Figure 6-18 shows the result of this analysis for pump powers between 0 and 310 mW.

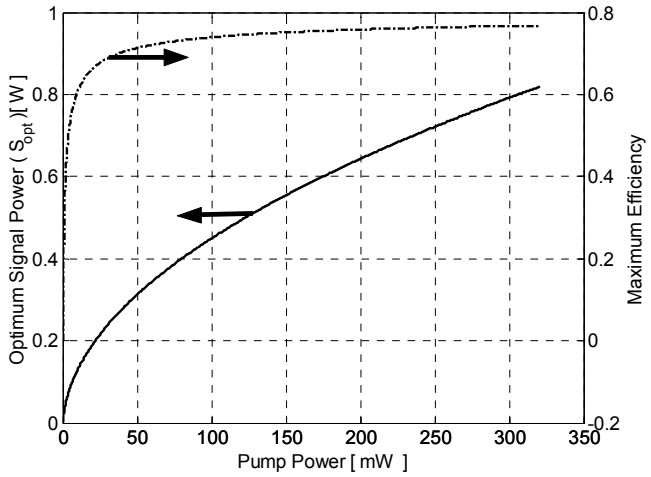

Figure 6-18 Optimum signal power and corresponding maximum efficiency for pump powers from 0 up to 310 mW.

The solid curve shows the optimum signal values (left y-axis) and the dotted curve is the corresponding maximum efficiency possible in this particular medium at the given pump

power. Figure 6-19(a) shows the resultant optimum gain coefficients, α, and Figure 6-19(b) shows the generated signal and absorbed pump powers at these optimum signal values.

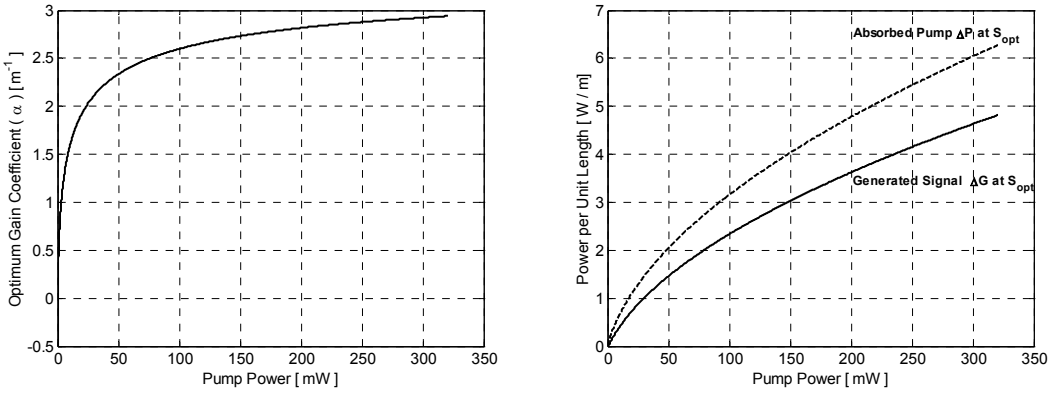

(a) (b)

Figure 6-19 (a) Optimum gain coefficient (b) Generated signal and corresponding absorbed pump powers at optimum signal powers for pump powers between 0 and 310 mW.

6.5.3. Longitudinal Distribution of Optimum Signal in Yb doped fibre

As mentioned earlier, if there were no losses present in the medium (ε = 0) then the maximum efficiency would be equal to the quantum efficiency, which is 0.92 for the pump wavelength 976 nm and the signal wavelength 1060 nm. However due to the loss mechanisms present in this medium the maximum conversion efficiency is pump power dependent and varies from a very small value at low pump powers and then tends asymptotically to 0.77 at very large pump powers. If, for example, 200 mW pump power is launched into the fibre then the ultimate conversion efficiency would be 0.76, however, this would require total absorption of the all power over an infinitely small distance. In reality the pump power will be absorbed gradually, due to the finite number of ions in the cross-section of the fibre, and with decreasing pump power the conversion efficiency will drop as Figure 6-18 illustrates. That is; the optimum signal will have a longitudinal distribution following the gradual absorption of the pump power down the fibre. If the pump power leaving the medium unabsorbed is, say, 11 mW then the maximum possible efficiency will be the weighted mean value of the efficiency curve between pump powers 11 and 200 mW, which is 0.73. Therefore for the total absorbed 189 mW pump power the maximum signal output power would be 138 mW.

In order to design the cavity for this ultimate efficiency we need to calculate the spatial distribution of the pump power and the corresponding optimum signal power. The translation from the optimum signal curve in Figure 6-18 to the spatial distribution of the

optimum signal power can be best illustrated with an example: Let us assume that 200 mW pump power is incident on the fibre laser at $z = 0$ as shown in Figure 6-20.

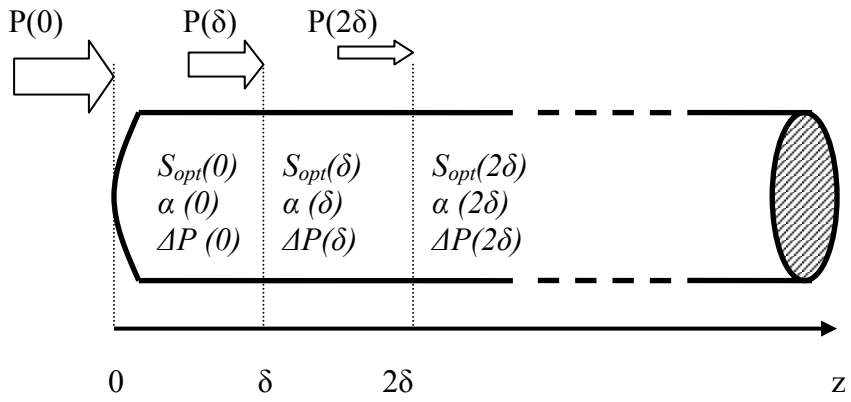

Figure 6-20 Numerical method for the calculation of pump power, optimum intensity and gain distributions.

From Figure 6-18 we read the optimum signal power corresponding to $P(0)$=200 mW is $S_{opt}(0)$ = 0.63 W at z = 0. For these values of pump and signal, we use the rate equations to find the signal gain $\alpha(0)$ and pump absorbed per unit length $\Delta P(0)$ as we have done in Figure 6-19(a) and (b). If we assume that the pump and signal powers are constant over a very short segment of length δ then we can calculate the pump power arriving at $z = \delta$ as:

$$P(\delta) = P(0) - \Delta P(0)\delta$$

For this new pump power value, again we find the corresponding optimum signal power from Figure 6-18 and use rate equations to calculate the new signal gain and pump power absorption at $z = \delta$. As illustrated in Figure 6-20, we continue to obtain the optimum signal intensity distribution and the corresponding signal gain until the pump power drops to 0 and as a result we obtain the pump, optimum signal and gain distributions, as in Figure 6-21 (a)-(c).

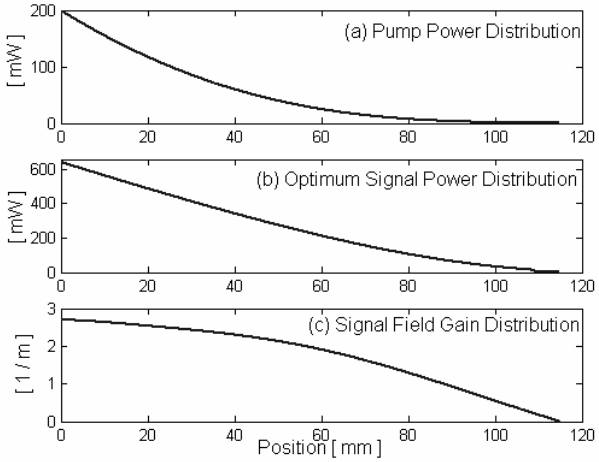

Figure 6-21 (a) Pump power (b) Optimum signal and (c) Gain distributions

6.5.4. Ultimate Efficiency Laser Design in Yb doped fibre

Figure 6-21 provides all the longitudinal distributions we need to calculate the coupling coefficient profile required for the ultimate conversion efficiency through Equations (6.12) and (6.13). In order to solve these equations, however, we need to define the initial value $D(0)$ which will set the laser boundary condition at z = 0. The other boundary condition $D(L)$ will follow from the total generated signal in the cavity and the defined boundary condition $D(0)$ given by Equation (6.17) due to the conservation of energy principle, as discussed in Section 6.2. For example, if we want the laser to be completely uni-directional in the $(+)z$ direction then we define $D(0) = 0$, so that no power leaves the cavity from the left-hand side (i.e. $R^{-}(0) = 0$). With this initial value at $z = 0$ and the calculated optimum spatial $S_{opt}(z)$ and $\alpha(z)$ distributions we are ready to design the grating.

First we calculate $D(z)$, by substituting $S_{opt}(z)$ and $\alpha(z)$ in Equation (6.12). The calculated $D(z)$ (dotted line) is shown in Figure 6-22, along with $S(z)$ (solid line). The second boundary condition on the RHS, given by Equation (6.39), is satisfied at $z = 74$ mm. This determines the device length, L, to be 74 mm. This example illustrates that the LHS boundary condition (Equation (6.38)) defines the degree of the laser uni-directionality, while the RHS boundary condition (Equation (6.39)) defines the total laser length.

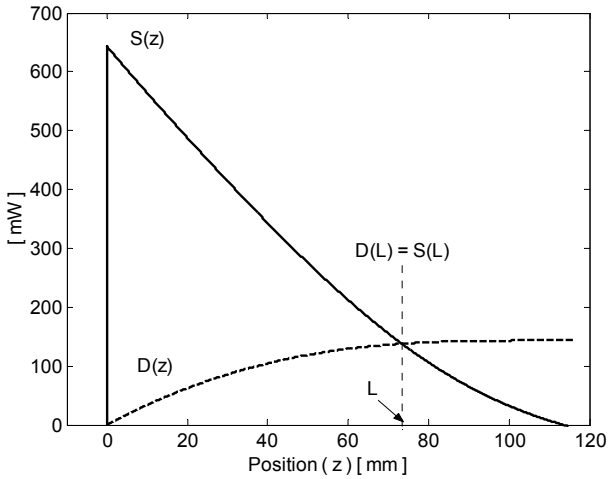

Figure 6-22 Optimum signal distribution *S(z)* and corresponding signal difference *D(z)*

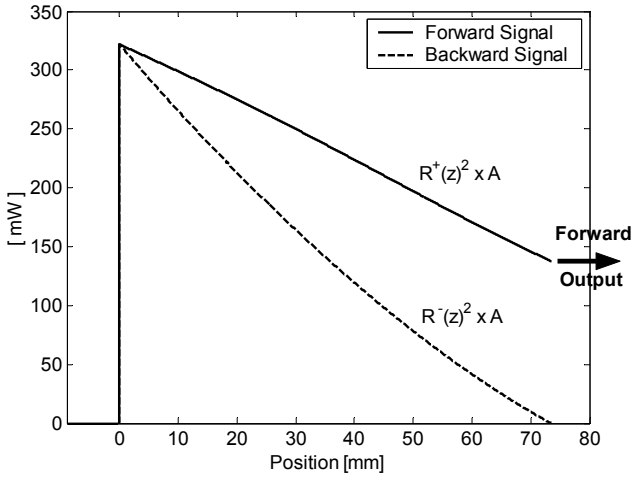

Figure 6-23 Powers of forward and backward propagating fields

Knowing *S(z)* and *D(z)* we can use Equations (6.8) and (6.9) in order to calculate the spatial distributions of individual fields, $R^{+}(z)$ and $R^{-}(z)$, propagating in opposite directions. Figure 6-23 shows the power distributions of these fields. At $z = 0^{+}$, just inside the cavity, we find that the backward and forward propagating fields are equal as expected; since we defined no backward field to leave the cavity from the LHS, all of the backward field must be reflected into the forward direction. At $z = 74$ mm the backward propagating field drops to 0, which is the second boundary, and the forward propagating field leaves the cavity as the output power in $(+)z$ direction. We find the residual pump power leaking out in the forward direction, *P(L)*, to be 11 mW and the signal output power to be 138 mW. The pump power cannot be converted into signal power at the maximum efficiency any further since the optimum signal values, corresponding to pump powers less than 11 mW, are smaller than 138 mW (see Figure 6-18). Therefore any attempt to convert the residual pump power will compromise the conversion efficiency in

this co-directional pumping scheme. We will show how to reduce the residual pump power by using alternative pumping schemes in the next Chapter.

Now we substitute $S(z)$, $\alpha(z)$ and $D(z)$ in Equation (6.13) to calculate the required apodisation profile $\kappa(z)$ between 0 and 74 mm, assuming no chirping and that the signal wavelength matches the Bragg wavelength. The result is shown in Figure 6-24. This derived cavity has a conversion efficiency of 0.73 with respect to the absorbed pump power, which is the ultimate limit as we calculated from the maximum efficiency curve earlier for pump powers between 11 and 200 mW in Section 6.5.3.

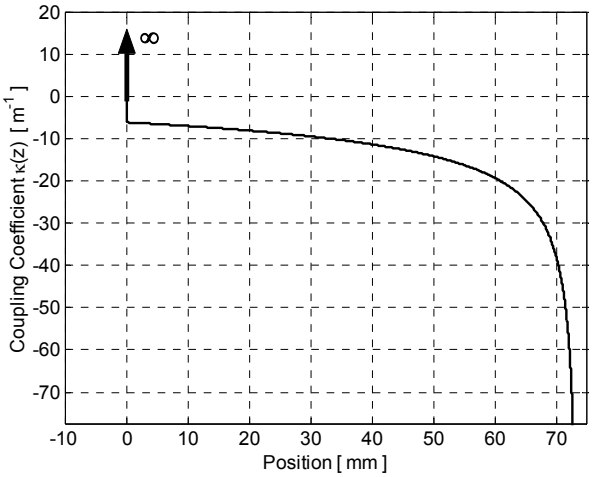

Figure 6-24 Apodisation profile providing the maximum efficiency

This example illustrates the application of the design method. For the given pumping scheme (i.e. co-directional pumping from one end), given active medium (Yb doped fibre) and for the chosen sharp LHS transition in the power from optimum value $S_{opt}(0^+)$ to 0 at $z = 0$ (See Figure 6-22) for complete uni-directionality we found that the RHS boundary condition is met in a self-consistent way within the distributed feedback structure. This combination of the LHS and RHS transitions in power at the boundaries is one of the three possibilities that may occur. Appendix B details and discusses each case individually. For example the infinitely large coupling coefficient required at $z = 0$ due to the zero left output condition can be achieved by using either a very long and strong grating written in a very low loss fibre, to prevent unnecessary pump absorption, or by a mirror. However, in either case the reflector needs to be spliced to the grating in the active medium in precise phase-relation so that the lasing signal wavelength matches the grating Bragg wavelength. This, however, is rather impractical with the technology currently available. An alternative solution to this problem, as illustrated in Appendix B as one of the possible transitions, is to reduce the defined uni-directionality: By allowing a very small output power in the backward direction, and defining a smooth increase in

the signal power to the optimum value over a short length, a feasible apodisation profile entirely in the active medium can be obtained without compromising the efficiency significantly.

6.6. Conclusions

We have developed the theoretical basis for designing gratings that would give any desired signal distribution both in passive and active media. In addition to the signal distribution, the design algorithm requires a certain chirp profile and gain distribution. So far in all our designs we assumed no chirping, for the sake of simplicity, and showed that the gain distribution can be set to a constant value or can be calculated from the rate equations of the medium in conjunction with the corresponding signal and pump distributions. We discussed the boundary conditions and showed how the second boundary condition in these 1-dimensional structures dictates the device length. We illustrated these concepts by designing reflectors and lasers with various internal signal distributions.

We introduced the concept of optimum signal power for the maximum conversion efficiency from pump to signal. The optimum signal power, the corresponding gain and the maximum efficiency are found by solving the rate equations of the active media numerically. These optimum values are then mapped spatially following the pump power distribution. Combining the spatial distributions with the grating design method, we developed a novel analytical laser design method that makes no *a priori* assumption about the cavity structure and sustains the optimum signal distribution for a given active medium and waveguide geometry. Therefore at every point along the cavity the pump is absorbed in the best possible way, and the result is the maximum possible conversion efficiency from the absorbed pump power to the generated signal power. According to the steady-state condition the generated power cannot be stored in the cavity. Therefore, if the background loss is small then the out-coupled power is practically equal to the total generated power, resulting in the ultimate output signal – absorbed pump power ratio for the device. These concepts are illustrated with numerical studies in a simplifed model of Yb-doped fibres. In the numerical example we calculated the maximum possible efficiency as 0.73 and the laser we designed matched this figure with complete uni-directionality.

The flow chart below summarises the laser design algorithm.

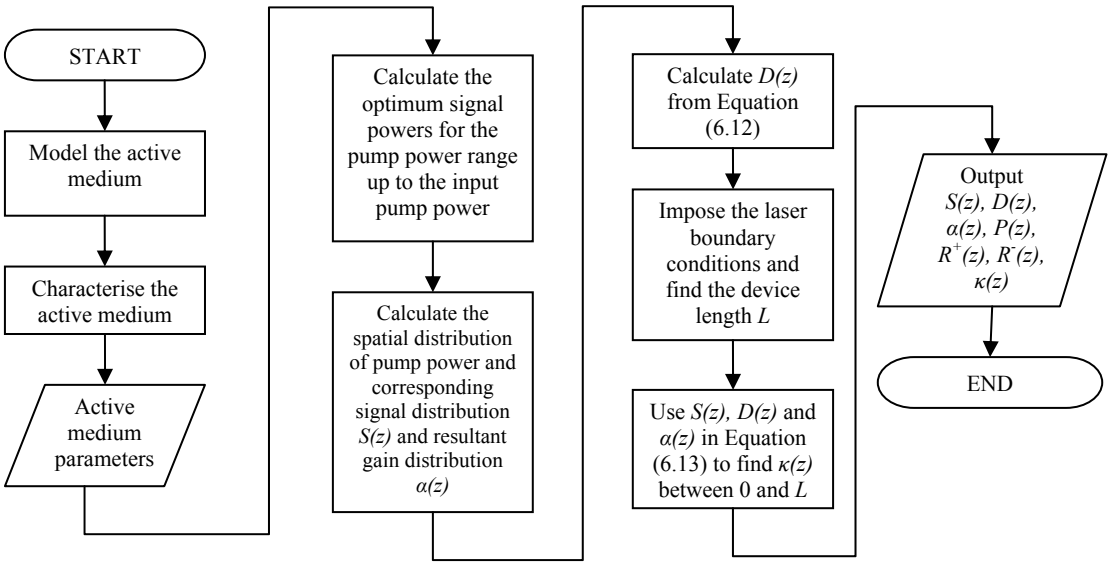

Figure 6-25 Flow chart of the laser design method

As a numerical example we studied the laser design in a Yb doped fibre. We calculated the maximum possible efficiency as 0.73 and the laser we designed matched this figure with complete uni-directionality.

The method is based on the steady-state operation of CW linear cavities, and it is applicable to any pumping scheme and active medium, in which a grating can be incorporated. The input to the design method is the model of the active medium hence its accuracy is critical for achieving the fundamental efficiency limits. We address the various issues related to the active medium parameters in the next chapter. The practical limits in implementing the new method are set by the accuracy of the active medium model and the particulars of the grating writing technique.

6.7. References

[1] G. Morthier and R. Baets, "Design of Index-Coupled DFB Lasers with Reduced Longitudinal Spatial Hole Burning," *Journal of Lightwave Technology*, vol. 9, no. 10, pp. 1305-1313, 1991.

[2] A. Ghatak and K. Thyagarajan, "Appendix F : Derivation of coupled-mode equations for periodic coupling," in *Introduction to Fiber Optics*. Cambridge, UK: Cambridge University Press, 1998, pp. 547-551.

[3] H. M. Pask, R. J. Carman, D. C. Hanna, A. C. Tropper, C. J. Mackechnie, P. R. Barber, and J. M. Dawes, "Ytterbium-Doped Silica Fiber Lasers: Versatile Sources for the 1-1.2 um Region," *Ieee Journal of Selected Topics in Quantum Electronics*, vol. 1, no. 1, pp. 2-13, 1995.

[4] I. Kelson and A. A. Hardy, "Strongly Pumped Fiber Lasers," *Ieee Journal of Quantum Electronics*, vol. 34, no. 9, pp. 1570-1577, 1998.

Chapter 7 Ultimate Efficiency Design in Er/Yb Co-Doped Fibre

7.1. Theoretical Preparation

7.1.1. Investigation of the Active Medium

In this chapter we will apply the new design method to the Er/Yb co-doped fibre we characterised and modelled in Chapter 4. The detailed model of the medium allows us to calculate the optimum signal and gain values for the maximum efficiency. We will design the laser for a pumping wavelength of 976 nm and an operating wavelength of 1552 nm. Figure 7-1(a) and (b) show the variation of the generated signal and absorbed pump power as a function of signal power for a fixed pump power of 200 mW. In this 3-level system, the signal is generated by the erbium ions and the pump is mainly absorbed by the ytterbium ions. For a fixed pump power the limited number of erbium ions leads to the saturation of the signal generation with increasing signal power, as can clearly be seen from Figure 7-1(a) (dashed line). However, the signal loss due to a constant background loss term is a linearly increasing function of signal power (dotted line), hence the net generated signal (solid curve) begins to drop once a certain signal power is exceeded. Similarly the pump absorption saturates with increasing signal power due to the finite number of ions. Here however since the pump power is fixed at 200 mW, the contribution of the constant loss term due to lifetime quenching of ytterbium ions is not affected by the signal power (dotted line). Now if we divide the net generated signal curve by the total absorbed pump power curve then we obtain the pump-to-signal conversion efficiency curve, as a function of signal power, as shown in Figure 7-1(c) and observe that for this given pump power of 200 mW, the signal power of 2.8 W is the optimum value yielding the largest possible efficiency of 0.31.

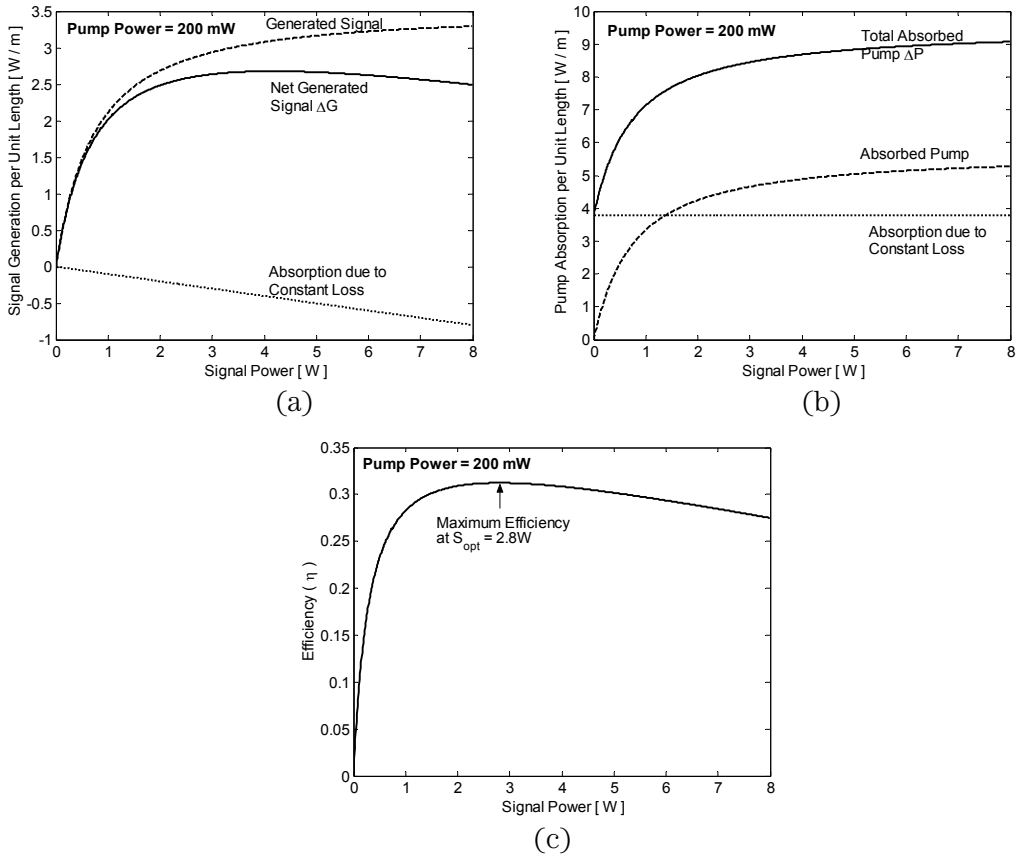

Figure 7-1 (a) Signal generation and absorption (b) Breakdown of pump power absorption (c) Pump-to-signal conversion efficiency. All curves are calculated for pump power = 200 mW as functions of signal power. Fibre parameters are given in Table 4-2.

In the same fashion we can calculate the optimum signal power and corresponding maximum possible conversion efficiency for other pump powers. Figure 7-2(a) shows the results of this analysis for pump powers between 0 and 200 mW. Figure 7-2(b) shows the generated signal and absorbed pump powers at the optimum signal power values. We see that the signal generation (solid line) saturates much faster than the pump absorption (dotted line). This is due to the fact that the signal generators, that is erbium ions, have a concentration of only ~1/10 of the main pump absorbers, that is ytterbium ions. The signal generation in erbium ions saturates quickly whereas the pump absorption, and hence the related pump loss in ytterbium ions increases without significant saturation with increasing pump power. The result appears as a drop in the maximum possible conversion efficiency with increasing pump power (c.f. dashed line Figure 7-2(a)).

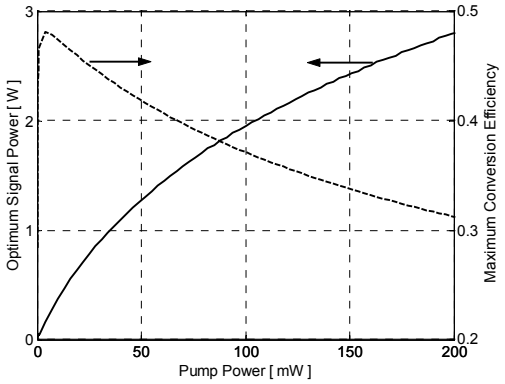

(a)

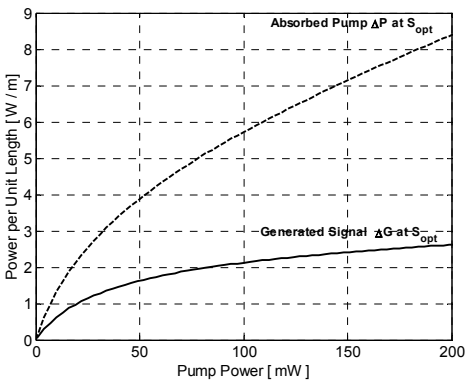

(b)

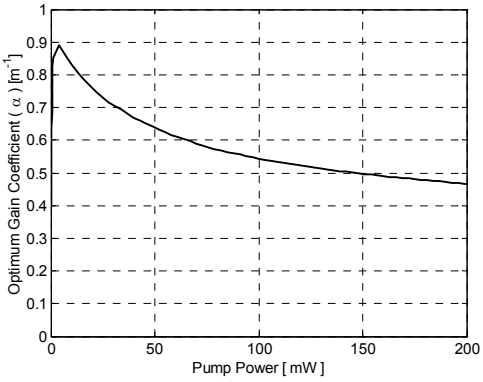

(c)

Figure 7-2 (a) Optimum signal power (solid line) corresponding to pump power up to 200 mW and resultant maximum possible conversion efficiency (dashed line) (b) Generated signal (solid line) and absorbed pump powers (dashed line) when optimum signal power is used (c) Field gain coefficient corresponding to optimum signal powers.

The optimum signal power and the resultant signal generation give the corresponding optimum field gain coefficient at different pump powers as shown in Figure 7-2(c).

7.1.2. Effects of Active Medium Properties

Figure 7-2(a) provides the extremely valuable information about the fundamental efficiency limit that one can achieve from the given medium. For example, if we take a single point of the maximum efficiency-pump power curve (dashed line), say for 200 mW pump power, we see that the maximum conversion from pump-to-signal would be 0.31, if the pump power is absorbed totally by a very large number of ions. However, in a real case pump absorption will be gradual along the fibre hence, the pump power will decrease and therefore the maximum possible efficiency rate will increase. For example if the launched pump power from one end is 200 mW and it is gradually absorbed completely, then the maximum conversion efficiency will be the average of the dashed curve between 0 and 200 mW, which is 0.38 and the maximum possible signal would be 76 mW.

The fundamental limit of the laser efficiency is set by the active medium and the pumping scheme used. If the medium were a lossless ideal medium then the fundamental limit would be the quantum limit set by the signal and pump wavelengths, which in this particular case is 0.63, independent of pump power. However in this realistic Er/Yb co-doped medium certain loss mechanisms are present. Figure 7-3(a) shows the effects of various loss mechanisms on the maximum possible efficiency.

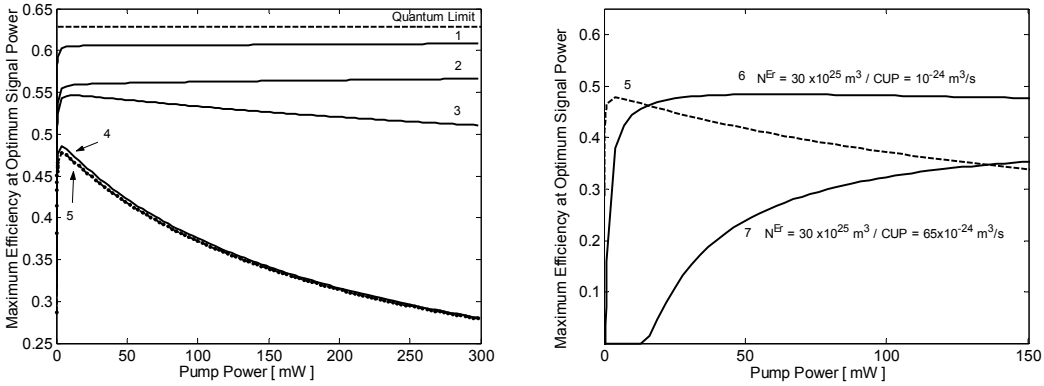

(a) (b)

Figure 7-3 (a) Maximum efficiency curves with the introduction of additional loss mechanisms. Refer to the main text for the details (b) Maximum efficiency curves with and without co-operative up-conversion (CUP).

The dashed flat line shows the quantum limit for the given pump and signal wavelengths. Curve (1) shows the maximum possible conversion efficiency in a fibre with N^{Er} = 3 x 10^{25} m^3 and N^{Yb} = 34 x 10^{25} m^3 without any loss mechanisms present. The deviation between curve (1) and the quantum limit is due to the finite excited-state life-time of Er and Yb ions and conversion of energy to other wavelengths due to spontaneous emission. Curve (2) shows the result of adding constant background loss of 0.65 dB/m at the signal wavelength. Then we introduce lifetime quenching for 1% of the total Yb ions and obtain Curve (3). The unsaturable pump loss causes the efficiency to drop after a maximum value at small pump powers. Then we increase the percentage of the quenched Yb ions from 1 to 11 and obtain Curve (4). Finally we introduce excited-state-absorption (ESA) and cooperative up-conversion (CUP) terms with magnitudes 10^{-27} m^2 and 10^{-24} m^3/s respectively to obtain the original active medium parameters used in Chapter 4 and obtain Curve (5). In this particular Er/Yb co-doped fibre the defining factor for the ultimate efficiency is therefore found to be the life-time quenching of the Yb ions. It can be proposed that by increasing the Er concentration to levels comparable to the Yb concentration one can prevent early saturation of signal generation and prevent the maximum possible efficiency curve from falling.

Indeed when we increased the Er concentration by 10-fold to $30x10^{25}$ m^{-3} we obtained Curve (6) in Figure 7-3(b) which exhibits almost flat behaviour as expected. However, increasing Er concentration, in reality, is accompanied by the increasing cooperative up-conversion (CUP). This phenomenon is inversely proportional to the cube of the distance between the Er ions, therefore it increases rapidly with concentration. The function that decribes the CUP dependence on the ion separation varies from host to host, and ideally it should be investigated experimentally. However, in order to illustrate the effect of increasing CUP on the efficiency we will use the following linear approximation for large concentrations (> $5x10^{25}$ m^3) [1]:

$$CUP = 3.5x10^{-24} + 2.41x10^{-49}(N^{Er} - 4.4x10^{25}) \qquad (7.1)$$

When we increase the Er concentration by 10 fold therefore CUP conversion should increase from 10^{-24} m^3/s to $65x10^{-24}$ m^3/s and the resultant maximum efficiency possible is given by Curve (7) in Figure 7-3(b). We can see that although the larger Er concentration prevents the decrease of maximum efficiency with increasing pump power, the increased up-conversion term leads to a significantly smaller maximum efficiency. Hence, there is a trade-off between the saturation of signal generation and losses due to the up-conversion.

7.1.3. Spatial Distributions for Co-Pumping Scheme

Following the investigation of the given active medium and the calculation of the optimum signal and gain curves over the pump powers of interest we can proceed to the design of the maximum efficiency cavity. As the starting point for the design we assume that 200 mW of pump power is launched into the fibre from the left-hand side co-directionally as illustrated in Figure 7-4 below.

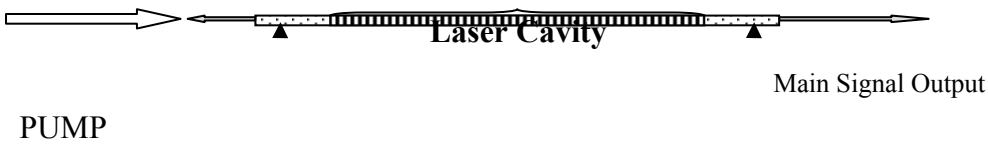

Figure 7-4 Illustration of co-pumping scheme.

In our design procedure we will also take production practicalities into account. For example, in practice an average of 4 mm-long doped fibre should be left before and after the laser cavity as a cleaving and splicing tolerance. This additional section of doped fibre has not inscribed grating and causes the actual pump power delivered to the laser cavity

to drop from 200 mW to 185 mW. Therefore at $z = 0$ (the entry point to the cavity), we take the pump power to be 185 mW and design the cavity accordingly.

The pump power will be absorbed as it propagates through the fibre hence the maximum conversion efficiency will be the average value between 0 and 185 mW of the dashed curve in Figure 7-2(a). We calculate this value to be 0.39. At this maximum efficiency 185 mW pump power should provide 72 mW total output power at the signal wavelength of 1552 nm if complete pump absorption takes place.

For the second step in the design method we need to find the spatial distribution of the signal intensity with the proper laser boundary conditions. As we discussed previously we can set the left-hand side signal output power to be zero so that all the generated power leaves the cavity from the right-hand end, making the device completely unidirectional However, as shown before, this condition will require a perfect mirror to be butted with a grating maintaining a precise phase shift. Since splicing a mirror with a grating would be very difficult in practice, we allow a smoother change between the optimum signal value and a small left-hand output resulting in a condition that can be met by a grating (see Appendix B). In this particular case, we define this transition to be hyperbolic, i.e. of the form $S(z)=D_0\cosh(mz)$. As we discussed in Section 6.3.2. this particular type of signal distribution requires a constant apodisation profile with amplitude $\kappa = m/2$. The gain in the current fibre will not cause a significant deviation from the constant coupling coefficient. The maximum coupling coefficient that can be achieved in the fibre is limited by the photosensitivity of the fibre. We found that $m = 735$ m^{-1} can easily be achieved with the current fibre properties and the grating writing technology. This corresponds to an effective refractive index modulation $\Delta n = 1.8\text{x}10^{-4}$ for the Bragg wavelength = 1552 nm. We define the left-hand side output to be 1 mW and the hyperbolic increase rate as $m = 735$ m^{-1}. That is:

$$S(0) = 1mW \quad \text{and} \quad S_{transition}(z) = S(0)e^{735z} \tag{7.2}$$

The dashed curve in Figure 7-5 shows the defined hyperbolic transition. With this smoother increase we calculate the pump absorption and resultant pump distribution (shown with dotted curve) starting from 185 mW. Since we already know the optimum signal power for each pump power (see Figure 7-5 solid line) we can derive the optimum signal distribution corresponding to this pump distribution (shown with the solid curve). At the position z ≈ 11 mm, the hyperbolically increasing signal meets the optimum value for the pump power ≈ 125 mW and from this point on we define the signal distribution to follow the optimum value.

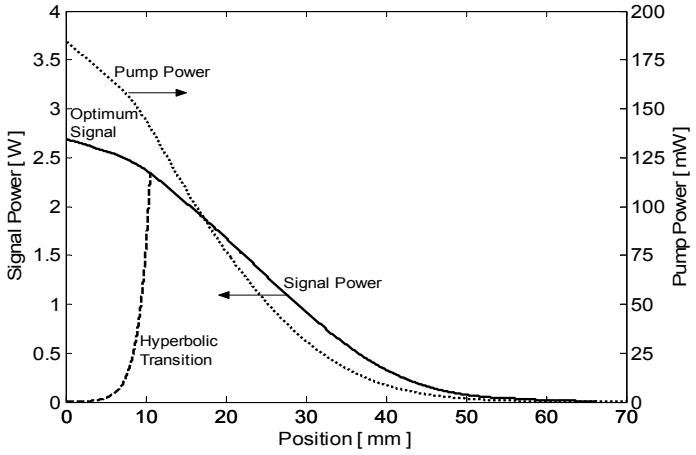

Figure 7-5 Defined signal distribution and pump power distribution (dotted) in the case of this distribution. Hyperbolic transition signal (dashed) in the shaded area reaches the optimum signal (solid) value at z = 11 mm.

Obviously, between z = 0 and 11 mm the signal power is not at the optimum value (c.f. the solid and the dashed line for $0 < z < 11$mm). Therefore, in this segment conversion efficiency will not be maximum. However, as stated before, this is not due to the design method but it is merely a limiting factor set by the production technique which favours a grating segment over splicing an external mirror. If the writing technique allows a very strong grating to be written then this exponentially (or any other fast varying) section can be shortened, and at the limit can be replaced by a mirror and then the entire cavity will be operating at the maximum efficiency.

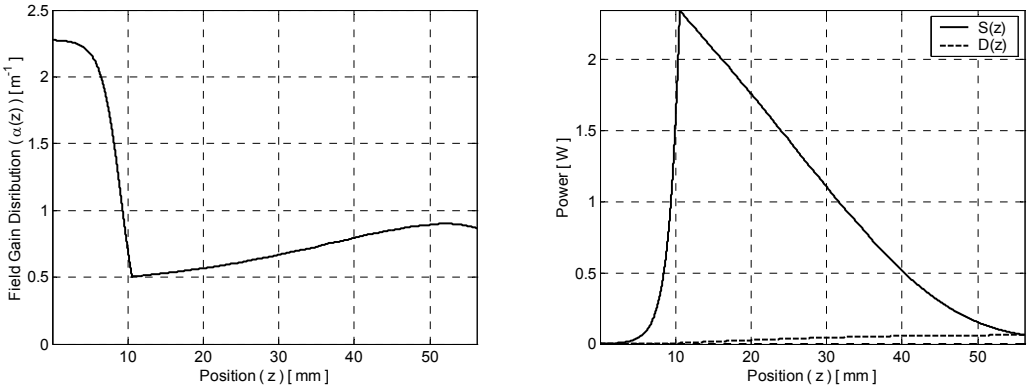

(a) (b)

Figure 7-6 (a) Gain distribution corresponding to the defined signal distribution with a hyperbolic increase up to z = 11 and optimum until z=56 mm (b) $S(z)$ and $D(z)$ between the two boundaries z=0 and z=L=56 mm

Now we know the pump and signal distributions and therefore we can easily calculate the gain distribution $\alpha(z)$ from the rate-equation of the active medium model as shown in Figure 7-6 (a). With known $S(z)$ and $\alpha(z)$ we use Equation (5.12) to calculate $D(z)$ and

find the position z=L=56 mm where the boundary condition $D(L) = S(L)$ is met as shown in Figure 7-6 (b).

We choose the grating period to be constant $\Lambda(z)$ =1552nm / $2n_0$ for matching the Bragg wavelength and signal wavelength, where n_0 is the effective refractive index of the fibre. Substituting $S(z)$, $D(z)$, $\alpha(z)$ and $\Lambda(z)$ in Equation (6.13) we calculate the coupling coefficient profile $\kappa(z)$ required for the signal distribution we defined.

Figure 7-7 (a) shows the derived coupling coefficient $\kappa(z)$ and Figure 7-7 (b) is the corresponding refractive index modulation $\Delta n(z)$ in the form of:

$$n = n_0 + \Delta n \cos(\phi(z)) \tag{7.3}$$

where Δn is the amplitude of modulation and ϕ is the phase of the sinusoidal grating. In this case Δn is related to κ by:

$$\kappa(z) = \frac{\Delta n(z)\pi}{\lambda} \tag{7.4}$$

and the sign change in κ is achieved by introducing a π shift in ϕ.

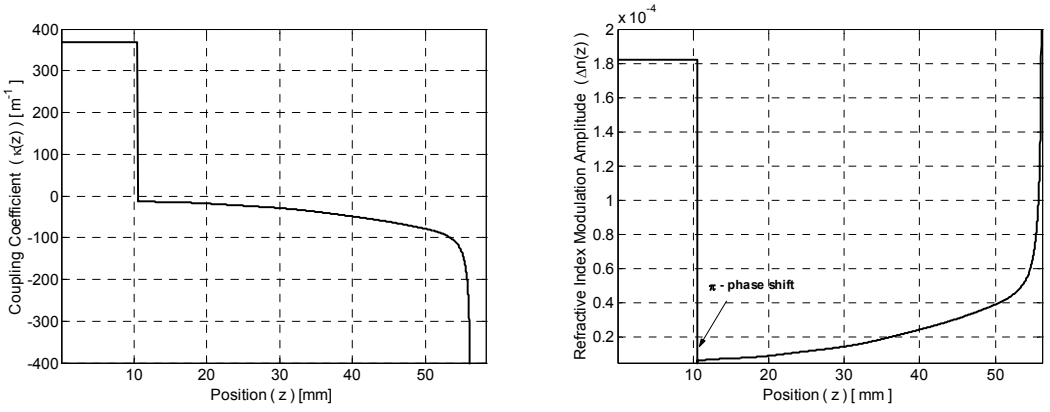

(a) (b)

Figure 7-7 (a) Coupling coefficient profile required for the defined signal distribution assuming no chirping. (b) Refractive index modulation amplitude profile corresponding to the calculated coupling coefficient profile in the case of a sinusoidal refractive index grating.

The flat section in Figure 7-7 (a) between z = 0 and 11 mm is the grating segment required for the hyperbolic increase in the signal power while the rest of the grating maintains the signal distribution at its optimum value until the right-end boundary condition is met at z = 56 mm. At this position, the signal power is equal to the forward

signal, which is the output power from this end and it is calculated to be 61 mW. Therefore, the total output power from this cavity including the defined 1 mW backward output power is 62 mW. The unabsorbed residual pump power is around 1 mW, therefore the total conversion from pump-to-signal is 0.33. Compared to the ultimate limit of 0.39, the 6% difference is due to the non-optimised hyperbolic transition segment of 11 mm.

Using the DFB laser simulation software based on the T-matrix method (see Section 3.2), we calculated the new design's power characteristics for pump powers up to 250 mW and compared it with the simulation of the standard optimised design, in Figure 7-8. In these simulations we included 4 mm-long segments before and after the laser cavity in order to be able to compare the experimental and theoretical results at a later stage.

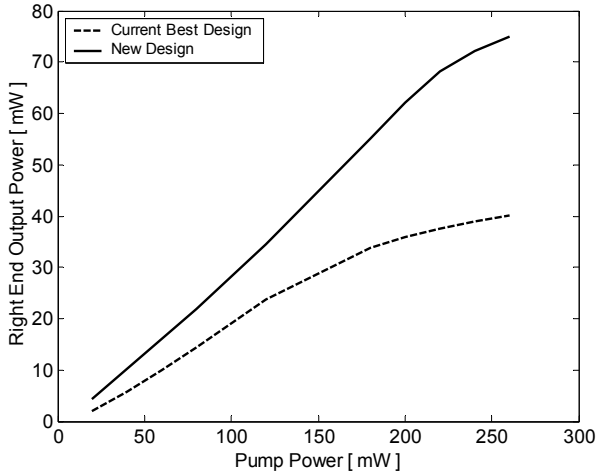

Figure 7-8 Theoretical comparison of output characteristics of the new design and the best uniform DFB laser. At the design pump power 200 mW, output power is increased by 64%.

The new design has dramatically larger output powers compared to the traditional design over the entire pump power range. For the optimisation pump power 200 mW (drops to 185 mW after the doped section) the simulation of the new design gives 61 mW output power, which, compared to the 37 mW output power of the traditional design, is a 64% larger. The simulation results confirm the validity of the design method. In addition to the increased efficiency, the new design also shows a very linear power characteristic up to the design power. However, for pump powers greater than the design power the structure becomes less efficient, as expected.

7.1.4. Longitudinal-Mode Stability

In addition to the better efficiency, the stable longitudinal-mode operation is essential for the overall performance of the lasers; therefore it is important to assess the modal stability of this new type of cavities.

The single longitudinal mode stability is a combined effect of the cavity design and the active medium: For instance, if the medium is not capable of providing high enough gain for the threshold of higher order modes then the laser will operate at the fundamental mode alone. Alternatively, if the cavity design results in spatial overlap of fundamental and higher order modes, then the fundamental mode will dominate over the other by extracting power, and again single mode operation will be sustained. Now we will examine and compare the modal stability of the new design to the standard design by considering a generic active medium with a constant gain distribution. We simulate the new and classic designs for the threshold gains, as discussed in Section 3.2.2 and calculate the signal distributions at the threshold of the fundamental and the 2nd order mode.

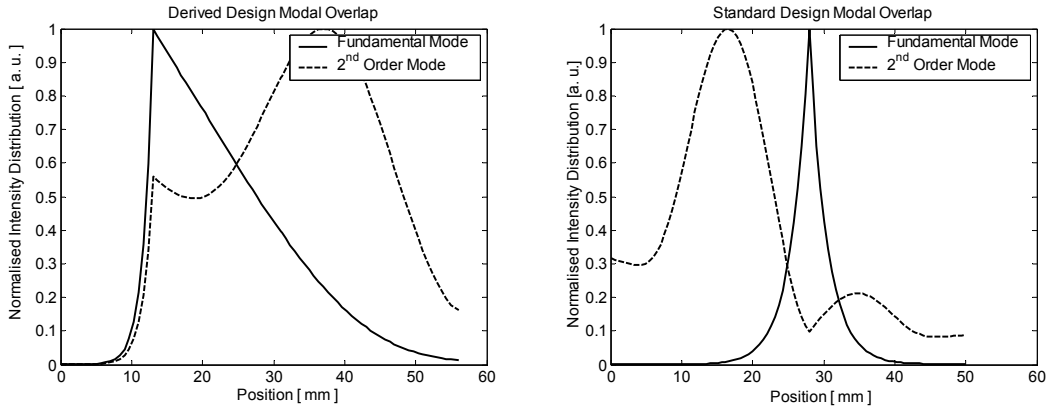

(a) (b)

Figure 7-9 Spatial overlap of fundamental and 2nd longitudinal modes (a) In the new design (b) In the standard design. Increased overlap in the new design contributes to the modal stability.

The threshold gain of the fundamental mode in the new design is found to be 0.5 m^{-1}, slightly larger then the threshold gain, 0.3 m^{-1}, of the standard design. The gain margin between the fundamental mode and the higher order mode is found to be 3 m^{-1} in the new design and 10.5 m^{-1} in the standard design. From the gain margin point of view the new design has a poorer separation between the two modes, however the threshold gain required for the higher order mode is still larger than the maximum available gain (~2.5 m^{-1}) in this particular medium. In addition to this sufficiently large gain required for the 2nd order mode the comparison of the signal distributions inside the two cavities (Figure 7-9 (a) and (b)) shows a greater overlap between longitudinal modes in the case of the new design.

In the new design, the fundamental mode spreads out more and fills the cavity better compared to the standard design. This causes the gain to be saturated by the fundamental mode, not leaving enough gain for the higher order mode to start lasing.

Therefore this much better overlap between two longitudinal modes assures the single mode stability in the new design.

7.1.5. Chirped Design

So far in designing maximum efficiency DFB cavities we have considered unchirped gratings (i.e. $\Lambda(z) = \Lambda_0 = \lambda_B / (2n_0)$) which makes the cosine term in Equation (6.13) equal to 1. However, this is rather arbitrary choice which was made without much justification. In the remaining of this section, we consider an optimum efficiency design based on a linearly chirped grating, i.e. $\Lambda(z) = \Lambda_0 + \Lambda_1(z - L/2)$, where $\Lambda_1 / \Lambda_0 = 1.4\text{x}10^{-4}$. Starting from the same optimum signal distribution ($S_{opt}(z)$) and gain distribution ($\alpha(z)$), shown in Figure 7-5 we have calculated the new required refractive index modulation corresponding to the chirped grating. The result is shown in Figure 7-10(a) and it is compared to the apodization profile of the previous unchirped case.

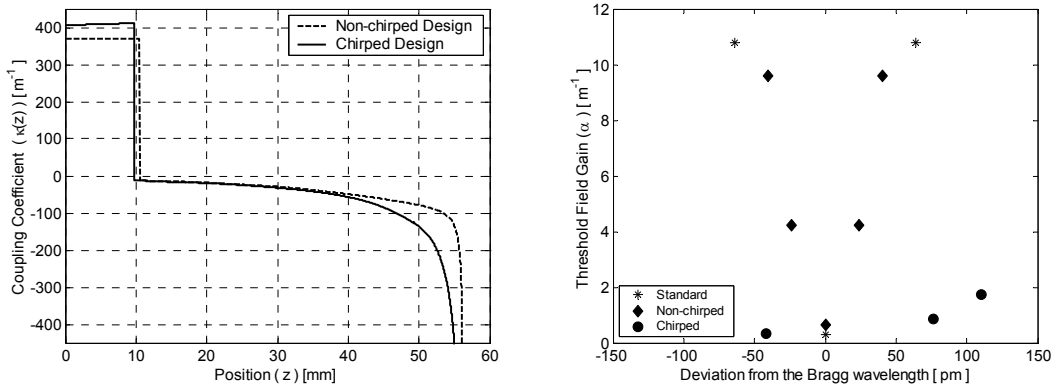

(a) (b)

Figure 7-10 (a) Comparison of apodisation profiles with (solid line) and without (dashed line) the chirp profile. (b) Threshold gains for the fundamental and higher order longitudinal modes of standard optimised (star), non-chirped maximum efficiency (diamond) and chirped maximum efficiency (circle) cavities.

It is quite straight forward to show from Equation (6.13) that for the same $S_{opt}(z)$ and (z) the two profiles are related by

$$\kappa_2(z) = \kappa_1(z)\left\{\cos\left[\Gamma(z)\right]\right\}^{-1} \tag{7.5}$$

where $\Gamma(z)$ defined as in Equation (6.4). Therefore, any additional chirp results in an increased coupling coefficient. Physically, this due to the fact that chirping gradually detunes the grating, which in order to provide the same optical feedback has to be stronger.

Cavities with and without chirp have the same total length and they produce the same output power at the designed pump power which are set by the boundary conditions and the signal distribution. Although their efficiencies are identical the two cavities are dramatically different in terms of the longitudinal mode stability. Figure 7-10(b) compares the threshold gains required for the various longitudinal modes in the standard π-shifted DFB laser (star) and maximum efficiency cavities with (circled) and without (diamond) chirping. The standard optimized DFB laser and non-chirped maximum efficiency laser have symmetric higher order longitudinal modes with respect to the Bragg wavelength (1552 nm) at which the fundamental mode has a very small threshold gain. Both cavities show significantly large gain margins between the fundamental and higher order modes. The unchirped cavities lase at the Bragg wavelength, i.e. $\lambda_s = \lambda_B = 2n_0 \Lambda_0$, which is well controlled by the fixed grating period Λ_0. In the chirped optimised cavity, on the other hand, the lasing wavelength is a complex function of the grating strength, chirp rate and the position of the π phase-shift. As a result, the lasing wavelength of the fundamental mode is different to the central Bragg wavelength $\lambda_B = 2n_0 \Lambda_0$. In addition the gain margins with the higher order modes reduce significantly. All first three modes of the chirped cavity have threshold gains that are well in the range of the available gain in this medium. This shows that the chirped design is very susceptible to mode-hoping, therefore it should be avoided.

7.1.6. Alternative Pumping Schemes

We discussed the effects of the active medium properties on the fundamental limits of efficiency. Now we will consider the implications of the choice of pumping scheme on the efficiency.

Different Pump Powers

The cavity is derived for the optimum signal value which follows the pump power distribution, therefore different input pump powers lead to different cavities. Figure 7-11 (a) below compares designs for launched pump powers of 50, 100 and 200 mW, which result in 45, 90 and 185 mW delivered pump powers respectively. The smaller pump powers lead to shorter cavities, as one would expect to prevent re-absorption of the signal. Figure 7-11 (b) and (c) compares the RHS output powers and residual pump powers from each design respectively.

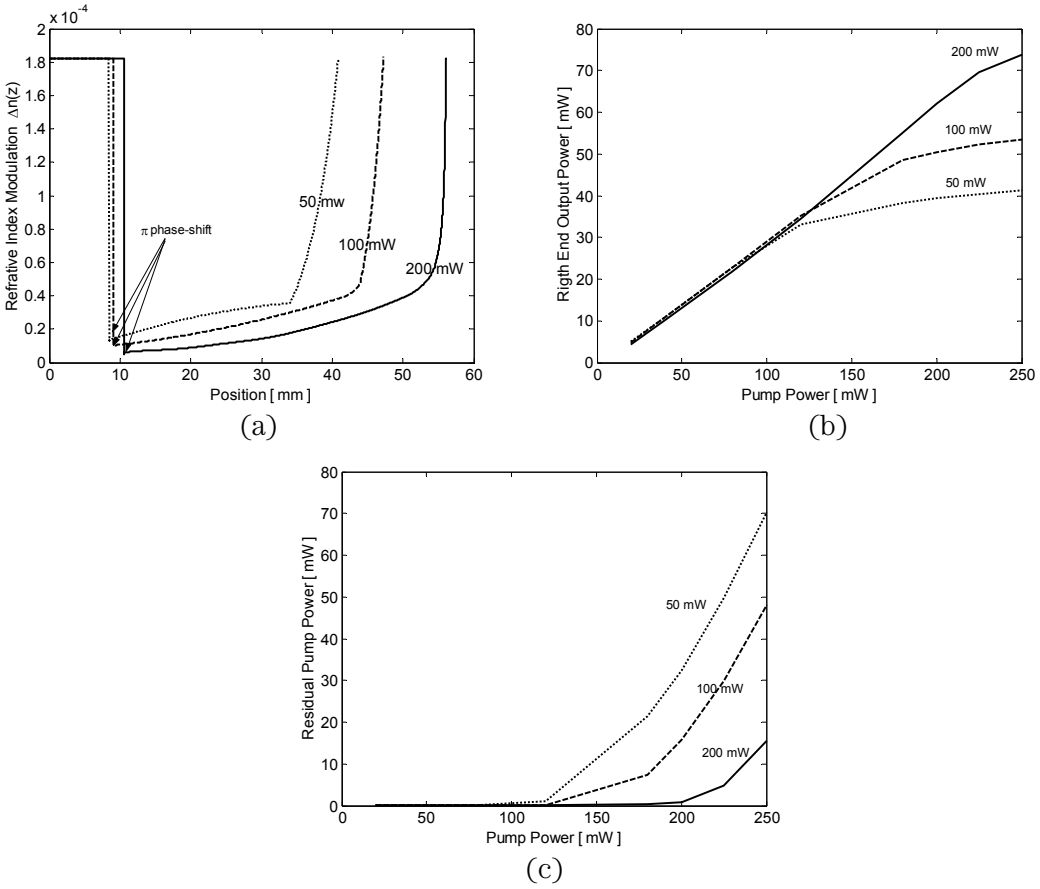

Figure 7-11 (a) Cavities designed for pump power of 50, 100 and 200 mW (b) Output characteristics and (c) Residual pump powers of the designs.

At the design powers the efficiencies are 0.38, 0.37 and 0.33 in the order of increasing pump power. This decreasing efficiency with larger pump power is also expected from the maximum efficiency curve in Figure 7-2(a) (dashed line) since larger pump powers result in smaller maximum efficiencies due to the increased pump loss because of the life-time quenched Yb ions. Each design provides linear output characteristics up to the design pump power and saturation is observed at pump powers exceeding the design value. Saturation also leads to the increased unabsorbed pump power beyond the design power.

Figure 7-12(a) shows the output power from the derived cavities for various pump powers (solid) line. The deviation from the fundamental limit (dotted line) is due to the presence of the front un-optimized transition region. If the grating writing limits can be increased then this un-optimized region can be shortened and the ultimate efficiency limit can be achieved practically by the presented design method. Figure 7-12 (b) shows the required DFB length as a function of pump power.

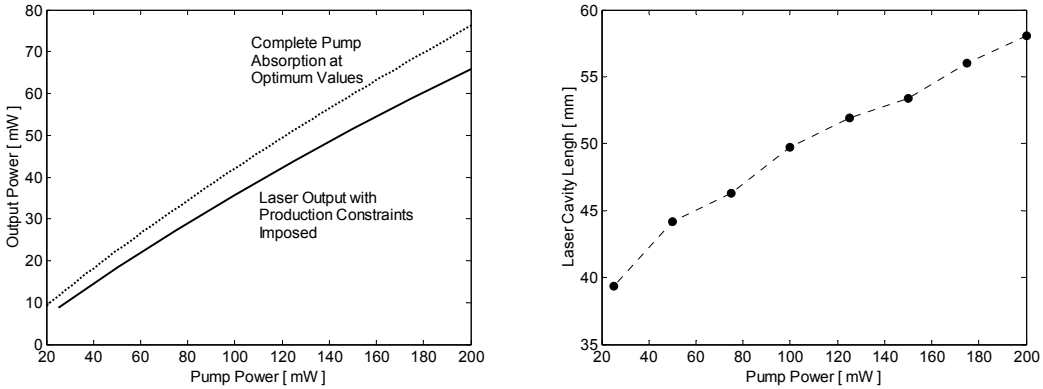

Figure 7-12 (a) Output powers from the derived cavities for various pump powers including the grating production limits (b) Length of the derived cavity as a function of pump power.

Counter Pumping

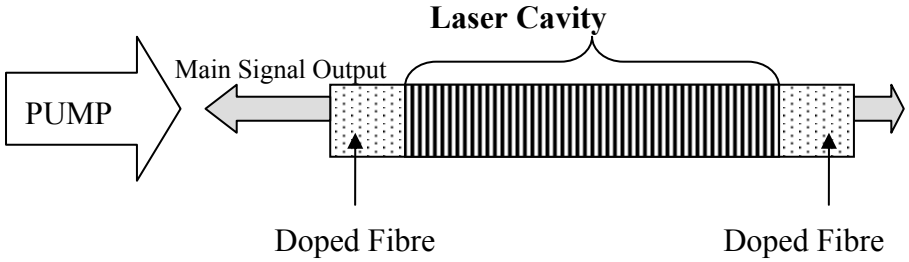

Figure 7-13 Illustration of the counter-pumping scheme.

Until now, we have assumed that the pump power was delivered in a co-directional manner. An alternative to this type of pumping is the counter-pumping scheme illustrated in Figure 7-13. In this scheme the main signal exits the cavity in the opposite direction to the delivered pump power.

In theory the co- and counter pumped designs should have identical efficiencies since both will have the same pump power delivered at z = 0 and both will exhibit the same optimum signal distribution. The only difference will be at the boundaries: At the LHS the counter-directional output power should be allowed to leave the cavity and at the RHS the co-directional power should drop to zero. However, if, for practical reasons, we allow a short transition region over which the signal increases from the counter directional output power to the optimum value, then the co- and counter pumped designs will have different efficiencies due to the different length of this transition segments, as will be explained below.

From Figure 7-2(a) we know that the average value of the maximum conversion efficiency for pump powers between 0 and 185 mW is 0.39 and the maximum generated power can be about 72 mW. Therefore, LHS output power can be 72 mW maximum if

there were no production restrictions for the grating. However, we will need to use a transition segment over which the signal will be sub-optimal hence the overall generated signal will be less then maximum. For this reason we need to define the LHS output power less then 72 mW. If we keep the same m parameter (735 m^{-1}) for the $\cosh(mz)$ transition (solid line in the shaded area of Figure 7-14 (a)) as in the case of co-directional design we found 67 mW LHS output power to be the upper limit.

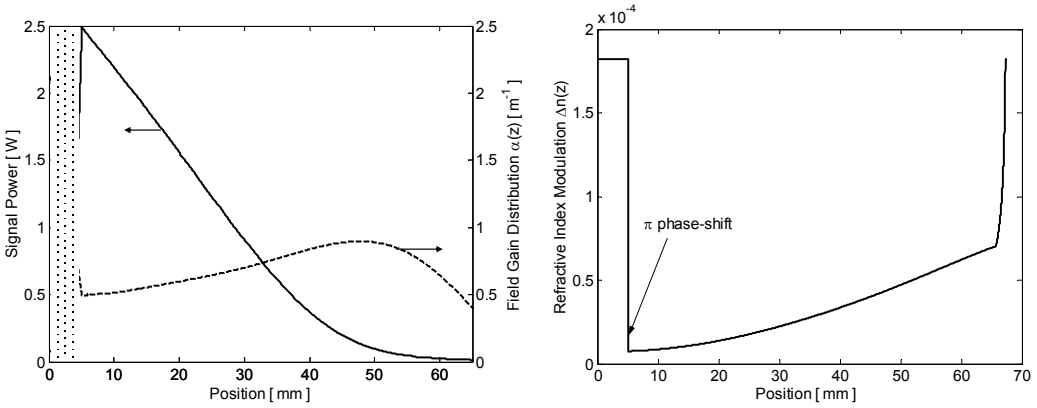

(a) (b)

Figure 7-14 (a) The signal (solid line) and the gain (dashed line) distributions for counter-pumping. Shaded area indicates the transition region from the output power to the optimum value. (b) Required refractive index modulation profile.

The design procedure is identical to the case of the co-pumped design. However in the co-pumped design we defined the left output power to be 1 mW and an 11 mm-long segment was needed to increase the signal from 1 mW to the optimum value ~ 2.5 W (c.f. Figure 7-5). In the counter-pumped design we define the LHS output power to be 67 mW and the length of the transition region needed is only 5 mm. The non-optimised transition region is halved in the counter pumped design and therefore more of the cavity is operating at the maximum efficiency limit and as a result, the overall efficiency is larger. As a matter of fact, the co-pumped design has a total conversion efficiency of 0.33 and the counter-pumped design has 0.36, while the fundamental limit is 0.39. Following the design steps described in Chapter 6 we calculate the required refractive index modulation as shown in Figure 7-14 (b). The cavity is longer than the co-pumped design by about 10 mm, and this extended grating on the RHS of the phase-shift causes the main output power to leave the cavity from the LHS as desired.

Bi-directional Pumping

Another alternative pumping scheme is the bi-directional configuration (bi-pumping) illustrated below. In this scheme the cavity is pumped from both ends with equal pump powers. Following the convention so far, if the total pump power is 200 mW then it is

divided into 100 mW for each end and the after 4 mm-long doped fibres, which are left as splicing tolerances, 90 mW of pump power is delivered to the cavity from each end.

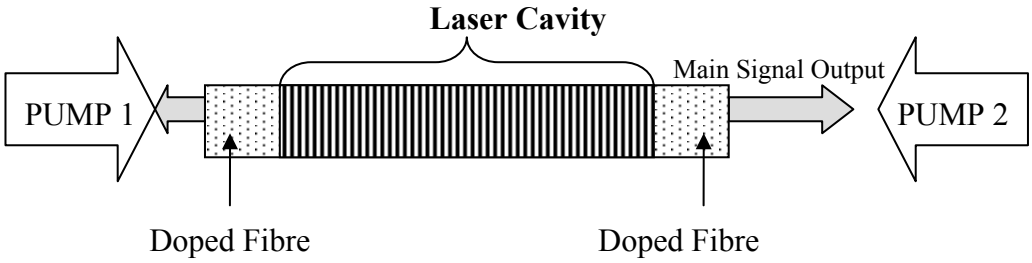

Figure 7-15 Illustration of bi-pumping scheme

Before starting the design procedure we can again use the maximum efficiency curve in Figure 7-2(a) in order to assess the expected efficiency of the cavity. If the pump powers propagating in both directions are almost completely absorbed then the total pump power inside the cavity be will be up to ~90 mW. The mean value of the maximum efficiency curve between 0 and 90 mW is 0.42 and, therefore, for a total of 180 mW pump power delivered bi-directionally, the maximum possible total output power, is 75 mW, which is larger than both the co- and counter-pumping schemes. But again when we introduce the required smooth transition regions we will deviate from this ultimate value. In the case of bi-directional pumping we will need two transition segments at both ends since the output powers will be different from the optimum signal powers (See Appendix B, Figure B-4) corresponding to the input pump powers.

Figure 7-16 (a) shows the distribution of the two pump powers and the total pump power when the transitional signal powers are present towards the ends of the cavity and the optimum signal distribution is sustained in between. Figure 7-16 (b) shows this signal distribution and the corresponding gain distribution.

With this information we employ the developed grating design method to find the required cavity. The result is shown in Figure 7-16 (c). One striking difference between this design and the two previous ones is the presence of 3 π phase-shifts. These phase shifts are associated with the change of the signal slope at the corresponding positions as shown in Figure 7-16 (b). The RHS output power of this cavity, when 180 mW pump power is delivered, is found to be 70 mW.

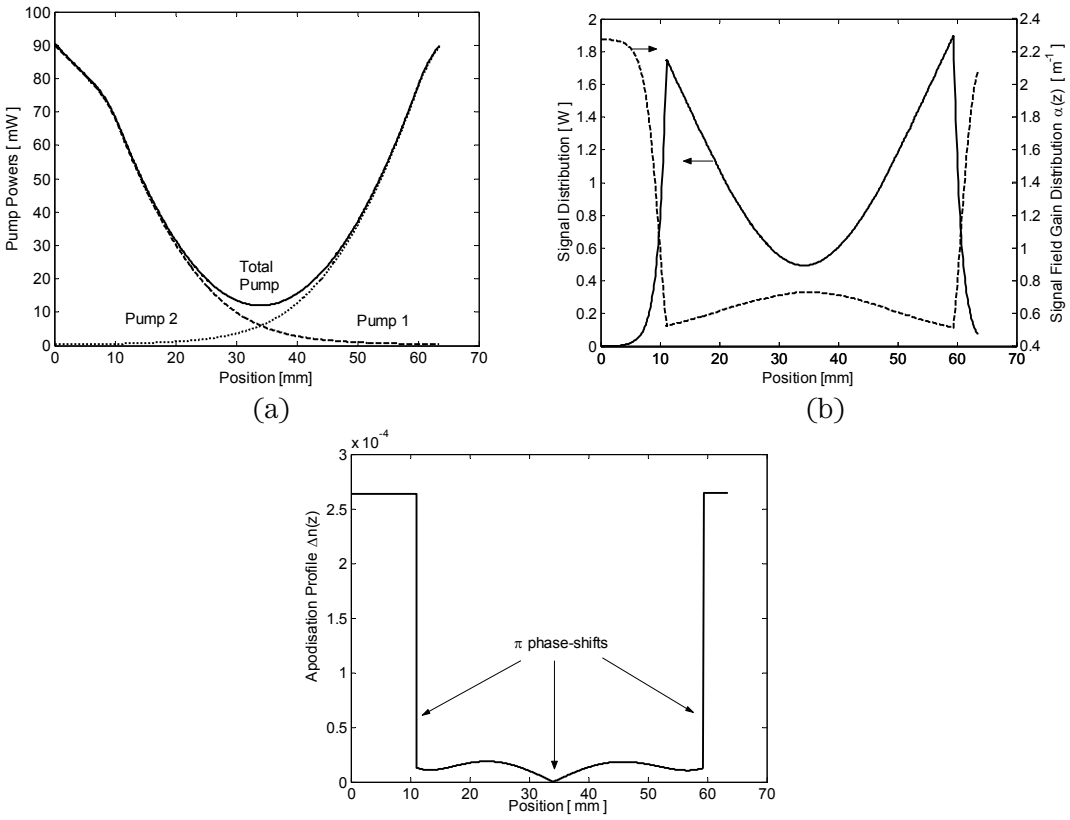

Figure 7-16 (a) Pump power distribution in the bi-directional pumping scheme. (b) The signal (solid line) and the gain (dashed line) distributions defined for the maximum efficiency including the transition stages. (c) The required apodisation profile.

Finally we compare all designs we presented so far in terms of their input-output power characteristics. We use the same pump source with a wavelength drift with increasing power (see Figure 4-12 (b)) and we include 4 mm-long doped fibre segments before and after the grating. These features are included for a realistic simulation of the practical setup (see Chapter 4).

The main cavity parameters of the designs we investigated in the Er/Yb co-doped fibre are summarised below in Table 7-1. In all cases the signal wavelength is 1552 nm. In the case of bi-pumping we divide the total power equally between the two ends.

	Total Length [mm]	Transition Region [mm]	Number of π phase-shifts	Launched / Delivered Pump Power [mW]	Unwanted output signal [mW]
Co-pumped	56	11	1	200 / 185	1
Counter-pumped	66	5	1	200 / 185	1
Bi-pumped	64	10 (LHS) 5 (RHS)	3	200 / 180	1
Step Apodised	50	Not applicable	1	200 / 185	4
Standard Optimised	50	Not applicable	1	200 / 185	4

Table 7-1 Summary of cavity features in the Er/Yb co-doped fibre.

Figure 7-17 shows the simulation results for pump powers up to 250 mW. All cavities are optimised for 200 mW total launched pump power. The lowest efficiency is observed when the DFB laser cavity is optimised by using the standard parametric approach. The step apodised design based on effective cavity length (Chapter 5) results in around 50% increase in the efficiency over this standard best design. The ultimate efficiency design method clearly shows its superiority over the other optimisation methods by providing 87 – 100% increase in the efficiency depending on the choice of the pumping scheme. In addition, all the new derived designs show more linear and more uni-directional power characteristics. For pump powers larger than the design value, as expected, the efficiency drops as the cavities become sub-optimal.

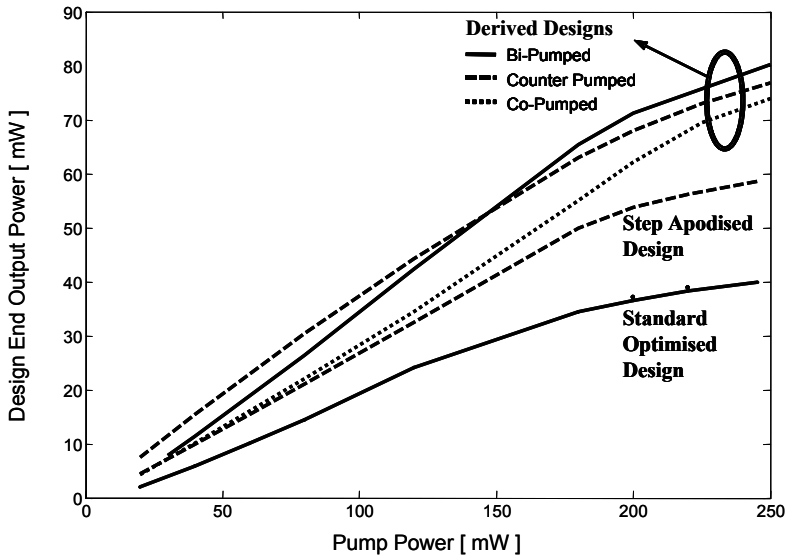

Figure 7-17 Theoretical comparison of output power characteristics of all the designs covered in the same Er/Yb co-doped fibre.

With the co-, counter- and bi-pumping schemes we covered all possible optical end-pumping configuration. A final comment can be made about uniform pumping, such as side-pumping or electrical pumping in semiconductor lasers, which, as opposed to the optical end-pumping schemes, can provide a constant pump power across the entire

cavity: If the pump power is constant then the corresponding optimum signal distribution will also be constant. In the case of a constant signal distribution the cavity will be similar to the one we discussed in Section 6.3.2 including the smooth transition regions. Again, although this cavity has a resemblance to DBR structures, strictly speaking, it would be a DFB laser due to the presence of the weak grating between the transition gratings in order to keep the signal constant at the optimum value.

7.2. Experimental Investigation

We experimentally investigated the maximum efficiency design in the Er/Yb co-doped fibre for co-pumping. We chose this pumping scheme because it allowed us to use the identical setup and calibrations we used for the experimental investigation of standard optimised and step apodised DFB lasers. By doing so, the experimental results are one-to-one comparable with the experimental results of these earlier optimisation approaches.

The optimum signal distribution is calculated by solving the rate equations defining the active medium, therefore the derivation of the cavity is critically affected by the active medium parameters. Discrepancies between the parameters of the model and exact values of the actual media can lead to derivation of an inaccurate cavity for the real medium. The complete and exact characterisation of an active medium, especially in the case of very complex transitions such as those present in the Er/Yb co-doped fibre, is an extremely challenging task and beyond the scope of this work. In any practical characterisation approach assumptions and fittings for certain parameters are inevitable. Even though the simulation results of Chapter 4 are in very good agreement with the experimental data, this does not guarantee the exactness of the assumed and fitted parameters, but it shows that the model matches the overall behaviour of a very complex system. However, it is possible to match the same characteristics with a similar but different set of parameters which may result in variations in the design for the maximum efficiency in practice. In this section we will investigate the effects of uncertainties in the active medium parameters on the cavity design before we proceed with the experimental application.

7.2.1. Effects of the Uncertainties in the Active Medium Model

All the parameters of the model, whether measured, fitted or assumed, have some degree of uncertainty; however not all of them have dramatic effects on the final design. By varying the parameters within the reported range in literature, we identified three of them to have critical effect on the cavity design. These are, namely, the total Yb

concentration, total Er concentrations and the energy transfer coefficient between Yb and Er ions. We can show the extent of their effects by deriving a series of cavities.

First, we double the assumed Yb ion concentration. The cavity derived for this new concentration results in the coupling coefficient profile shown with a dashed curve in the Figure 7-18 (a). Compared to the initial optimum design (solid curve), the new design is shorter with a very similar shape. Approximately, the profile appears to be scaled down in length and scaled up in amplitude after the transition segment. We then reduce the original Yb concentration by half, and find the optimum design to be as shown with the dotted curve on the same plot. Again the effect appears to be scaling of the length and the amplitude of the profile after the initial segment. But this time the length is scaled up, due to lower absorption, and the amplitude of the coupling coefficient is scaled down.

We follow the same procedure for the Er concentration. Doubling and halving the initial concentration result in the designs shown in Figure 7-18 (b) with dashed and dotted curves respectively.

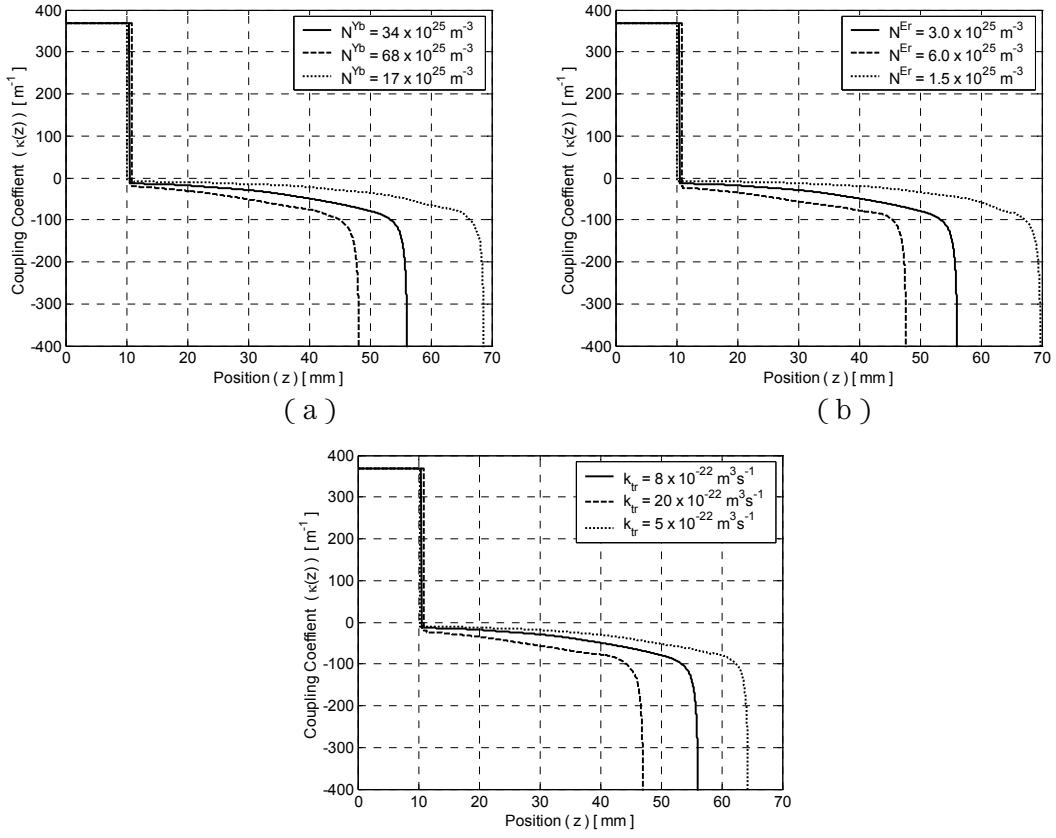

Figure 7-18 Effects of critical parameters on the optimum design (a) Assumed Yb concentration is doubled and halved (b) Assumed Er concentration is doubled and halved (c) Energy transfer coefficient between Er and Yb ions is changed to the lowest and largest values.

Finally we change the energy transfer coefficient to the maximum and minimum values that are most common in the literature. Figure 7-18 (c) compares the coupling coefficient profiles, with the maximum (dashed) and the minimum (dotted) transfer coefficient, to the original design (solid curve). In all of the cases above, the apodisation profiles have a strong resemblance to the original one, but they are scaled in length and amplitude.

From this investigation of the critical parameters we conclude that, although the modelling parameters may not be exact, if they are accurate enough, then the theoretical design can be scaled up or down in order to compensate for the uncertainty in these parameters. This deviation from the initial design will depend on the difference between the parameters' actual values and the values used in the model.

7.2.2. Results

We produced a number of lasers in which the theoretical length and the apodisation profile were scaled up and down. We achieved the best performance when the device was 45 mm long. We measured the absolute scaling of the apodisation profile of this device by using the grating characterisation method, as explained in Section 4.3. Compared to the initial theoretical design, the experimental apodisation profile was scaled up by 30% and length was scaled down by %20 (c.f. Figure 7-19).

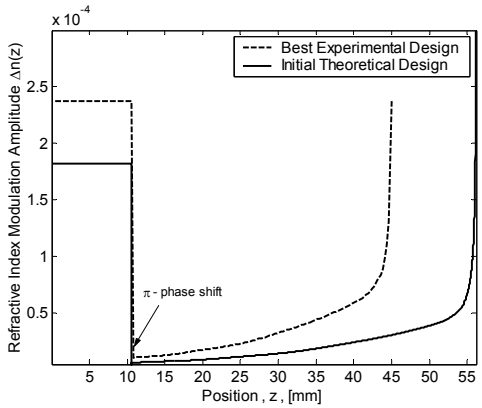

Figure 7-19 Theoretical design and the best operating experimental design. Experimental design is scaled in length and amplitude due to the inaccuracies of modelling parameters.

As the solid curve in Figure 7-19 shows, the design requires the refractive index modulation to increase steeply towards $z = L = 56$ mm. However, this is a very large modulation in the vicinity of $z = L$. When writing the gratings we limited the modulation to the constant value of the transition section. This causes a deviation from the initial design for a length of less than 1mm therefore we do not expect it to have a significant effect.

Figure 7-20(a) and (b) compares the theoretical (curves) and the experimental (error bars) output powers and residual pump powers of the 45mm-long new design and the parametrically optimised 50mm-long standard design.

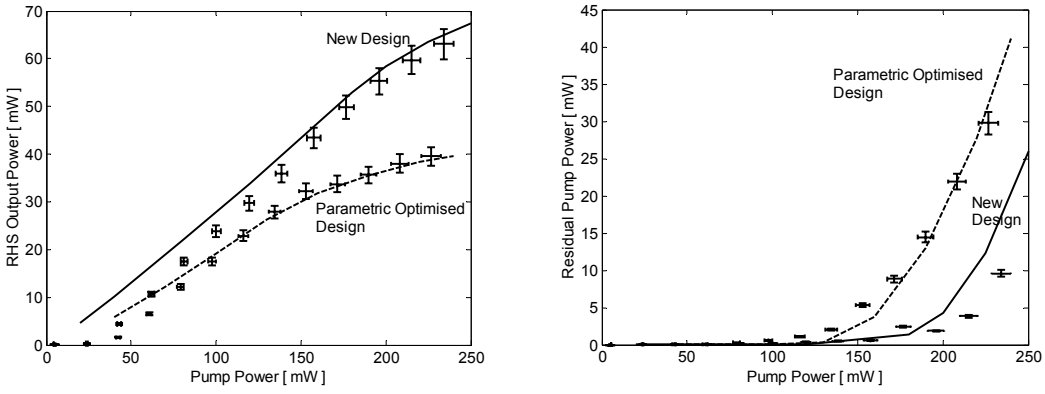

(a) (b)

Figure 7-20 Experimental (error bars) and simulation (curves) laser characteristics. (a) RHS output powers in co-pumping mode. (b) Residual pump powers from both design.

The new design has dramatically improved the efficiency and provided more linear power characteristics with a larger saturation value, as expected. At the design pump power of 200 mW, the output power is increased from 37 mW in the standard design to 58 mW in the new design, corresponding to a 57% increase. As a result of increased conversion efficiency from pump to signal the 10% shorter new design showed smaller residual pump powers compared to the standard design. The backward output power was less than 1 mW even for the largest pump power used and the new design is highly unidirectional (18 dB at 200 mW pump), as expected. The output spectrum of the laser when pumped with 200 mW pump power is measured as shown in Figure 7-21

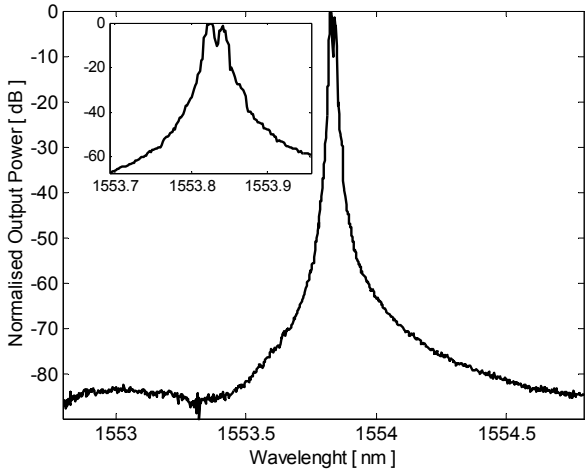

Figure 7-21 Normalised output spectrum of the new design. Observed peaks are two polarisation modes slightly offset due to birefringence of the fibre. Longitudinally new design is single mode and the side mode suppression is > 80 dB.

As the inset depicts, two peaks were observed in the spectrum. These peaks correspond to two polarisation modes due to the birefringence of the fibre, and the separation between the two polarisation modes was measured to be 16 pm. Simulation results showed that the 2nd order spatial mode would be 32 pm away from the fundamental mode. With the spectral resolution of 2 pm we could not see signs of the 2nd-order spatial mode. Therefore, the new design had stable single longitudinal mode operation at all the pump powers again as predicted.

7.3. Conclusions

Using the parameters of the characterisation and modelling study of Chapter 4, we determined the optimum signal powers for pump powers of interest. For a given initial pump power the maximum efficiency curve allowed us to define the ultimate efficiency limit that we can achieve in this particular fibre. We also investigated the effects of the various loss mechanisms on the ultimate efficiency limit. The lifetime quenching of ytterbium ions is found to be the main limiting parameter. This phenomenon results in the waste of the pump power almost without any saturation with increasing power, whereas the signal generation quickly saturates due to the smaller concentration of erbium ions. Increasing the Er concentration seemed to be a solution to this problem. However, increasing the Er concentration is accompanied with increasing co-operative up-conversion which causes the maximum possible efficiency to drop significantly. From the active medium spectroscopy point of view, the reduction of Yb life-time quenching and the optimum choice of Er concentration can increase the ultimate efficiency limit of the medium.

We also investigated the choice of pumping scheme on the efficiency. Bi-directional pumping is shown to be the best choice for this particular active medium since it leads to a smaller total pump power distribution throughout the cavity and results in a larger possible efficiency. In our design method we have also taken the production requirements into account. The upper limit for the grating coupling strength required us to allow a smooth but non-optimised signal power transition between the output powers and internal standing-wave power at the optimum value. This requirement made the counter-pumping scheme more efficient than the co-pumping scheme since a shorter transition segment would be sufficient.

Recognising the importance of the longitudinal-mode stability for the overall performance of lasers, we investigated the modal stability of the derived cavity for the co-pumping scheme without any chirp. The sufficiently large 2nd order threshold gain and much better spatial overlap between the fundamental and 2nd order mode compared to

the standard co-pumped design ensured stable single-mode operation in the new design. However when the cavity was designed with chirp the gain margins dropped significantly and the first three order modes had threshold gains that can be provided by the medium. Therefore, we concluded that chirp profiles should be avoided to prevent poor longitudinal mode stability.

The derived designs are critically based on the model parameters therefore uncertainties in the model values due to the measurement and characterisation limitations can result in divergence from the actual design. Therefore, before proceeding with the experimental study we investigated the effects of the uncertainties of the model parameters on the design and concluded that the variations in the critical parameters would result in the scaling of the cavity length and the apodisation profile. We confirmed the theoretical results experimentally in Er/Yb co-doped fibre. The 10% shorter new design provided a nearly 60% increase in the output power compared to the parametrically optimised standard design. The efficiency of the new design was measured to be 33%, and the deviation from the ultimate limit of 39% was a result of the fibre photosensitivity and the grating writing limitations. In addition to the larger output power, the new design showed lower threshold, more linear power characteristics, and was highly unidirectional, all agreeing very well with the simulation results.

The flow chart below gives an overview of the design method with its inputs and outputs. The inputs to the design algorithm are the parameters of the active medium and the pump source. For a given parameter set the method guarantees the ultimate efficiency. However errors and uncertainties in the active medium characterisation can lead to deviations between the theory and experiment and impose practical limits. Therefore, accurate characterisation and modelling are critical to achieve the fundamental efficiency limits.

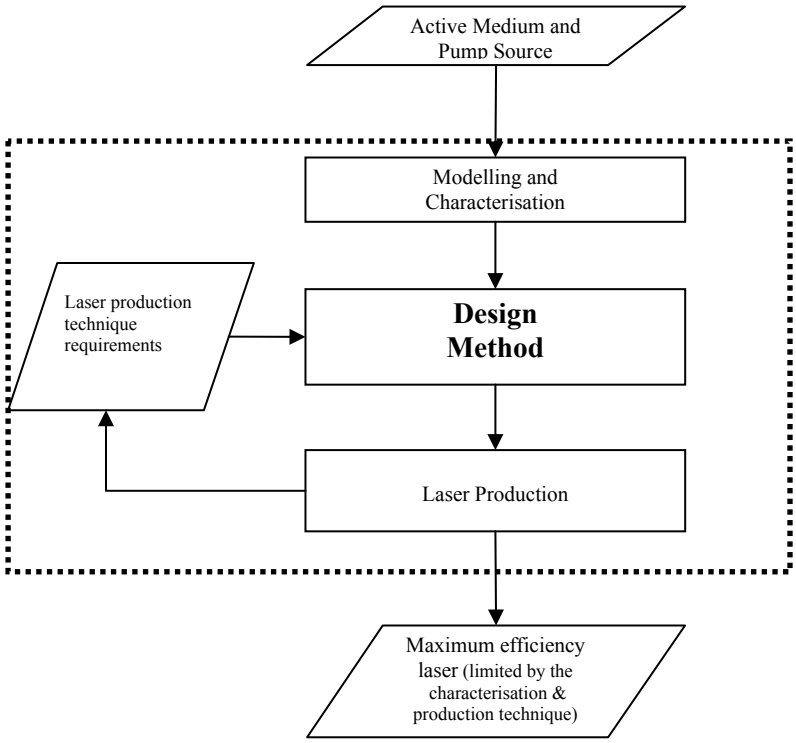

Figure 7-22 Flow chart of the production steps for the ultimate efficiency laser

The cavity obtained as the output of the design method requires a distributed feedback in order to tailor the signal distribution. Therefore, the grating writing technology also imposes practical limits; the maximum limit of the refractive index modulation that can be induced can be taken into account during the design process as we illustrated in the case of the photosensitive fibre. In addition to this limitation, the errors occurring during the grating writing process can also cause deviation from the ultimate limit.

To sum up; within the practical limits imposed by the active medium characteristics and fibre photosensitivity, the novel DFB laser design method guarantees the ultimate efficiency by deriving the required optimum cavity.

7.4. Reference

[1] M. Karasek, "Optimum Design of Er3+-Yb3+ Codoped Fibers for Large-Signal High-Pump-Power Applications," *IEEE Journal of Quantum Electronics*, vol. 33, no. 10, pp. 1699-1705, 1997.

Chapter 8 High Power Yb-Doped Fibre DFB Lasers with Ultimate Efficiency

8.1. Introduction

So far, we have considered ultimate efficiency designs using primarily 976 nm single-mode pumps of relatively low powers. These types of sources are widely used in telecom applications operating in the 1550 nm window. In this chapter we extend our investigation to alternative pumping configurations, including jacketed air-clad (JAC) source and cladding pumping, with high powers and alternative operating wavelengths, namely 976 nm and 1060 nm. These wavelengths are important for medical, industrial and aerospace applications.

8.2. High Power Standard Optimised Yb-Doped Fibre DFB Lasers

There has been a lack of high power, fibre-coupled, efficient pump sources operating in the wavelength range of 970-980 nm to pump Er and Yb doped fibres. However the recent developments in the jacketed air-clad (JAC) fibre technology opened the way for single-moded high power pump sources, both in laser and in ASE source configuration [1]. We recently reported the application of 1.5 W 976 nm JAC fibre ASE source for pumping a 5 cm-long standard asymmetric cavity Yb doped DFB fibre laser [2] to obtain output powers exceeding 400 mW at 1060 nm.

Figure 8-1 shows the setup we used for pumping the Yb doped DFB laser using the ytterbium doped JAC fibre as a high power ASE source. The 1.2 m long JAC fibre is pumped by a broadband multimode laser diode at 915nm. The JAC fibre, whose cross-section is shown in the inset, has a 10 µm diameter, 0.1 NA core at the centre of a 28 µm diameter inner cladding (NA ~0.5). The core was single mode with cut-off of 950 nm. The inner cladding is surrounded by an air-hole structure, raising the NA and therefore allowing a tighter 915 nm confinement. The end of the JAC fibre facing the pump diode was angle-cleaved in order to avoid any feedback which would have created instability in the JAC fiber source. An additional 1030nm filter was used to suppress unwanted 1030-1060nm emission of Yb ions in the JAC fibre. The output end of the JAC fiber is spliced to

a standard 980nm single mode fiber. The absence of feedback ensures that the JAC fiber operates in ASE mode.

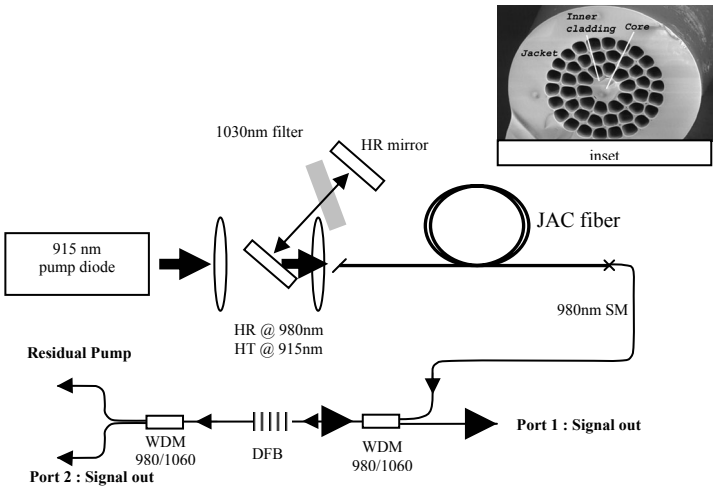

Figure 8-1 Experimental setup for application of JAC fibre as an ASE source for pumping Yb doped DFB lasers.

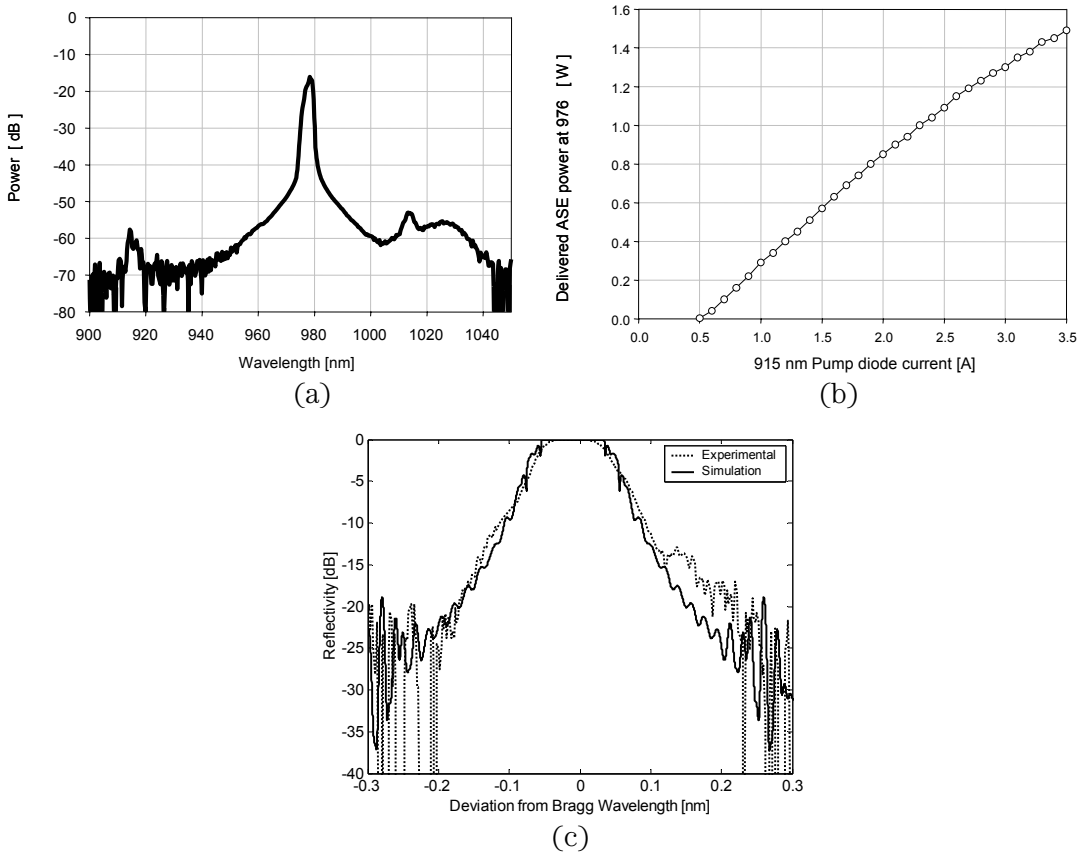

Figure 8-2 (a) JAC fibre ASE Pump Spectrum (b) 976 nm pump power delivered to the DFB laser (c) Experimental (dashed line) and simulation (solid lined) reflection spectrum of the DFB laser grating.

The characteristics of the JAC fibre are shown in Figure 8-2 (a) and (b). The ASE power is then launched through a 980 / 1060 nm coupler into the 5 cm-long standard

asymmetric cavity DFB fiber laser (see Figure 2-3) in the counter-pumping scheme. Figure 8-2 (c) shows the experimental reflection spectrum of the DFB laser grating obtained with 20 pm resolution and the best fit by simulation when a peak refractive index modulation of $1.5x10^{-4}$ is used. The birefringence of the fibre is estimated to be about 20 pm and the individual polarisation modes cannot be distinguished on an optical spectrum analyser (with a limiting resolution of 20 pm). This birefringence value is included in the theoretical reflection spectrum.

The core radius of the photosensitive aluminosilicate Yb doped fibre was 2.8 µm, NA was 0.14 and the cut-off wavelength was 1020 nm. Although 976 nm pump power was delivered in single mode by the JAC fibre the DFB laser was multi-moded at this wavelength with V = 2.47. We assume that 90% of the pump power remains in the LP01 mode and 10% in LP11 over the 5 cm-long device. This modal distribution gave us an effective overlap coefficient of 0.7 between the pump power and the active core. Using these values and the cross-section spectra provided by the manufacturer we estimated the Yb concentration to be $5.8x10^{25}$ m^{-3}. The best fit between the simulations and experimental data for the power characteristics is obtained when the background loss at both pump and signal wavelength was 0.009 dB/m, without any quenching, as Figure 8-3 shows below.

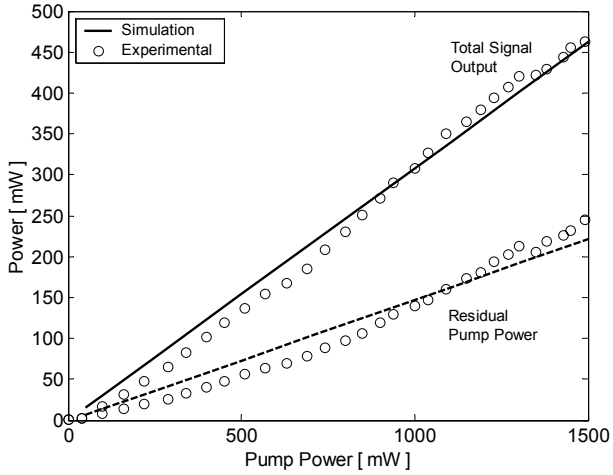

Figure 8-3 Experimental (circles) and simulation data for total output and residual pump power.

We used the Yb ion model and transitions described in Section 0with the parameters summarised in Table 8-1 below.

Parameter	*Value*
Total Yb Concentration	5.8×10^{25} m^{-3}
Pump Wavelength	**976 nm**
Absorption Cross-section at Pump Wavelength	18.2×10^{-25} m^2
Emission Cross-section at Pump wavelength	**18.2×10^{-25} m^2**
Signal Wavelength	1060 nm
Absorption Cross-section at Signal Wavelength	**8.23×10^{-27} m^2**
Emission Cross-section at Signal wavelength	4.45×10^{-25} m^2
Excited-state Life-time	**2 ms**
Background Loss	0.009 dB/m
Percent of Life-time Quenched Ions	**0**
Doping Radius	2.8 µm

Table 8-1 Parameters of the Yb doped fibre

The theory and the experimental data match well for the total output power and residual pump power. The small deviation from linearity is believed to be due to internally generated thermal effects, as will be discussed below.

Figure 8-4 shows (a) the variation of signal power coming out of the desired and undesired end and (b) their ratio (uni-directionality) as a function of pump power. The latter figure indicates a significant change in the uni-directionality.

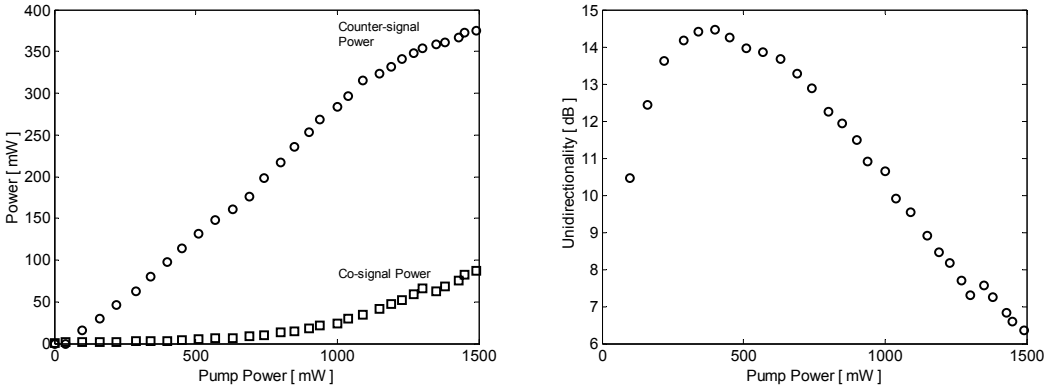

(a) (b)

Figure 8-4 (a) Output powers from individual ends of the DFB lasers (b) Variation of the uni-directionality with pump power.

Low power DFB fibre lasers have a typical uni-directionality figure around 20 dB[3] We believe the observed variation in the uni-directionality is due to the heating of the grating, especially near the phase-shift region, by conversion of absorbed pump power to heat through the quantum defect and background losses.

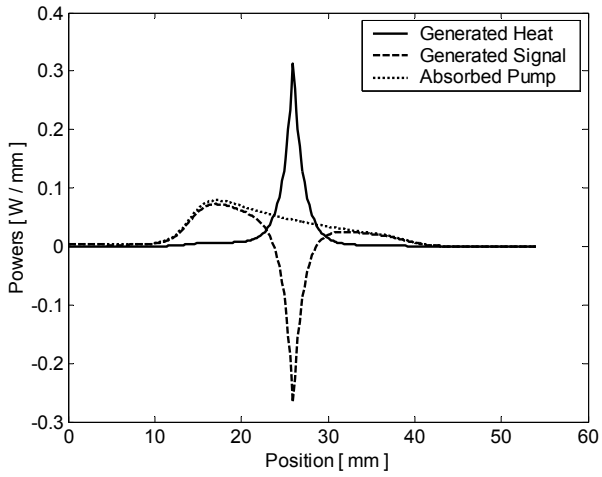

Figure 8-5 Signal generation, pump absorption and heat generation in the non-optimised standard DFB laser.

Figure 8-5 shows the locally generated signal, generated heat and absorbed pump power as functions of position in the non-optimised standard DFB laser design we used in the experiment. We calculate the generated heat easily by comparing the locally absorbed pump and locally generated signal by stimulated emission as well as by spontaneous emission using the rate equations. The negative value of the generated signal around phase-shift indicates the absorption of the signal due to the background loss. This is because the grating is too strong and causes an excessive signal build-up around the phase-shift. As a result the loss becomes larger then the stimulated emission, and the net effect is signal absorption. The combined effect of the signal loss, pump loss and the quantum defect is the large heat generation (up to 0.3 W / mm) around the phase-shift. The local heating can have two effects; (i) The non-uniform temperature distribution can lead to the expansion of the fibre, causing chirping in the grating period, which in turn results in the variation of the reflectivity of the gratings on each side of the phase-shift (ii) The expansion around a non-perfect π phase-shift can improve or further deteriorate the phase-shift. Both effects can change the laser output uni-directionality and can account for the observed behaviour.

8.3. Ultimate Efficiency Designs

We now apply the new method to design lasers with ultimate efficiency, using the same active medium parameters given in Table 8-1. We will consider core- and cladding-pumped geometries.

8.3.1. Design for core-pumped fibre

The JAC fibre source delivers the large pump power single-moded into the core of the Yb doped fibre in which we write the gratings. After determining the main parameters of the

model through the experiment and successful fitting, we can define the related optimum signal power and maximum possible efficiency. The solid line in Figure 8-6(a) shows the optimum signal powers corresponding to pump powers up to 1.5 W and the solid line in Figure 8-6(b) compares the maximum possible efficiency with the quantum limit for this pump and signal wavelength pair. Without the presence of any additional loss mechanisms other than the quantum defect and a small background loss, the maximum possible efficiency approaches the quantum limit in this particular fibre.

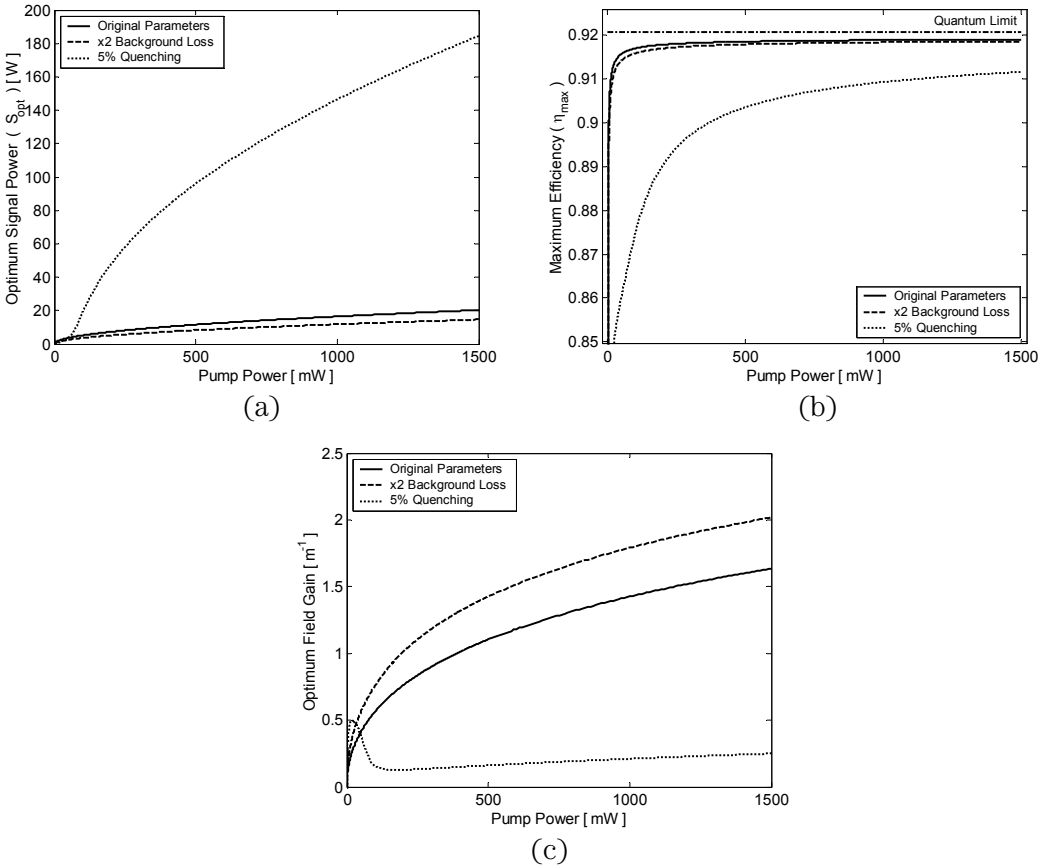

Figure 8-6 (a) Optimum signal powers for the original (solid line) medium, with doubled background loss (dashed line) and with 5% quenched ions (b) Corresponding maximum possible efficiencies (c) Corresponding optimum field gain values.

Doubling the background loss results in a lower optimum signal value (c.f. Figure 8-6 (a) dashed line). However its effect on the maximum efficiency is minimal (dashed line) in Figure 8-6, since it still has a very small value. (~ 0.01 dB/m).

Background loss affects both the pump and the signal powers. We also consider another type of loss originating from the Yb ion life-time quenching. This mechanism was shown experimentally in Chapter 4 to affect primarily the pump power in the form of an unsaturable loss. If we increase the ratio of the life-time quenched ions to 5% the optimum signal power drastically increases (dotted line in Figure 8-6(a)) while the

maximum possible efficiency limits drops significantly (dotted line in Figure 8-6(b). The optimum signal power is larger because in this case there are two absorption paths for the pump power: One through quenched ions by phonon emission and the other through ions with normal lifetimes by stimulated emission. The optimisation of conversion efficiency, therefore, requires the stimulated emission to be dominant over the phonon emission. The required large amount of stimulated emission requires the presence of larger signal powers. However, the signal power cannot be arbitrarily large because in that case the constant background loss will cause the efficiency to drop.

Finally Figure 8-6(c) shows the resultant optimum gain values for these three cases. The lower optimum signal value required in the case of increased background loss results in smaller stimulated emission for the same pump power. Hence a larger number of ions remain at the excited state. This causes the optimum gain value to be larger (dashed line) compared to the original fibre gain (solid line). Conversely, the larger optimum signal value required in the case of quenched ions manifests itself as a lower optimum gain value (dotted line) due to the increased stimulated emission. At low pump powers however, the loss due to the quenched ions become small and the optimum characteristics approach the case without any quenching.

Using the optimum signal and gain values we design the co-pumped all-grating cavities incorporating non-optimised smooth transition regions at LHS end as shown below.

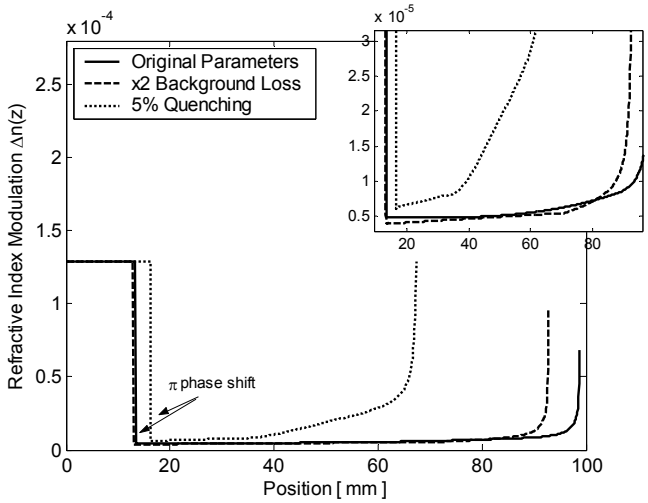

Figure 8-7 Designs in Yb doped fibre with different loss mechanisms

The original fibre requires a 98mm-long grating (solid line). The fibre with larger background loss requires a similar grating (dashed line) with a slightly reduced coupling coefficient (see inset) and a slightly smaller total length. This weaker grating provides the lower optimum signal value required in the medium with larger background loss. However the introduction of lifetime quenching significantly changes the cavity design

(dotted line). The device is now only 65 mm since a shorter device is needed in order to prevent the excessive pump loss. At the same time a stronger grating is needed to sustain the larger optimum signal. Figure 8-8 compares the power characteristics of these three designs.

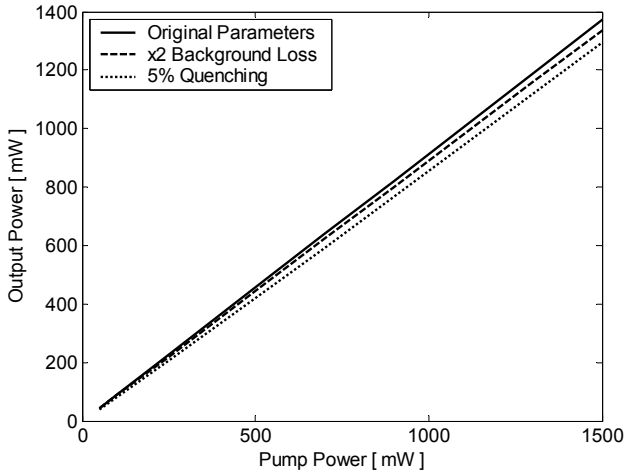

Figure 8-8 Power characteristics of designs in Yb doped fibre with and without additional losses.

The characteristics follow the same behaviour expected from the comparison of the maximum possible efficiencies shown in Figure 8-6(b). Table 8-2 compares and summarises the maximum efficiency limits and output powers possible and the ones achieved with the derived cavities in each case. Despite the difference of the loss mechanisms, lasers showed comparable efficiencies. This clearly demonstrates the strength of the new design method showing that quite different loss mechanisms can be accommodated with proper cavity design and their effects can be minimised.

	Ideal Medium	Original Medium Limit / Derived Cavity	x2 Background Loss Limit / Derived Cavity	5% Quenching Limit/Derived Cavity
Efficiency	0.920	0.915 / 0.912	0.910 / 0.893	0.870 / 0.860
Power(mW)	1380	1373 / 1368	1365 / 1340	1305 / 1290

Table 8-2 Efficiency and power summary in Yb doped fibre

The optimum value of the signal power maximises the conversion from pump to signal wavelength and therefore minimises the power loss through heat generation. As a result, the derived cavity, in addition to superior efficiency, will show linear power characteristics and longitudinal mode stability, and lower requirements on temperature control and packaging. Comparison of the heat generation in the derived cavity with original parameters (Figure 8-9) with the heat generation in the standard design with the same parameters (Figure 8-5) shows the difference, clearly.

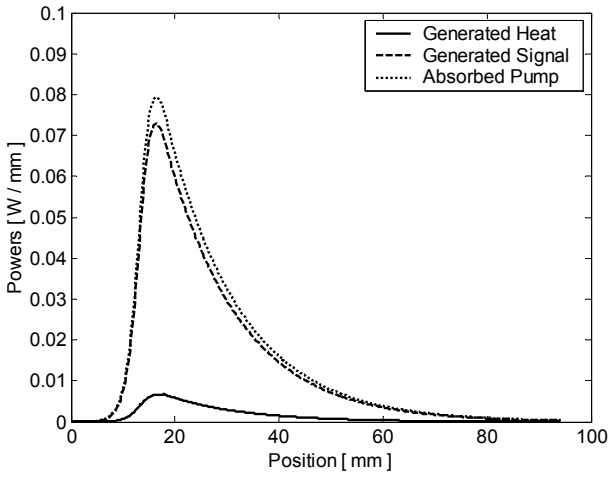

Figure 8-9 Signal generation, pump absorption and heat generation in the derived cavity.

In the derived optimum cavity the peak value of the generated heat has dropped from 0.3 W /mm to less than 0.008 W / mm. This will reduce temperature gradient considerably along the cavity and minimise the effects of thermally-induced chirping. Such cavity is expected to be much more stable and robust.

8.3.2. Design for cladding-pumped fibre

High power pump sources are usually available as highly multi-moded laser diodes. In order to utilise these sources fibres with double claddings have been used [4]. The outer cladding confines the pump power in the inner cladding region, which encapsulates the single-mode signal core (Figure 8-10). Therefore this type of structure allows coupling of multi-moded pump powers and produces single-moded signal outputs. This pumping scheme is referred to as cladding-pumping.

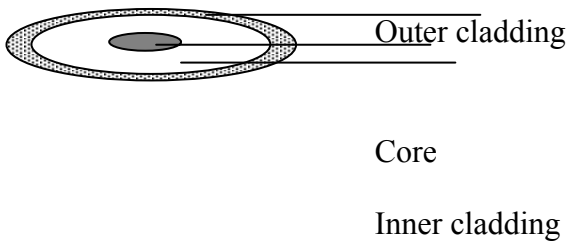

Figure 8-10 Cross-section of a double-clad fibre

Although such a structure allows coupling of large amounts of pump power, the actual overlap between the pump power and the active core is very small. The typical ratio of the inner cladding to core areas is in the range of 100 – 1000. In our simulations we

consider a core radius of 4 µm and an inner cladding radius of 50 µm, which gives an overlap coefficient for pump power and active core of 1/150. We define a core NA = 0.1 and cut-off of 980 nm so that it is single-moded at the signal wavelength of 1060 nm. This gives the same overlap coefficient of 0.8 for the signal as in the previous case of core-pumped fibre. If we keep the same Yb concentration of 5.8 x 10^{25} m^{-3} as well as the same model parameters, given in Table 8-1, we find the optimum signal powers and corresponding pump absorption and signal generation as shown in Figure 8-11.

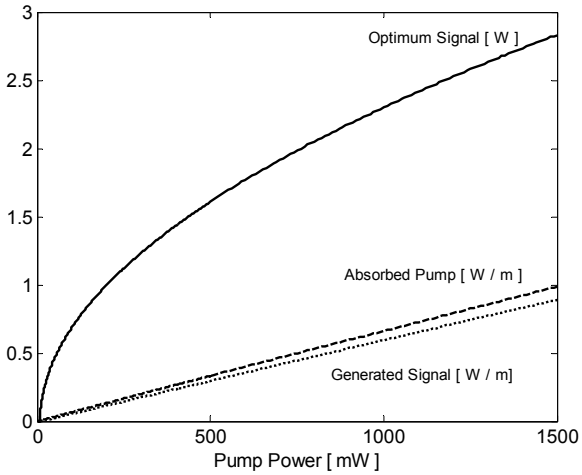

Figure 8-11 Optimum signal power, corresponding pump absorption and signal generation in double-clad fibre. Yb concentration 5.8x10^{25} m^{-3}.

From this figure we observe that over the pump power range we consider, the average pump absorption is about be 0.5 W/m. This means that 1.5 W of input pump power would be absorbed over a length of about 3 m. Production and packaging of such a long DFB laser would be totally impractical. Pump absorption can be increased by either increasing the core radius or by increasing the ion concentration. But in order to keep the core single-moded for the signal, the radius is kept, typically, below 5 µm. Therefore, we increase the Yb concentration to 50 x 10^{25} m^{-3} which is still considered to be practical. The life-time quenching associated with high dopant concentrations can be avoided by proper fibre drawing. The optimum signal and corresponding absorbed pump and generated signal are shown in Figure 8-12.

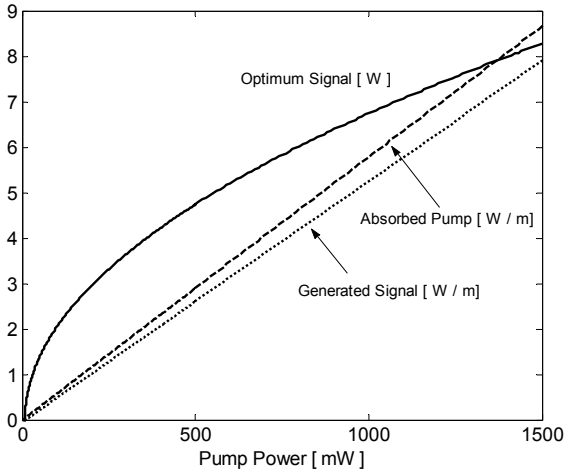

Figure 8-12 Optimum signal power, corresponding pump absorption and signal generation in double-clad fibre with increased Yb concentration (50 x 10^{25} m^{-3}) .

Now with almost 8 times larger absorption we can expect the design to be only several tens of cm instead of few meters. Indeed when we apply the design method we find that the RHS boundary condition is met at ~ 60 cm for the co-pumped scheme. The signal distribution and the corresponding apodisation profile are shown in Figure 8-13 (a) and (b), respectively.

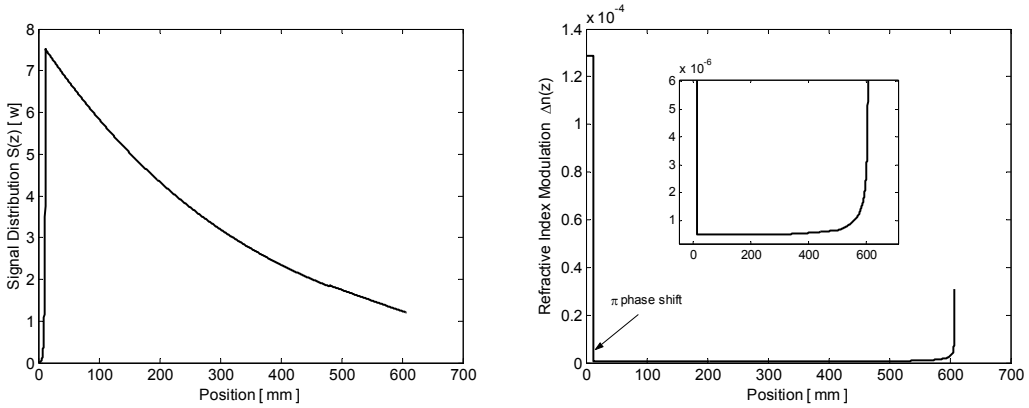

(a) (b)

Figure 8-13 (a) Signal distribution (b) Derived cavity in the cladding-pumped fibre with Yb concentration = 50 x 10^{25} m^{-3}

The smaller pump absorption in the cladding-pumped fibre results in a smaller maximum conversion efficiency compared to the core pumped fibre (Figure 8-14 (a)) and as a result the output power of the cladding pumped laser is smaller (Figure 8-14 (b)).

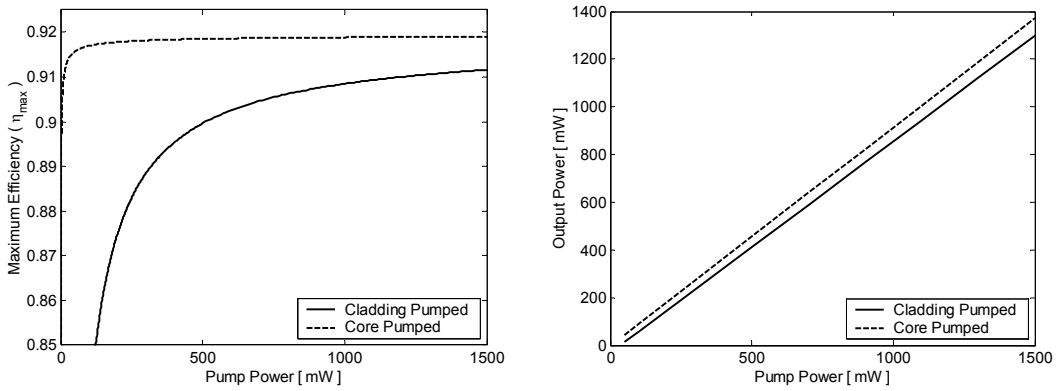

(a) (b)

Figure 8-14 (a) Maximum possible efficiency in cladding (solid) and core (dashed) pumped fibres. (b) Comparison of power characteristics of derived cavities in cladding and core pumped fibres.

8.4. Alternative Wavelengths

8.4.1. 915 nm pumping for 976 nm signal

So far we designed cavities for a pump at 976 nm. Application of the design method to other signal and pump wavelengths is quite straightforward, especially if the active medium dynamics do not change due to the choice of the pump and signal wavelength. As an illustration we can design a Yb doped laser pumped at 915 nm and operating at 976 nm again in the original core-pumped fibre. In order to do this, we change the pump absorption and emission cross-sections at 915 nm to 6.36×10^{-25} m^2 and 1.33×10^{-26} m^2, respectively and use the same 976 nm cross-section values, as given in Table 8-1, for the signal. We also keep the same overlap coefficients and background losses for the pump and signal. With this pump and signal wavelength pair, namely 915 nm and 976 nm, the quantum limit is 0.94.

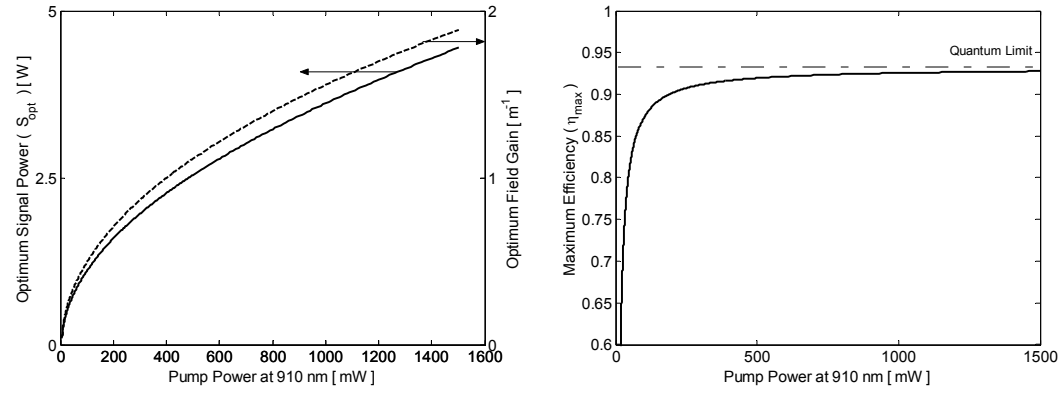

(a) (b)

Figure 8-15 (a) Optimum signal and gain values (b) Maximum possible efficiency for 915 nm pumping

Now we re-calculate the optimum signal and gain values and the maximum efficiencies as shown in Figure 8-15 (a) and (b), respectively for this new pair of pump and signal wavelengths.

We consider a total of 1.5 W pump power launched co-directionally. Such high-power, single-mode pump diode lasers, suitable for core-pumping, are not available today. However, it is interesting to investigate such a system and study its ultimate conversion efficiency. We calculate the signal and gain distributions as shown in Figure 8-16 (a) and calculate the required refractive index modulation profile as in Figure 8-16 (b). Due to the smaller pump absorption cross-section at 915 nm the device length is 20.5 cm. The large signal emission and absorption cross-sections, on the other hand, cause the gain to be as large as 40 m^{-1} in the non-optimised regions (c.f. dotted line in Figure 8-16 (a) right y-axis). The output power characteristics are shown in Figure 8-16 (c).

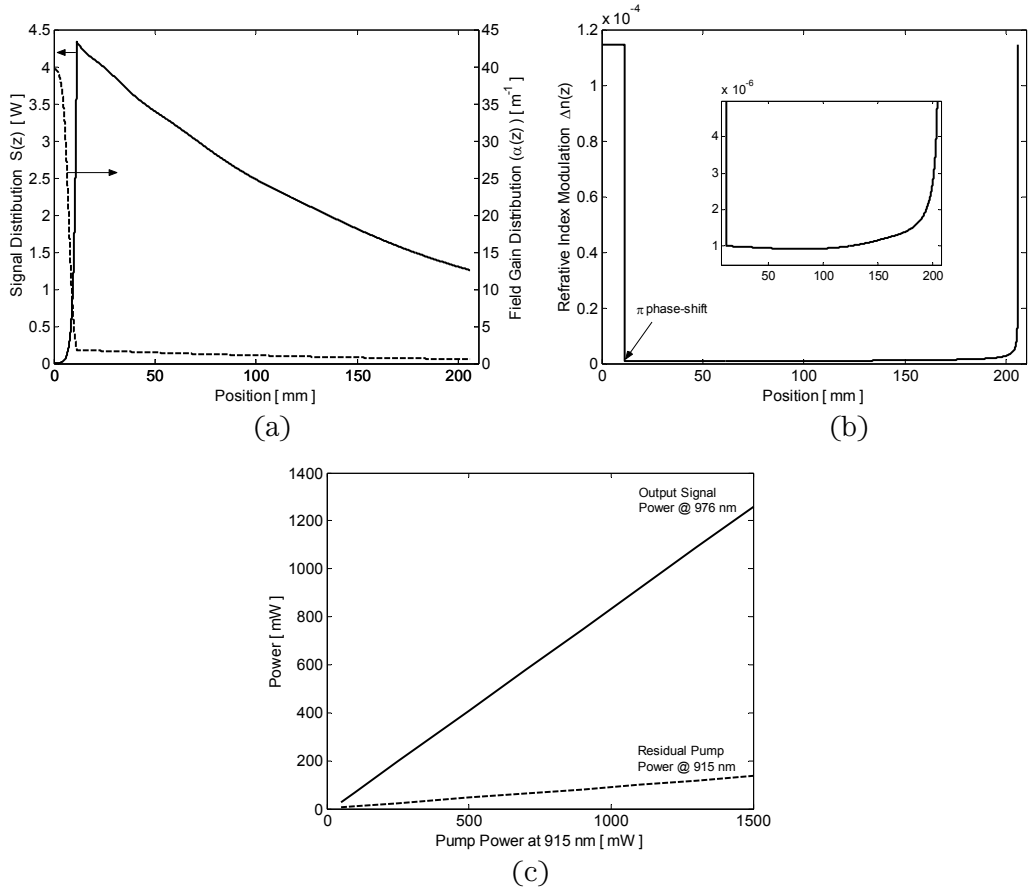

Figure 8-16 (a) Spatial distribution of the optimum signal and gain values for 1.5W co-directional pumping (b) Required refractive index modulation profile. (c) Output power and residual pump characteristics of the design.

In contrast to the case of 976 nm pumping, a large amount of pump power (~130 mW) leaves the cavity unabsorbed and the forward output power is 1250 mW. Although the conversion efficiency is 0.91, significant amount of pump power is not utilised. This is

due to the fact that the optimum signal that corresponds to the pump powers less than 130 mW is smaller than the output power generated by absorbing pump power of an amount = 1500 – 130 = 1370 mW. Increasing the length to absorb this residual pump power compromises the overall conversion efficiency. If the residual pump power is significant, as in this case, the problem can be easily solved by employing the counter-pumping scheme. The advantage of this scheme is that in the forward direction the optimum signal curve can be followed until very small pump powers (ideally no signal is desired in the forward direction) so that larger pump power is absorbed to produce larger output power from the backward end. As an illustration we now define the LHS output power to be 1350 mW and obtain the cavity as in Figure 8-17 (a).

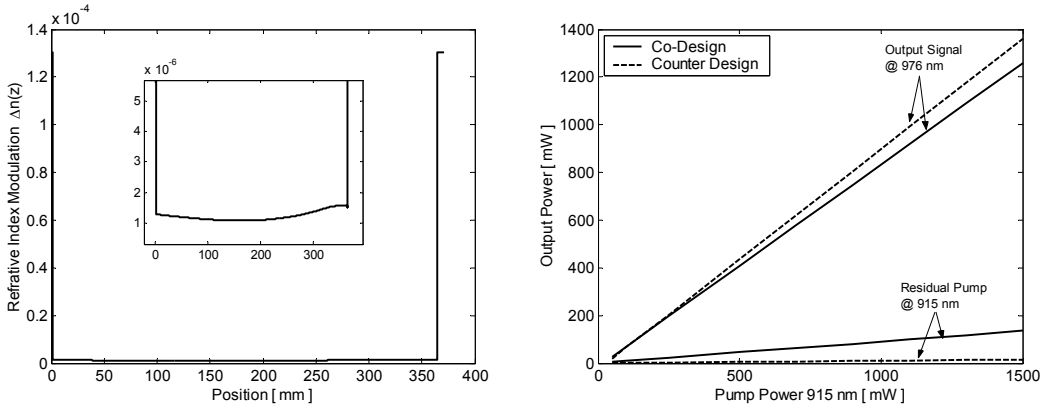

(a) (b)

Figure 8-17 (a) Counter-pumped design for 915 nm pumping and 976 nm signal (b) Comparison of output characteristics of counter- (dashed) and co- (solid) pumped designs.

This ~ 10 cm longer design results in larger pump absorption at optimum values and the residual pump is as small as 15 mW (c.f. 130mW of co-pumping case). As expected the the output power in this case is larger (Figure 8-17 (b)) than the co-pumped design output. The overall absorbed pump to generated signal conversion efficiency, however, remains the same at 0.91, since we follow the optimum curve in both cases.

From the point of view of pump and signal wavelengths these designs are comparable to the actual JAC fibre ASE source we used in our experiment described in the previous section. This high power JAC fibre was 1.2 m long and was capable of generating 400 mW power as an ASE source and 600 mW power in a laser configuration at 976 nm when pumped by 1500 mW at 915 nm[1]. Therefore; compared to these values the derived design, theoretically, can improve the efficiency by 100% and reduce the length to 1/4 of the JAC fibre, provided that high power pump lasers are suitable for core pumping.

8.4.2. 915 nm pumping for 1060 nm signal

As the final application we derive the cavity for 915 nm pumping and 1060 nm signal. We use the cross-sections quoted earlier and the core-pumped fibre with parameters given in Table 8-1. As always we start with the calculation of the optimum signal and optimum gain values as in Figure 8-18 (a) and this gives the maximum possible efficiency curve as in Figure 8-18 (b).

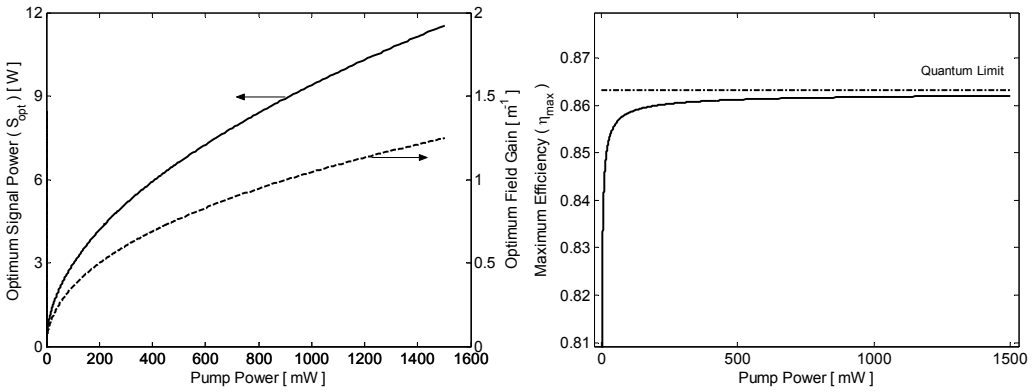

(a) (b)

Figure 8-18 (a) Optimum signal and gain values for 915 – 1060 operation (b) Resultant maximum efficiency for pump powers up to 1.5 W.

Then we spatially unfold these optimum values in relation to the pump absorption while taking the production limits into account and assuming co-pumping. We find the signal and gain distributions as in Figure 8-19 (a).

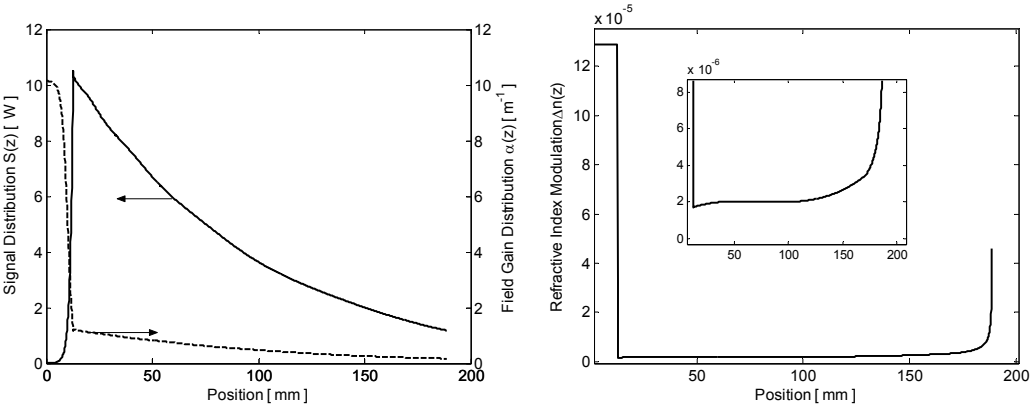

(a) (b)

Figure 8-19 (a) Signal and gain distribution for 915 – 1060 nm co-pumped design. (b) Derived apodisation profile.

The 19 cm long-design of Figure 8-19 (b) gives an output power of 1270 mW for the design pump power of 1500 mW. The residual pump power in the co-pumped scheme is around 20 mW, therefore the conversion efficiency is ~0.85 and the power characteristics are very linear as shown in Figure 8-20.

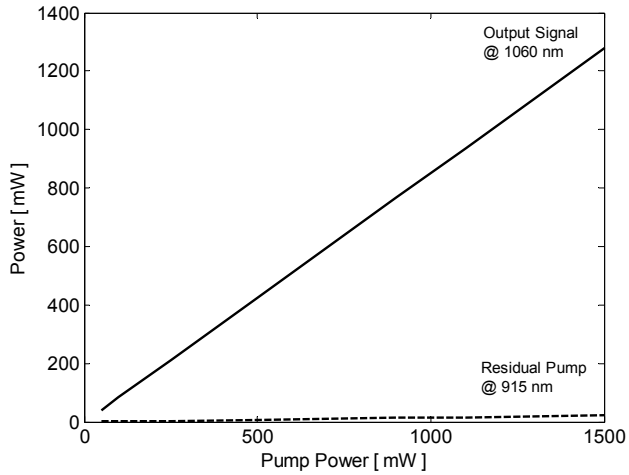

Figure 8-20 Power characteristics of co-pumped 915 – 1060 nm design.

The DFB lasers studied in Section 8.4. can be potentially quite useful in the future, if single-mode 915 nm pumps become available, for converting efficiently into other wavelengths which are more suitable for frequency doubling and other bio-medical and industrial applications.

8.5. Conclusions

Developments in the single-moded high power pump sources open the way for the high power regime for rare-earth doped fibre lasers. In accordance with these developments we applied the new design method for core-pumped fibres. We deduced the model parameters of the Yb doped fibre from the experimental data of JAC fibre ASE source application. Using this active model we investigated the effects of possible loss mechanisms on the efficiency and optimum values of signal and gain. The life-time quenching of Yb ions was found to be more severe limiting factor for the efficiency than the background loss. The presence of lifetime quenching requires a shorter cavity in order to prevent pump loss and a larger coupling coefficient to sustain the larger value of the optimum signal. The theoretical power characteristics of the designed cavities are found to be very linear with very small residual pump powers. As a result of larger conversion the generated heat in the derived cavity is significantly smaller and we expect this feature to allow simpler and better heat removal and packaging.

Although JAC fibres provide single-moded pump powers, high pump power sources are usually in the form of multi-moded laser diodes, which can be coupled to double-clad fibres efficiently. We applied the design method in a typical double-clad fibre for cladding-pumping and showed the feasibility of the application with sufficiently large ion concentrations.

We extended the theoretical investigation to alternative pump and signal wavelength pairs. We designed lasers for 915 nm core-pumping operating at 976 and 1060 nm. The reduced pump absorption resulted in longer designs compared to 976 nm pumping and in the case of 915-976 nm co-pumping a significant amount residual pump power remained unabsorbed although the efficiency with respect to the absorbed pump was at the limit. We showed that this shortcoming can be avoided by using the counter-pumping scheme.

The analysis in this chapter showed the usefulness of the new design method in an active medium alternative to Er/Yb co-doped fibre and for different pump power regimes as well as for different pump and signal wavelengths.

8.6. References

[1] R. Selvas, J. K. Sahu, L. B. Fu, J. N. Jang, J. Nilsson, A. B. Grudinin, K. H. Yla-Jarkko, S. A. Alam, P. W. Turner, and J. Moore, "High-power, low-noise, Yb-doped, cladding-pumped, three-level fiber sources at 980 nm," *Optics Letters*, vol. 28, no. 13, pp. 1093-1095, 2003.

[2] C. A. Codemard, L. Hickey, K. Yelen, D. B. S. Soh, R. Wixey, M. Coker, M. N. Zervas, and J. Nilsson, "400 mW 1060 nm ytterbium doped fiber DFB laser," presented at Photonics West LASE, San Jose, California, USA, 2004, 5335-11

[3] M. Ibsen, E. Ronnekleiv, G. J. Cowle, M. O. Berendt, O. Hadeler, M. N. Zervas, and R. Laming, "Robust high power (>20mW) all-fibre DFB lasers with unidirectional and truly single polarisation outputs," presented at CLEO, Baltimore, USA, 1999, CWE4

[4] J. Nilsson, W. A. Clarkson, R. Selvas, J. K. Sahu, P. W. Turner, S. U. Alam, and A. B. Grudinin, “High-power wavelength-tunable cladding-pumped rare-earth-doped silica fiber lasers”, *Optical Fiber Technology*, vol. 10, no. 1, pp. 5-30, 2004.

Chapter 9 Conclusions

Despite the intensive research on linear-cavity continuous-wave lasers there has been a lack of a comprehensive analytical laser design method to achieve the ultimate efficiency for a given pump scheme and active medium. Previous efforts have been focused on optimising a chosen cavity, such a FP, DBR or DFB structure. The optimisation of the cavities had to be parametric, and due to infinitely many different combinations of parameters these designs cannot guarantee to give the ultimate efficiency possible. In the case of DFB lasers we showed that it is possible to improve efficiency further than the parametric optimisation using intuitive arguments based on the effective cavity length. Identifying the critical importance of the signal distribution in the cavity we introduced the concept of optimum signal power for a given pump power.

We developed a novel analytical method for the design of laser cavities which guarantees the ultimate efficiency. In this approach a cavity is not *optimised* based on an *a priori* defined geometry but it is *derived* for the given pump and active medium. The method combines the general grating design equations, valid for both passive and active media, and the optimum signal power calculations. The idea that lies at the heart of the design method is to sustain the optimum signal power at every single point in the entire cavity for the local maximum conversion efficiency. The cavity derived by this method allows the absorbed pump power to be converted into the signal power in the best possible way every where in the cavity. Therefore this method guarantees the ultimate conversion from absorbed pump power to the generated signal.

In certain cases the residual pump power can be large and the efficiency with respect to the launched pump power can be notably smaller than the effiency with respect to the absorbed pump power. We investigated such a situation in Section 8.4.1 and showed that this practical problem can be solved by using a counter-pumping scheme instead of of a co-pumping scheme. The signal distritbution for counter-pumping scheme allows the complete conversion of the launched power using longer gratings.

When applying the new method there are three main points to be addressed, namely;

(i) Proper definition of boundary conditions that result in physically realisable cavity.

(ii) Practical grating limits imposed by the grating writing techniques.

(iii) Effects of model parameters on the derived cavity.

We illustrated how to approach these issues with various examples. The fundamentals of the theory are developed in a general fashion while we demonstrated and experimentally verified the method in rare-earth doped fibres. We used this particular set of examples due to the attractive features of rare-earth doped fibres for a broad range of applications. Table 9-1 summarises the efficiencies, η, that are achievable in the Er/Yb co-doped fibre when a total of 200 mW pump power at 976 nm is launched for generating 1552 nm signal and taking the production requirements into account.

	Parametrically optimised Best DFB Laser	Step Apodised DFB Laser	Derived Cavity Co-Pumping	Derived Cavity Counter-Pumping	Derived Cavity Bi-Pumping	Derived Cavity No production restriction	Er/Yb co-doped medium ultimate limit	Ideal Medium Quantum limit
η	0.20	0.27	0.31	0.34	0.35	0.38	0.38	0.63

Table 9-1 Pump-to-signal conversion efficiency comparisons in Er/Yb doped fibre

Improving the Er/Yb co-doped medium's ultimate efficiency limit of 0.38 to the ideal medium's quantum limit of 0.63 is not a cavity design problem only; it also requires spectroscopic improvements in the active medium properties to avoid any loss mechanisms.

Similarly Table 9-2 compares the efficiency limits and efficiencies achievable in Yb doped fibres using 976 nm core-pumping and operating at 1060 nm for two different losses. Parametrically optimised DFB laser and the derived cavity have the same length in each case.

	Parametrically optimised DFB Laser	Derived Cavity Co-Pumping	Derived Cavity No production restriction	Yb doped medium ultimate limit	Ideal Medium Quantum limit
η (low loss)	0.88	0.90	0.915	0.915	0.92
η(5% quenching)	0.81	0.86	0.88	0.88	0.92

Table 9-2 Pump-to-signal conversion efficiency comparisons in Yb doped fibre

When the losses are very small the medium is close to an ideal medium therefore the signal power does not have a significant effect and the conversion is close to the quantum limit. In this case the parametrically optimised and the derived cavities provide comparable efficiencies. However when losses increase using the optimum value of the signal becomes critical and the design method's superiority becomes apparent.

In addition to the fundamental investigations we refined previously known modelling and characterisation techniques for the simulation of lasers in rare-earth doped fibres. In our approach we treated the pump source, the active medium, and the grating as a complete system. Unlike the previous studies which gave information as trends, our results are benchmarked against experimental data and actual values are obtained for different laser designs.

We investigated the effects of the various loss mechanisms on the ultimate efficiency limit. The life-time quenching of ytterbium ions is found to be the main deteriorating parameter both in Yb and Er/Yb co-doped fibres. In the latter case increasing the Er concentration can improve the fundamental efficiency, however; there is a trade-off between compensating the life-time quenching of Yb ions and increasing the co-operative up-conversion among Er ions. We also investigated the choice of pumping scheme on the efficiency. Bi-directional pumping is shown to be the best choice for this particular active medium.

Since the derived designs are critically based on the model parameters we investigated the effects of the uncertainties of the model parameters and concluded that the variations in the critical parameters would result in the scaling of the cavity length and the apodisation profile. We confirmed the theoretical results for co-pumping experimentally in Er/Yb co-doped fibre. The 10% shorter new design provided a nearly 60% increase in the output power compared to the parametrically optimised standard design. This is the shortest and highest efficiency laser operating at 1552 nm pumped around 976 nm reported to date.

We addressed the longitudinal-mode stability of the new designs. The sufficiently large 2^{nd} order threshold gain and much better spatial overlap between the fundamental and 2^{nd} order mode compared to the standard design ensured the stable single-mode operation in the new design without any chirp. Investigation of the effects of chirping on the stability justified the choice of non-chirped designs.

We also extended the application of the method to alternative pump and signal wavelengths and to alternative pump power regimes. Namely; we derived cavities for core and cladding-pumping and for pump and signal pairs (976 nm, 1060 nm), (915 nm, 976 nm) and (915 nm , 1060 nm) in Yb doped fibres with efficiency close to the ultimate limit when production limitations are imposed.

The method is applicable to any active medium whose properties do not significantly change over the length of intereset and in which a grating can be incorporated. Therefore we expect this design method to find immediate application over a wide range area from semiconductor, planar glass, solid-state to fibre lasers since in these media the grating writing technologies have already matured.

Beyond the ultimate effiency design method:

The method derives the laser design for a medium with pre-defined properties pumped with a pre-defined source. There is always room for improvements in the active medium properties, such as reducing the loss mechanisms, and improving the pump source such as tailoring the pump wavelength or its overlap with the active medium. The ultimate effiency from various active media and pumping options can be conveniently calculated and compared using the concepts and methods developed in this study.

The practical limitations in the application of the method arise from the restrictions imposed by the grating writing technology and the uncertainities in the active medium characterisation.

APPENDIX – A : Derivation of conversion efficiency in Yb Ions

The total ion concentration, N_T, gives:

$$N_1 + N_2 = N_T \tag{A.1}$$

The field gain coefficients at signal and pump wavelengths are:

$$\alpha_S = N_2\sigma_{s,e} - N_1\sigma_{s,a} \tag{A.2a}$$

$$\alpha_P = N_2\sigma_{p,e} - N_1\sigma_{p,a} \tag{A.2b}$$

The generated signal ΔG and the absorbed pump ΔP are:

$$\Delta G = 2(\alpha_s - \varepsilon_s)S \tag{A.3a}$$

$$\Delta P = 2(-\alpha_s + \varepsilon_P)S \tag{A.3b}$$

and the rate equation at steady state gives:

$$\frac{dN_1}{dt} = -N_1\left(\frac{P}{h\nu_p}\sigma_{p,a} + \frac{S}{h\nu_s}\sigma_{s,a}\right) + N_2\left(\frac{P}{h\nu_p}\sigma_{p,e} + \frac{S}{h\nu_s}\sigma_{s,e} + \frac{1}{\tau}\right) = 0 \tag{A.4}$$

from (A.4) we find

$$N_1\left(\frac{P}{h\nu_p}\sigma_{p,a} + \frac{S}{h\nu_s}\sigma_{s,a}\right) = N_2\left(\frac{P}{h\nu_p}\sigma_{p,e} + \frac{S}{h\nu_s}\sigma_{s,e} + \frac{1}{\tau}\right) \tag{A.5}$$

and we define absorption, A, and emission, E, terms as

$$\begin{aligned} A &= \left(\frac{P}{h\nu_p}\sigma_{p,a} + \frac{S}{h\nu_s}\sigma_{s,a}\right) \\ E &= \left(\frac{P}{h\nu_p}\sigma_{p,e} + \frac{S}{h\nu_s}\sigma_{s,e} + \frac{1}{\tau}\right) \end{aligned} \tag{A.6}$$

and substituting the definitions into (A.5)

$$N_1 = \frac{E}{A}N_2 \tag{A.7}$$

(A.7) and (A.1) are solved for N_1 and N_2 as:

$$\begin{aligned} N_1 &= \frac{E}{E+A}N_T \\ N_2 &= \frac{A}{E+A}N_T \end{aligned} \tag{A.8}$$

Now substituting N_1 and N_2 values in gain coefficient equations (A.2a) and (A.2b) we find:

$$\alpha_S = \frac{N_T}{E+A}\left(A\sigma_{s,e} - E\sigma_{s,a}\right)$$
$$\alpha_P = \frac{N_T}{E+A}\left(A\sigma_{p,e} - E\sigma_{p,a}\right) \tag{A.9}$$

and gain coefficient are substitution in equations for generated signal and absorbed pump (A.3a) and (A.3b) transforms the equations as:

$$\Delta G = 2\frac{N_T}{E+A}\left[A\sigma_{s,e} - E\sigma_{s,a} - \varepsilon_s\left(\frac{E+A}{N_T}\right)\right]S \tag{A.10a}$$

$$\Delta P = 2\frac{N_T}{E+A}\left[-A\sigma_{p,e} + E\sigma_{p,a} + \varepsilon_p\left(\frac{E+A}{N_T}\right)\right]P \tag{A.10b}$$

The pump-to-signal conversion efficiency

$$\eta = \frac{\Delta G}{\Delta P} \tag{A.11}$$

with the substitution of (A.10a) and (A.10b) becomes:

$$\eta = \frac{\left[A\sigma_{s,e} - E\sigma_{s,a} - \varepsilon_s\left(\frac{E+A}{N_T}\right)\right]S}{\left[-A\sigma_{p,e} + E\sigma_{p,a} + \varepsilon_p\left(\frac{E+A}{N_T}\right)\right]P} \tag{A.12}$$

using definitions of A and E as given in (A.6) we transform (A.12) as:

$$\eta = \frac{\left[\frac{P}{h\nu_p}\left(\sigma_{s,e}\sigma_{p,a} - \sigma_{s,a}\sigma_{p,e}\right) - \frac{\sigma_{s,a}}{\tau} - \varepsilon_s\left(\frac{E+A}{N_T}\right)\right]S}{\left[\frac{S}{h\nu_s}\left(\sigma_{s,e}\sigma_{p,a} - \sigma_{s,a}\sigma_{p,e}\right) + \frac{\sigma_{p,a}}{\tau} + \varepsilon_p\left(\frac{E+A}{N_T}\right)\right]P} \tag{A.13}$$

APPENDIX – B : Alternative Boundary Transitions

Consider the illustration in Figure B-1

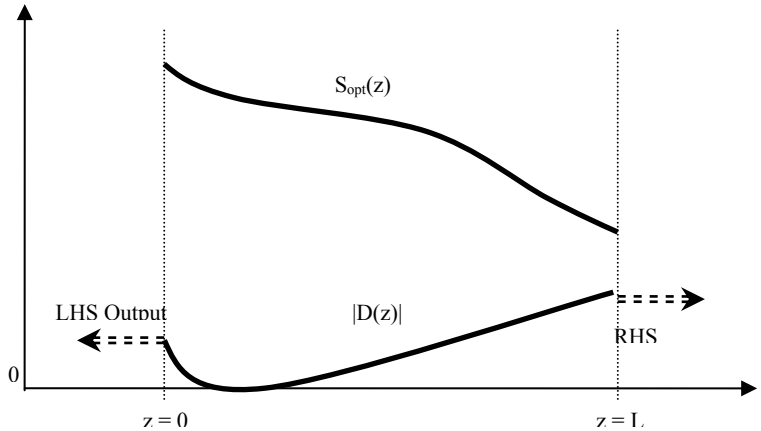

Figure B-1 Illustration of optimum signal distribution and corresponding $|D(z)|$ function variation in an active medium.

Since there are no incident fields from the outside of the laser cavities as Equations (6.38) and (6.39) show $|D|$ is equal to the output powers at the boundaries and it must be equal to the signal power S at $z = 0$ and $z = L$. In general the optimum signal distribution S_{opt} may not match $|D(z)|$, as illustrated above.

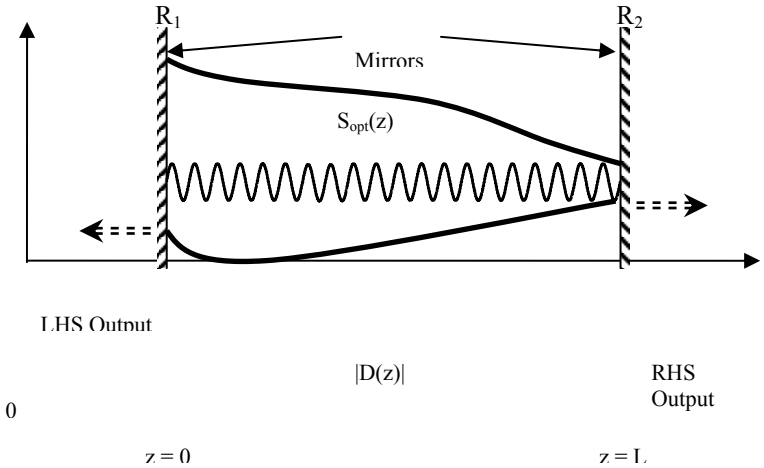

Figure B-2 Matching boundary conditions by step changes using mirrors

In this case a step change from S_{opt} to output powers is required which can be achieved by placing mirrors with two external mirrors with reflectivities:

$$R_1 = \frac{S_{opt}(0^+) - |D(0^-)|}{S_{opt}(0^+) + |D(0^-)|} \qquad R_2 = \frac{S_{opt}(L^-) - |D(L^+)|}{S_{opt}(L^-) + |D(L^+)|} \tag{B.1}$$

at LHS and RHS boundaries respectively as illustrated in Figure B-2.

In this case the final cavity will consist of two external mirrors –satisfying the boundary conditions – and a grating in between, with a specific apodisation profile that sustains the optimum signal value throughout the cavity. But in certain cases, depending on the pumping scheme and active medium properties, S_{opt} and $|D|$ can become equal at a position L so that the boundary condition at L is matched without the need for an external mirror. This was the case we encountered in Figure 6-22, with the Yb doped fibre example, and it is illustrated below schematically.

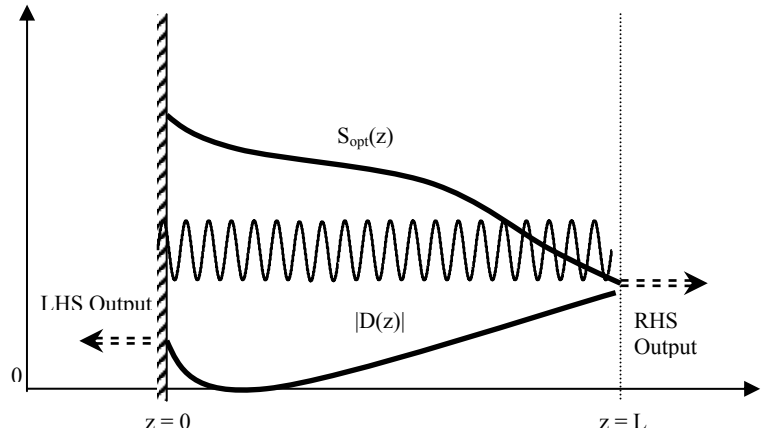

Figure B-3 Coincident optimum signal distribution and $|D(z)|$ function at RHS boundary

This type of signal distribution will then require only a LHS mirror to be connected to the grating.

The mirrors required for the step changes in the signal distribution can lead to very challenging production problems. Splicing or butt-coupling a grating to mirrors with perfect phase relations is anticipated to be impractical. This problem, however, can be overcome by sacrificing a small amount of efficiency: Instead of step changes right at the boundaries, smoother transitions can be defined over a short length which can be achieved by a grating so that the need for an external mirror is avoided.

In Figure B-4 the dashed curves illustrate these smooth transitions between the optimum signal value and the output powers. Of course in the shaded region the efficiency will not be the maximum, since the signal power is not optimum. However these smooth transitions can be sustained by gratings and in this case the cavity will be an all-grating device therefore it can be produced in a single manufacturing step without any splicing or additional connection. In our experimental investigations we will employ this technique.

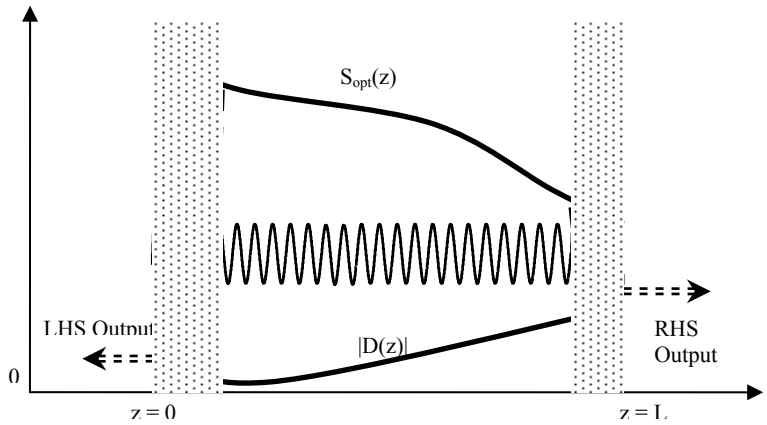

Figure B-4 Matching the boundary conditions with smooth transitions and gratings.

List of Publications

Publications & Presentations

K. Yelen, L. Hickey, M.N. Zervas, "A New Design Approach for fibre DFB Lasers with Improved Efficiency", *IEEE Journal of Quantum Electronics*, vol. 40, no 6, pp 711-720, 2004.

K. Yelen, M.N. Zervas, L. M. B. Hickey, "Fibre DFB Lasers with Ultimate Efficiency", *OFC 2004* Post-deadline Paper PD21, Los Angeles, USA, 22-27 Feb 2004.

K. Yelen, L. M. B. Hickey, M.N. Zervas "A New Design Approach for DFB Lasers for Improved Efficiency", *OFC 2004* ThB1, Los Angeles, USA, 22-27 Feb 2004.

C.A Codemard, L. Hickey, K. Yelen, D. B. Soh, R. Wixey, M. Coker, M. N. Zervas, J. Nilsson "400 mW 1060 nm ytterbium Doped Fiber DFB Laser", *Photonics West 2004*, San Jose, USA, 24-29 Jan 2004.

K. Yelen, L. Hickey, M.N. Zervas, "Experimentally Verified Modelling of erbium ytterbium Co-Doped DFB Fiber Lasers", IEEE Journal of Lightwave Technology, In Press.

K. Yelen, M.N. Zervas, L. M. B. Hickey, "Fibre DFB Lasers with Ultimate Efficiency", IEEE Journal of Lightwave Technology, In Press.

Submitted and under Preparation

"Design Method For Ultimate Efficiency in Linear-Cavity Continuous-Wave Lasers with Distributed-Feedback"

"68 mW Output Power at 1550 nm from Er/YB Co-Doped Fiber DFB Laser"